

**NUMERICAL INVESTIGATION ON STRENGTH UPSCALING AND ITS  
APPLICATION TO A BACK ANALYSIS OF AN OPEN PIT SLOPE FAILURE**

by

Cristian Andres Guajardo

B.S.GEO., Universidad Católica del Norte, 2007

A THESIS SUBMITTED IN PARTIAL FULFILLMENT OF  
THE REQUIREMENTS FOR THE DEGREE OF  
MASTER OF APPLIED SCIENCES

in

THE FACULTY OF GRADUATE AND POSTDOCTORAL STUDIES  
(Mining Engineering)

THE UNIVERSITY OF BRITISH COLUMBIA  
(Vancouver)

January 2020

© Cristian Andres Guajardo, 2020

The following individuals certify that they have read, and recommend to the Faculty of Graduate and Postdoctoral Studies for acceptance, a thesis/dissertation entitled:

Numerical investigation on strength upscaling and its application to a back analysis of an open pit slope failure

---

submitted by Cristian Andres Guajardo in partial fulfillment of the requirements for

the degree of Master of Applied Science

in Mining Engineering

Examining Committee:

Davide Elmo, Mining Engineering

Supervisor

Ali G. Madiseh, Mining Engineering

Supervisory Committee Member

Stephen Rogers, Golder Associates Ltd.

Supervisory Committee Member

## **Abstract**

Strength scale effect refers to the decreasing of rock strength when specimen size increases. The drop of strength is specific of the rock type and is related to the presence of natural defects. Scale effect has been widely studied in laboratory test and numerical simulations and there is consensus on the importance of upscaled rock strength for excavation design. However, due to lack of data at scale of rock block, is not uncommon that non-upscaled laboratory properties are applied directly for geotechnical assessment. Besides, literature is scarce on practical applications of scaled rock block strength. In this thesis, numerical upscaling of rock strength is performed and used to back analyze a major instability. The study case corresponds to a highly defected and fractured leached rock that participated in a major slope failure of an open pit mine. First, geological and geotechnical characterization of the defected rock is presented. Then, rock strength is numerically upscaled using synthetic rock numerical samples. Finally, the upscaled rock strength is applied to estimate rock mass strength as input for a bidimensional slope failure back analysis.

Synthetic rock experiments were performed in ELFEN FDEM code, on bidimensional samples with diameters between 5 centimeters to 1 meter. A discrete defect network was built in Fracman software based on core logging data. Uniaxial, biaxial and indirect tensile test were performed. The FDEM code was able to simulate realistically cracking patterns and stress-strain curves. The scale effect of the unconfined strength was verified while friction angle showed to be size invariant. The back analysis of slope failure demonstrated that the confined strength was overestimated, likely due to the lack of constraint that the third dimension impose.

The bidimensional back analysis of the slope instability was performed in ELFEN FDEM code and RS2 continuum code. A discrete fracture network of faults was included in ELFEN analysis. Assessments applying upscaled and non-upscaled properties were compared. There was small difference between the two cases due to the larger influence of the joints regarding the upscaled rock strength. However, the case based on upscaled properties reproduced the failure more accurately in both, FDEM and continuum code.

## **Lay Summary**

The strength scale effect refers to the decreasing of rock strength when specimen size increases. While the importance of using upscaled strength in the design and stability assessment of excavations is acknowledged by geotechnicians, in practice the use of non-upscaled strength is common. In this work, laboratory and field data were used to computationally simulate synthetic rock samples with defects and highlight the importance of using upscaled properties. A range of synthetic sample sizes was tested, characterizing the scale effect. This upscaled strength was used to numerically simulate a real failure of an excavated slope. Analysis performed applying upscaled and non-upscaled strength were compared. More precise reproduction of the slope failure was obtained with upscaled properties, demonstrating the importance of considering scale effect. The synthetic rock showed to be useful to upscale the unconfined strength, but confined strength was overestimated due to the bidimensional nature of the simulated synthetic samples.



## **Preface**

This thesis is original and independent work done by the author. Two abstracts were submitted to consideration to ARMA 2020 congress. The author was the main author of both articles. The co-author of these papers were the thesis supervisor and Steve Rogers from Golder Associates.

The paper “Numerical investigation on rock strength upscaling using synthetic rock approach” is based on Chapter 4 in this thesis.

The paper “Back analysis of an open pit slope failure using numerically upscaled rock strength” is based on Chapter 5 in this thesis

## Table of Contents

Abstract .....	iii
Lay Summary .....	iv
Preface .....	v
Table of Contents .....	vi
List of Tables .....	xi
List of Figures .....	xii
Acknowledgements .....	xxiii
Dedication .....	xxiv
Chapter 1. Introduction .....	1
1.1 Research statement .....	1
1.2 Research objective .....	3
1.3 Thesis Organization .....	4
Chapter 2. Literature review .....	6
2.1 Introduction .....	6
2.2 Brittle rock strength .....	6
2.2.1 Mechanics of the brittle failure .....	6
2.2.2 The Mohr-Coulomb and Hoek and Brown failure criterion .....	8
2.3 Rock strength scale effect (strength upscaling) .....	12

2.3.1 Defects and Rock Block Strength .....	15
2.4 Synthetic Rock numerical modelling.....	18
2.4.1 Numerical discontinuum approach for SR.....	21
2.4.2 Applications of SR to defected rocks.....	23
2.5 Slope stability analysis with continuum codes and FDEM codes .....	27
2.6 Conclusion .....	29
Chapter 3. Basic Geological and Geotechnical characterization of the Leached rock .....	31
3.1 Introduction.....	31
3.2 Geological Setting.....	31
3.2.1 The Leached rock in the context of Chuquicamata Mine Geology .....	31
3.2.2 Structural geology of the north east slope.....	33
3.2.3 Geology of the Leached geological unit .....	37
3.2.3.1 Healed defects in the Leached unit .....	39
3.3 Laboratory strength test of leached geological unit.....	41
3.3.1 Uniaxial compressive strength.....	41
3.3.2 Tensile strength, confined strength and intact rock failure envelope .....	42
3.3.3 Strength of defects .....	45
3.4 Geological Strength Index (GSI) of the Leached geological unit.....	47
3.5 Conclusion .....	50

Chapter 4. Numerical investigation on rock strength upscaling using synthetic rock approach .....	51
4.1 Introduction.....	51
4.2 Synthetic Rock (SR) test model setup .....	51
4.3 Discrete Fracture Network of Defects .....	53
4.4 Synthetic Rock properties .....	55
4.4.1 Material properties .....	55
4.4.2 Veins properties .....	56
4.4.3 Rock matrix (Leached Granodiorite) properties .....	57
4.4.4 Contact Properties.....	59
4.5 Mesh, critical time step and computation time .....	64
4.5.1 Mesh quality.....	64
4.5.2 Mesh size dependency .....	66
4.5.3 Critical time step and computation time .....	68
4.6 Synthetic Rock tests.....	69
4.6.1 Uniaxial Compression Strength upscaling relationship.....	69
4.6.2 Uniaxial compression strength of Synthetic rock samples .....	71
4.6.3 Biaxial compression strength of synthetic rock samples .....	76
4.7 Indirect tensile strength of synthetic rock samples .....	80

4.8 Uniaxial strength of the defected leached rock in combination with joints.....	81
4.8.1 Strength of rock bridges in a defected rock with joints .....	81
4.9 Other methods to upscale defected rock strength .....	85
4.9.1 MRMR Rock Block strength (Laubscher and Jackubeck, 2000) .....	85
4.9.2 Composite GSI (Day et al 2012, Day, 2016) .....	86
4.10 Conclusion .....	89
Chapter 5. Upscaled strength of the defected rock and its application in the back analysis of a slope failure.....	91
5.1 Description of the slope failure.....	91
5.2 Geological setting .....	93
5.2.1 Geological units .....	94
5.2.2 Structural Geology .....	95
5.3 Discrete Fracture Network of faults.....	97
5.3.1 Faults DFN model validation.....	98
5.4 Model settings.....	101
5.4.1 Section geometry and excavation stages.....	101
5.4.2 Intact rock and rock mass input properties .....	102
5.4.3 Loadings.....	107
5.5 Bidimensional numerical modelling of the failure .....	107

5.5.1 Slope failure back-analysis in finite element continuum code RS2 .....	107
5.5.2 Slope failure back-analysis in FDEM code ELFEN .....	111
5.5.3 Influence of intact rock confined strength on stability analysis .....	115
5.6 Conclusion .....	118
Chapter 6. Conclusions .....	121
6.1 Conclusions summary .....	121
6.2 Findings on synthetic rock modelling of the defected rock and numerical upscaling..	122
6.2 Findings on the use of numerically upscaled properties to assess major excavations stability.....	123
References .....	127

## List of Tables

Table 4.1. Input parameters for defects DFN .....	54
Table 4.2. Final properties used for SR modelling highlighted in grey.....	59
Table 4.3. Contact Properties used for SRM modelling .....	63
Table 4.4. Mohr Coulomb and H&B properties characterizing biaxial test in Figure 4.16.....	79
Table 5.1. Input parameters for faults DFN (SD=Standard Deviation).....	98
Table 5.2. Input properties for 2d slope stability analysis. Rock mass friction angle and cohesion were obtained from the linearization of H&B criteria and applied to M-C properties in ELFEN code. ....	105
Table 5.3. H&B's $m_i$ and equivalent Rock mass Friction angle for sensitivity analysis performed on HELTZ unit confined strength. Base $m_i$ value corresponds to the non-defected intact rock. Numerically upscaled $m_i$ is equal to $m_i*2$ .....	115

## List of Figures

Figure 1.1. Examples of the variety of natural defects that can control scale effect in rocks. a) Micro fractures in mineral grains filled with clays in a shear zone next to a major fault (40x, polarized light, Chuquicamata mine, Flores and Karzulovic, 2003) b) Stockwork with quartz veinlets in a hard rock at El Teniente Mine (Flores and Karzulovic, 2003) c) Granodiorite with scarce visible defects, in this case strength upscaling is controlled mainly by mineral contacts d) Same granodiorite showed in c but with abundant veins of quartz with sericitic halo. e) Quartz sericitic rock with soft mineral veins. f) Beach boulder with strong quartz veins that survived transportation and erosion; given the strength of veins the scale effect is probably controlled by mineral grains (photographs c, d and e courtesy of Chuquicamata mine).....	2
Figure 2.1. a) Chemical bond break in tension in a microscopic flaw (modified from Eberhardt, 1999). b) Mechanism model of internal crack extension towards the major principal stress. $\sigma_t$ , major principal stress; $\tau$ , shear stress. The initial defect is modelled as an elliptical fracture which develops tensile strength concentration at its tips (from Eberhardt et al, 1998).....	7
Figure 2.2. The Mohr-Coulomb failure criterion in the normal stress ( $\sigma$ ) - shear stress ( $\tau$ ) space. The MC envelope is tangent to Mohr's circles (modified from Goodman, 1989). ....	9
Figure 2.3. Basic GSI chart. A numerical value for GSI is obtained by qualitatively assessing the joint condition and the blockosity (Hoek and Marinos, 2000) .....	11
Figure 2.4. Relationship between H&B and equivalent MC failure criterion in the principal stresses space (Hoek et al, 2002).....	12
Figure 2.5. Hoek and Brown (1981) UCS data compilation (a) and application of Yoshinaka <i>et al</i> (2008) power function to UCS laboratory test (b) (from Yoshinaka <i>et al</i> , 2008, after Pratt <i>et al</i> 1972). Note that (a) suggests a single exponent equal to 0.18 for different types of rock, while Yoshinaka's power function application in (b) uses k exponents depending on the rock type. ....	14



Figure 2.6. Influence of defects intensity in the intact rock strength estimation. Is not uncommon that, as in the case in the central and right photographs, defects are difficult to assign to any type of geological feature. IRS: Intact Rock Strength (From Jakubec, 2013).....	16
Figure 2.7. Failure types in veined laboratory test specimens before and after testing (from Bewick et al., 2018): (a) homogeneous break via splitting; (b) homogeneous break via shear rupture; (c) combined break; (d) discrete vein break; and (e) break around/along veins, clasts or nodules. ..	17
Figure 2.8. a) Adjustment factor to determine rock block strength based on Laubscher and Jakubec (2000) procedure (from Bewick et al., 2019) b) White arrows indicate joints bounding the “intra block structure” included in Day’s Compound GSI (modified from Day et al., 2012).....	18
Figure 2.9. An example of Synthetic Rock that emulates a real sample submitted to biaxial compression test (from Turichshev and Hadjigeorgiou, 2015) .....	19
Figure 2.10. Key aspects of DFN modelling and implication for SRM (Elmo et al, 2016).....	20
Figure 2.11. Conceptual definition of the use of equivalent continuum rock mass properties to represent small scale fracturing (from Elmo and Stead, 2017). The same equivalent continuum concept can be applied to SR samples at lower scales.....	21
Figure 2.12. PFC particle bond and sliding joint model (Elmo et al, 2016).....	22
Figure 2.13. Voronoi method implemented into DEM models (Elmo et al, 2016). .....	22
Figure 2.14. Scale effect on SR samples. Scale effect becomes more pronounced as vein strength decrease, percentage indicates vein strength is relative to host rock (from Pierce et al, 2009)....	24
Figure 2.15. SR with deterministic DFN embedded in a BPM were assessed by Vallejos et al (2016) (above) and Turichshev and Hadjigeorgiou (2016) (below). The diameter of samples in both cases is approximately 50 mm. ....	25

Figure 2.16. Micro DFN and Voronoi tessellation used in the work of Stavrou et al (2019). Red and green are virtual scan-lines.....	26
Figure 2.17. SR simulation of defected rock in FDEM code. Hamdi’s biaxial test on samples with microdefects on the left (Hamdi et al., 2015) and Karimi et al (2016) rock bridge simulation on the right. Both experiments were developed in ELFEN code. ....	27
Figure 2.18. SSR analysis of a slope performed in RS2 (Rocscience). MC (left) and H&B (right) materials can be used in the simulation (Sari, 2019). ....	28
Figure 2.19. Elfen model geometry (left) and pit slope deformation at 40% of caving extraction at Palabora mine. A DFN fabric with variable intensity is included in the slope rock mass (from Vyazmensky et al., 2010).....	29
Figure 3.1. Plan view of geotechnical units in Chuquicamata mine. Pit border in black. The West Fault (in blue) is a hard geological limit between the ore in the east block and waste rock in the west block. The dotted line encloses the leached rock (geology by Chuquicamata mine Superintendency of Geotechnics) .....	32
Figure 3.2. Schematic cross section showing the supergene zonation of Chuquicamata mine (modified from Dold, 2003).....	33
Figure 3.3. Fault zone components used to categorize mapped structures in Chuquicamata mine. Fault core + damage zone, together with mapped continuity are used to classify the faults as VIF or FT, as indicated in the figure (modified from Caine et al, 1996). ....	34
Figure 3.4. Stereonets of faults mapped in bench scanline. Great circle for north east slope is included as reference together with planar limits (dotted line in black).....	35
Figure 3.5. Structures with rank 3-4 are interpreted in ATV record as faults VIF and FT. A blind zone, delimited with red lines, is formed due to preferential drilling of holes. Only one planar, non-daylighting set is defined by poles concentration, absence of other structural sets is likely due to bias related to the orientation of drillholes. ....	36

Figure 3.6. Tridimensional wireframes of major structures in the north east slope, in the leached rock and surrounding units. Bench scanline mapping of VIFs and drillhole's interception of faults, oriented with ATV, are the supporting information. ....	37
Figure 3.7. Cross section of the leached unit. This cross section is used in Chapter 5 to back analyze the slope instability that occurred in the leached rock. ....	38
Figure 3.8. Bench excavated in Heterogeneous Leached Zone (HELZ). Brown colors corresponds to abundant Iron Oxides and Hidroxides. Note the high degree of fracturation of this geotechnical unit. ....	39
Figure 3.9. Photograph of drill core with defects. Infill of defects and joints coating correspond to same mineralogy of iron oxides and gypsum. Orientation of defects and open joints is in various cases similar. ....	40
Figure 3.10. Stereonet of drillhole's ATV for discontinuities of rank 1 and 2 (number of poles =13722). This orientation was assumed the same for joints and healed defects in the Leached unit. ....	41
Figure 3.11. Histograms of UCS laboratory test performed on samples from the leached geological unit. Diameter of samples with rock matrix brake (left) varies from 45 to 60 mm, diameter of samples with mixed rupture (right) was 61 mm. All strength data was converted to a 50 mm diameter sample using Hoek and Brown (1980) size – strength relationship. Basic statistics presented for each data set. SD: standard deviation, CV: coefficient of variation, n: total number of samples. ....	42
Figure 3.12. Indirect tensile strength (Brazilian) test for the leached unit. Rock matrix break only. SD: standard deviation, CV: coefficient of variation, n: total number of samples. ....	43
Figure 3.13. Laboratory strength test and H&B's failure envelopes for rock matrix brake and mixed brake. Data points are 183 for rock matrix break and 80 for mixed break. Note that there is no	

tensile strength data for mixed brake test. UCS and mi factor that characterize each H&B's failure envelope are included in the figure. H&B's envelope fitting carried out in Rocdata software.... 44

Figure 3.14. Biaxial test with break throughout a single defect (or joint) was used to characterize defect's strength,  $\psi$  is the angle between the defect and the axial load (a). Normal and shear stress in the defect are located at point A (b), which is formed by the intersection of a line from F, making an angle  $\psi$  with the horizontal axis, and Mohr circle. Alternatively, normal and shear stress can be obtained drawing a line from F', making an angle  $\psi$  from the vertical, and piercing the Mohr circle at A (from Goodman, 1989)..... 45

Figure 3.15. Biaxial laboratory test data with rupture trough single defect converted to normal stress ( $\sigma_n$ ) - shear stress ( $\tau$ ) space using Goodman's procedure. The linear regression of the data yields the failure criterion for defects, namely: Cohesion=1.3 MPa, Friction angle =  $45^\circ$  ..... 46

Figure 3.16. GSI mapped in Leached rock on the north east slope. Figures a and c show the north east slope (in gray) with bench scanline mapping and drillholes respectively. Average GSI from bench mapping is equal to 42 (b) while drillhole GSI is equal to 40. More detailed characterization can be performed in drill core logging, hence the higher dispersion for that support. Further analysis of the apparent bimodal distribution in (d), lead to a subdivision of the Leached rock based on GSI. .... 48

Figure 3.17. GSI logged on drill core showed a spatially consistent spotted distribution of GSI less than 35. This spatially traceable pattern allowed to map two separated geotechnical units in the Leached rock, namely HELZ and HOLZ (upper cross section). Statistics on drill core logging showed a reduced dispersion of GSI values when the leached unit is separated in HELZ and HOLZ (lower histograms), which confirms the suitability of the differentiation. Coefficient of variation for Leached unit without differentiation is 21%, which compares to 17% for HOLZ and 16% for HELZ. .... 49

Figure 4.1. SR sample setup. Basic setup geometry to the left. Final SRM with DFN of defects added for a 250x500 mm sample size to the right side of the figure (H: sample height). .... 52

Figure 4.2. Defects generation for SRM modelling. 1 Defects DFN realization (input parameters from Table 1). 2 Vertical cross section (5x5 m) showing intercepted 3D defects. 3&4 shows defect traces as obtained from the cross section. 5 Defects were drawn using linear traces as guide, defect's material properties are then assigned to these polygons in the SRM model (width of each defect is 2mm)..... 55

Figure 4.3. SR calibration on 100x50 mm samples. MC's cohesion and friction angle were obtained linearizing H&B's envelope for a  $\mu$  of 11.3 (from real laboratory test) and the UCS indicated in the figure for each box. Rock matrix UCS of 36.5 MPa yield SR strength matching actual laboratory test. .... 58

Figure 4.4. (a) Schematic representation of a block containing a single discontinuity (after Bandis, 1993) (b) Penalty contacting couple in ELFEN as an equivalent spring system (after Klerck, 2000). Kn: normal joint stiffness, ks: tangential joint stiffness (Elmo, 2006) ..... 60

Figure 4.5. Stress – Strain curves for different values of default penalties (Sample 1:  $P_n=5$  GPa, Sample 2:  $P_n=25$  GPa, Sample 3:  $P_n=100$  GPa;  $P_t=0.1P_n$  for all samples). Sample 4 (purple line) shows different post peak trend due to the use of cohesion in the default contact property ( $C_0=1$  MPa). In grey the uniaxial test geometry, before loading (left) and showing the typical post peak cracking pattern (right). Numerical test performed using uncalibrated rock matrix properties. .. 61

Figure 4.6. Stress-strain curves for 4 different penalty variations ( $P_t=0.1*P_n$ ) in a 500x1000 mm SR UCS test. Figures at the bottom show the sample before loading and fracturing pattern at peak strength..... 62

Figure 4.7. ELFEN crack insertion procedure showing: a) the actual failure direction defined by weighted average configuration, b) intra-element fracturing, c) inter-element fracturing. (Klerck et al., 2004) ..... 64

Figure 4.8. Numerically unstable 1x2 meter UCS SR test including defects and joints a) SR with incipient cracking b) Abnormal cracking 0.005 seconds after crack onset (at that time the model

crashed) c) stress – strain curve d) Zoom in to anomalous zone, note that mesh elements in defects are not particularly long.  $Q_m$  for all elements is  $>0.15$  and 98.5% of elements has  $Q_m > 0.5$  ..... 65

Figure 4.9. Results of biaxial test on 500x1000 mm sample with defects. a) stress-strain Curve showing similar pre peak behavior and peak strength. b) Combined mesh with 10 mm elements in the rock matrix and 5 mm elements in the defects. Coarser mesh in the platens has no influence in the test. c) Combined mesh sample at 0.24% vertical strain showing poor development of shear bands. Intra element fracturing was used in this simulation. d) Single size mesh with 4 mm elements size. e) Single size mesh at 0.24% vertical strain showing well developed shear bands. .... 67

Figure 4.10. Scale effect relations for intact rock UCS proposed by Yoshinaka *et al* (2008). Hoek and Brown relationship ( $k = 0.18$ ) is showed in green (taken from Pierce et al. 2009)..... 71

Figure 4.11. Stress – strain curves for six selected UCS SR samples, each curve represents one of the six sample sizes. .... 72

Figure 4.12. Selected Synthetic Rock samples for UCS test (same as in Figure 4.9), before loading (pre-test) and at peak strength..... 73

Figure 4.13. Synthetic rock UCS vs sample diameter. Exponent  $k=0.38$  in Yoshinaka's relationship (equation 4.6) describes the strength drop in the range 100 – 500 mm sample diameter. (x symbol depicts single UCS test. Averaged UCS for each group size in green. Number of samples (n) indicated for each size) ..... 74

Figure 4.14. UCS size dependence for defected rock. In red UCS results and strength upscaling for the defected rock with a matrix of unconfined strength equal to 52 MPa. In green data presented in Figure 4.11 (matrix UCS = 36.5 MPa). Only rock matrix strength was increased, DDN geometry, defects strength and number of samples for each size is same for both cases..... 75

Figure 4.15. Fracturing patterns in SR biaxial test. a) SR sample, preloading geometry b) 1 MPa confinement biaxial test. Zoom in on the development of wing cracks from defects tip during

elastic stage (pre peak strength), parallel to vertical main stress c) 6 MPa confinement biaxial test at the time of reaching peak strength d) 6 MPa confinement biaxial test, zoom-in on crack coalescence in shear band during plastic stage. Same defects geometry and sample size (250x500 mm) for all numerical tests in the figure..... 77

Figure 4.16. Biaxial strength of four selected SR samples with defects and non-defected sample (in green). Continuous line show fitted H&B failure envelope characterized by sample UCS and  $m_i$  parameter (in rectangle). Curve and dots in green correspond to sample with no defects..... 78

Figure 4.17. a) Four disc samples were tested under indirect tensile strength. b) Fracturing pattern after reaching peak tensile strength (Ts), size in mm indicates sample diameter. .... 80

Figure 4.18. Sample assemblage of defected rock, and its equivalent continuum, with 2 joint networks. UCS yielded from the numerical simulation is presented at the bottom of the figure. 83

Figure 4.19. Laubscher and Jakubec (2000) procedure to calculate rock block strength, applied to leached granodiorite data. .... 86

Figure 4.20. a) Modified Joint condition ratings (modified by Day, 2016, from Bieniawsky, 1989), circled: in green ratings for defects, in blue ratings for joints. Raw data for ratings from drillhole mapping and bench mapping. b) CGSI chart (Day, 2016). Block volumes obtained from DFN of defects and joints using Sybill algorithm in Fracman. Joint Condition (JC) from table in a. Calculations performed as indicated in upper left quadrant in the chart. .... 88

Figure 5.1. Inter-ramp slope failure on which back analysis was performed. The rupture extends approximately from 3000 meters above sea level (m.a.s.l.) down to 2830 m.a.s.l. A pushback was located on top of the failed rock mass and 180 m below the toe of the breakage. A shovel is shown as scale reference. .... 92

Figure 5.2. Contouring of slope velocity at early stage of deformation (5 months before the event) and after the failure. Nearest pushbacks showed in green and red in pit photograph. The pit is 4 kms long by 2 kms width. Slope velocities monitored with robotic theodolite..... 93

Figure 5.3. Geological units and main faults outcropping in the failed slope. HELZ and HOLZ units not differentiated. Red line indicating the position of the 2d section analyzed in RS2 and ELFEN software. ....	95
Figure 5.4. Laser topography of the slope failure. Structural limits of the slide in red. Fault Z5S is a continuous structure while the back and north bound of the failure are formed by combination of faults, joints and breakage of rock bridges. ....	96
Figure 5.5. Stereonet of faults (VIF+FT) and joints. Planar limits for a parallelism criterion of +/- 20°. Joints orientations sourced from ATV of drillholes in the HELZ unit (assuming rank 1-2 as joints). For faults, two structural sets are located at the border of planar limits, although there are no clear planar sets there are faults located within the planar limits (20°). ....	97
Figure 5.6. Validation of DFN's traces length distribution. a1, b1 VIF and FT realizations were generated in a 250 m side cube. a2, b2 each realization was sampled with a trace plane with same slope orientation (azimuth=N20°W, dip=70°). a3, b3, comparison of the trace length distribution of simulated faults (brown) and mapped faults along scanlines(blue). ....	99
Figure 5.7. Stereonets comparison of mapped and DFN generated faults.....	100
Figure 5.8. Geometry of the vertical cross section assessed in RS2 and Elfen software. Sequence of excavation stages indicated in circled number. Meters above sea level are indicated at the left. ....	102
Figure 5.9. Example of upscaling approach in function of mesh size elements as proposed by Elmo and Stead (2010). ....	103
Figure 5.10. Hoek and Brown envelopes for Intact Rock (a) and Rock Mass (b) for HELZ unit. For intact rock envelopes, numerically upscaled properties depict a weaker rock (a). In the case of rock mass envelopes, unconfined strength difference is less marked due to low GSI, the increasing of strength with confinement is higher for the rock mass based on non-upscaled laboratory properties of intact rock strength. ....	106



Figure 5.11. Bidimensional stability analysis in RS2 FE code showing maximum shear strain for non-upscaled intact rock properties (a) and numerically upscaled intact rock properties (b). In both cases the extension of the failure and shape is quite similar and consistent with field observations. Black dotted line marks HELZ limit. HELZ: Heterogeneous Leached Zone; HOLZ: Homogeneous Leached Zone; GRD: Granodiorite. Major implicit faults in pink ..... 109

Figure 5.12. Bidimensional stability analysis in RS2 FE code showing absolute horizontal displacement for non-upscaled intact rock properties (a) and numerically upscaled intact rock properties (b). As expected, due to similar H&B's rock mass envelopes, displacement is alike between both cases. The zone of major displacement is concordant with the actual failure. Maximum horizontal displacement is approx. 0.5 m. Black dotted line marks HELZ limit. HELZ: Heterogeneous Leached Zone; HOLZ: Homogeneous Leached Zone; GRD: Granodiorite. .... 110

Figure 5.13. Vertical cross section assessed in Elfen software. Sequence of excavation stages indicated in circled number. Meters above sea level are indicated at the left. Thin blue and red traces correspond to DFN of VIF (red) and FT (blue faults). ..... 112

Figure 5.14. Bidimensional failure back analysis in ELFEN code showing horizontal displacement for simulation using rock mass properties based on non-upscaled intact rock properties (a) and numerically upscaled intact rock properties (b) for HELZ unit. Interpreted failure surface for 0.7 m horizontal displacement is showed with black dotted line. Major fault limiting the back of the failure in red. Level 2830 correspond to the toe of the real failure. .... 113

Figure 5.15. Sensitivity analysis performed in RS2 on increasing values of H&B's  $m_i$  as a manner of assess confined strength. Variations of  $m_i$  only for HELZ unit. Figures colored by maximum shear strain. The extension of the failure surface does not change significantly. SRF varies from 0.95 for  $m_i=15$  to 1 for  $m_i=23$  ..... 116

Figure 5.16. Sensitivity analysis performed in ELFEN software. H&B's  $m_i$  was transformed to friction angle for M-C rock mass properties. Figures colored by horizontal displacement. Interpreted failure surface (0.7 m threshold) indicated with dotted line. The extension of the failure

surface and depth of the movement decreases when friction angle decrease. Failure surface for a friction angle of  $23^\circ$  (c) shows the best match with the extension of the real failure..... 117

## Acknowledgements

I would like to thank my supervisor professor Davide Elmo for his support, time, guidance and valuable “crash course” on the tool that helped me to produce this thesis. My work under his supervision became a breaking point in my understanding of rock mechanics.

I would also like to thank NSERC (Natural Sciences and Engineering Research Council of Canada) for the financial support provided to this research through a Collaborative Research Development grant (Grant No. 11R74149; Mine-to-Mill Integration for Block Cave Mines). I would like to express my gratitude to Golder Associates Ltd. for providing an academic license for the code FracMan. Thanks to Conicyt (Chile) for the financial support provided through scholarship.

I would like to thank the Superintendence of Geotechnics of Chuquicamata mine. To my friend Rodrigo Araya for his help and to Milton Arellano to grant permission to use the data that makes it possible to apply the core ideas contained in this thesis.

A very special thank you to two good friends. To Serge Seguret that with his encouraging enthusiasm pushed me to pursue this degree. To Steve Rogers for give me a well-needed hand when landed in Canada with my family and for his invaluable help along the way.

Thanks to my mother and father, all that you did gave me the freedom that allows me to be where I am now.

A big thank you to the most important persons in my life. To my beloved daughter and son, Leonor and Martin, for being so brave at the beginning of this journey, I could not be prouder of you both. To Gaspar, for that last little push at the end of this. To Evelyn, my wife, she did the part of the work that is not written here, probably the most important part, Thanks for being always there for us.

*To Evelyn, Leonor, Martin and Gaspar*

# Chapter 1. Introduction

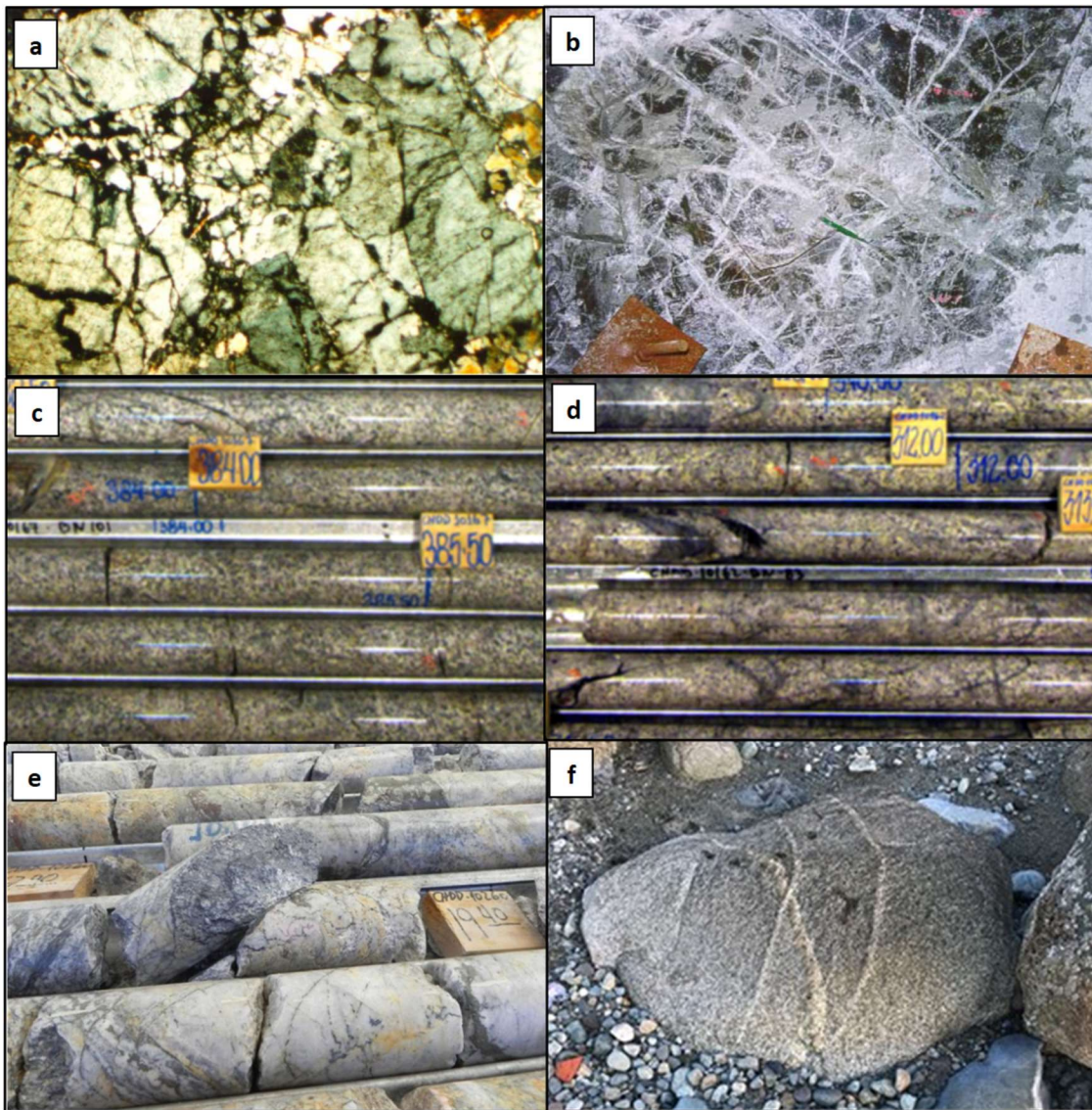
## 1.1 Research statement

The drop of strength when specimen size increases is a well-established characteristic of rocks. It is commonly called the scale effect or strength upscaling. The scale effect is explained by brittle failure mechanics as directly linked to the existence of natural flaws in the rock. The tips of these natural flaws (or defects) act as tensile stress concentrators from where new cracks form and propagate. As the specimen size becomes bigger, the probability of including a greater number of flaws increases, more tensile cracks will form, reducing the specimen strength. Rock flaws can be present as mineral contacts, microcracks, veins, patches of alteration minerals or any other defect that is not a joint or fault. Their geometry varies depending on defect type, with size ranging from a few millimeters, as is the case of micro cracks and mineral contacts, up to meters for some type of veins.

The scale effect can be mathematically modelled using Weibull's distribution; however, the prominence of the strength drop is specific for each rock type and depends on the characteristics of its flaws. Size, intensity, orientation and strength of the defects are primary factors that control the scale effect. Thus, given the variety of defects that can be found in the different geological settings (**Figure 1.1**), scale effect must be assessed specifically for each rock type.

The scale effect is of key importance in the design of excavations and stability assessment of rock masses. Due to the scale involved, the strength of a rock mass is not measurable, therefore its mechanical behavior is commonly assessed indirectly, by estimating the combined effect of the intact rock strength with the network of joints. The underlying assumption in this estimation is that the intact rock strength fairly represents the strength of the block bounded by joints, i.e. the rock block strength. Laboratory tests used to measure strength of the intact rock are commonly performed on a limited range of sample sizes, keeping the strength upscaling relationship, and the important rock block strength, unknown. Cost, and difficult obtention and preparation of larger samples are the main reasons that prevent the investigation of strength at different sizes. Thus, the

actual rock block strength remains unknown and the analysis is performed using data that do not necessarily represent the inter-joint rock block.



**Figure 1.1. Examples of the variety of natural defects that can control scale effect in rocks. a) Micro fractures in mineral grains filled with clays in a shear zone next to a major fault (40x, polarized light, Chuquicamata mine, Flores and Karzulovic, 2003) b) Stockwork with quartz veinlets in a hard rock at El Teniente Mine (Flores and Karzulovic, 2003) c) Granodiorite with scarce visible defects, in this case strength upscaling is controlled mainly by mineral contacts d) Same granodiorite showed in c but with abundant veins of quartz with sericitic halo. e) Quartz sericitic rock with soft mineral veins. f) Beach boulder with strong quartz veins that survived transportation and erosion; given the strength of veins the scale effect is probably controlled by mineral grains (photographs c, d and e courtesy of Chuquicamata mine)**

Synthetic Rock (SR) modelling has been proven to be a useful technique to assess the mechanical behavior of rocks, including the investigation of scale effect. From the different types of available codes, hybrid finite-distinct element methods (FDEM) offer special advantages to realistically model rock strength testing. Their ability to simulate the transition continuum – discontinuum, by the developing of cracks that follow brittle failure mechanics, make them adequate for SR testing. The necessity of minimum calibration and direct use of rocks' mechanical properties are other advantages. The aim of this investigation was to explore the suitability of numerically upscaled properties, performed in a FDEM hybrid code, to obtain rock block strength. The effectiveness of the approach was evaluated using the numerically upscaled properties as input to assess a major slope instability.

This research was developed using field and laboratory data collected from a defected rock associated to a major slope instability in Chuquicamata mine.

## **1.2 Research objective**

The main objectives of this research are:

- To explore the ability of FDEM code ELFEN to upscale the strength of a rock with abundant defects under the limitations of modelling in a bidimensional space
- To explore the suitability of numerically upscaled rock strength as a rightful parameter to assess rock mass strength.

The following tasks were developed to achieve the primary objectives of the research:

- Geological and geotechnical characterization of the intact rock, defects and rock mass that were numerically modeled. Laboratory tests and field data of a defected rock were used with this aim.
- Application of core logging data and field observations to build a discrete defect network (DDN) using the FracMan software.
- Assessment of the scale effect in the defected rock using SR samples assembled in ELFEN FDEM code combining the DDN, calibrated intact rock properties and defects strength. A

series of numerical UCS, biaxial and indirect tensile strength test were performed at a range of sizes.

- Assessment of a major slope failure associated to the defected rock using numerically upscaled properties. Hence establish suitability of upscaled strength as a licit parameter to estimate rock mass strength.

### **1.3 Thesis Organization**

This thesis is organized in six Chapters. The results presented in each chapter are used in the next section linking the text logically.

Chapter 2 summarizes the main concepts and numerical tools used to develop the research. Key literature related to the following themes was reviewed in Chapter 2: brittle failure mechanics, phenomenological description of rock failure, scale effect, rock block strength, SR modelling of defected rocks and its past applications, and slope stability assessment using numerical codes.

The practical part of the research was developed based on information of a defected rock associated to major slope instability in Chuquicamata mine. Thus, geological and geotechnical characterization, numerical strength upscaling of the defected rock, and back analysis of slope failure is progressively developed along Chapters 3, 4 and 5.

Based on field data and laboratory test the defected rock is geologically and geotechnically characterized in Chapter 3. Rock matrix strength, defects strength, and rock mass characterization are presented in this chapter and used later in Chapter 4 and 5.

Chapter 4 present the SR experiments developed in ELFEN hybrid code to assess scale effect and obtain upscaled properties for the defected rock. The building of the discrete defect network and rock matrix calibration are presented. Numerical UCS, biaxial and indirect tensile tests are developed for a range of sizes to obtain the fully upscaled strength. Upscaled UCS is compared with Laubscher and Jakubec (2000) method to estimate rock block strength and Day *et al* (2014) method to account for defects into GSI. Additionally, numerical experiments were developed to assess the scale effect in rock bridges.



Chapter 5 shows the back analysis of the major slope failure involving the defected rock assessed numerically in Chapter 4. Assessment of slope stability is performed and compared using numerically upscaled properties and non-upscaled laboratory properties. The analysis was performed in ELFEN FDEM code and RS2 continuum code; results from both methods are compared as well.

Conclusions, analysis limitations and recommendations for future studies are presented in Chapter 6.

## **Chapter 2. Literature review**

### **2.1 Introduction**

This Chapter provides a literature review of the main concepts and techniques applied in the development of this thesis. Brittle mechanics notions and the two main phenomenological descriptions used for rock failure, Mohr-Coulomb and Hoek and Brown, are presented. Strength upscaling (scale effect), rock block strength and the role of defects are presented as the main concepts that drive the development of this research. Then, Synthetic Rock modelling, which was the numerical tool used to develop the experiments in this thesis, and previous applications to model defected rocks and upscaling rock strength are summarized. Finally, a general overview of the application of continuum and hybrid numerical methods to slope stability assessment is presented. Slope stability analysis was used in this research to assess the suitability of numerically upscaled strength to reproduce a real slope failure.

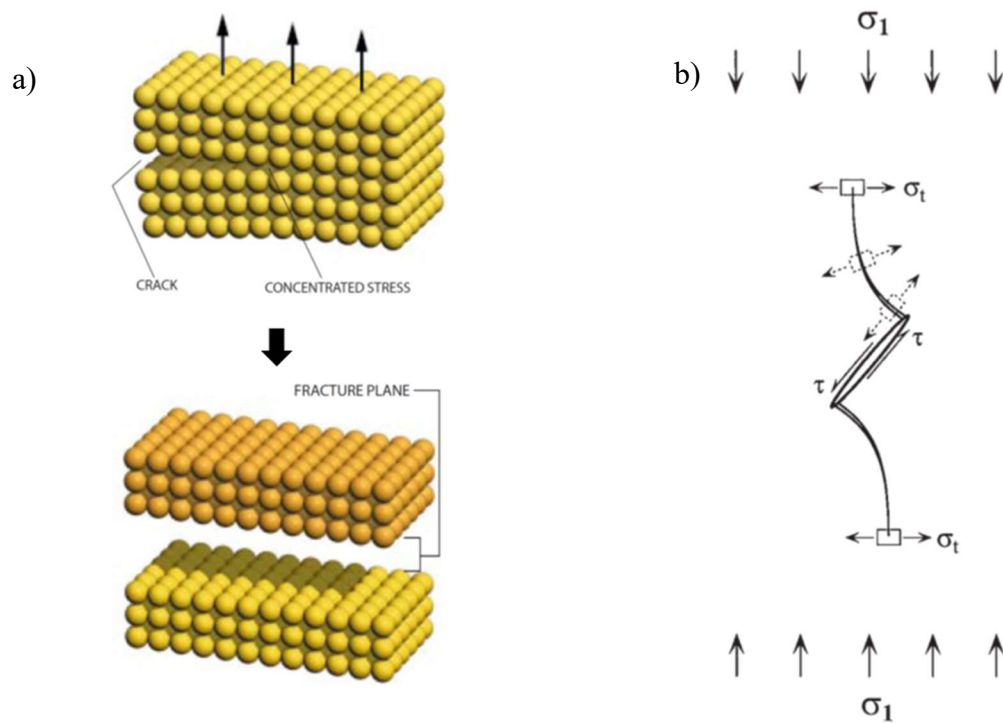
### **2.2 Brittle rock strength**

Rock strength is defined as the point of failure at which the progressive development of cracks prevents the rock from carrying additional load. Rock failure can be described under two approaches: Mechanistic and Phenomenological (Eberhardt et al, 1998). The former describes the microscopic phenomenon of fracture, while the latter correspond to generalizations of large-scale observations. Griffith's fracture theory (1920) is a widely accepted mechanistic approach. The two main phenomenological approaches used in rock mechanics correspond to Mohr-Coulomb and Hoek and Brown failure criterions.

#### **2.2.1 Mechanics of the brittle failure**

Independently of whether the origin of a material is man-made or natural, it breaks or fails due to the presence of flaws. These flaws can be imperfections at an atomic scale or discontinuities of sizes ranging from millimeters up to meters. At the microscopic scale, a solid can be seen as a collection of atoms, arranged in an ordered and periodical manner, held together by chemical bonds which can stretch until reaching a critical point at which the bond is broken. When enough bonds

are broken, a crack is formed in the solid (Eberhardt, 1999). The mechanics of a chemical bond breaking implies rupture in tension or shear, since repulsive atomic forces prevent bonds from breaking under compression. However, the sole breaking of chemical bonds is not enough to explain the strength of the great majority of materials, including rocks. Even the strongest material breaks at approximately  $1/10^{\text{th}}$  of the stress required to break chemical bonds (Eberhardt, 1999 *op cit*). Griffith (1920), showed that strength is controlled by defects or cracks already present in the material. Thus, when stress is applied, tensile strength is concentrated at the tip of the crack, where the chemical bonds break initiating a brittle fracture. **Figure 2.1** shows the mechanism of a chemical bond break (a) and growth of the newly initiated fracture (b), with crack opening in the direction of lowest confinement and crack propagating parallel to the main stress (Eberhardt et al, 1998). The initial flaws can be microscopic, as a discontinuity in the molecular arrangement of the material, or visible as a crack.



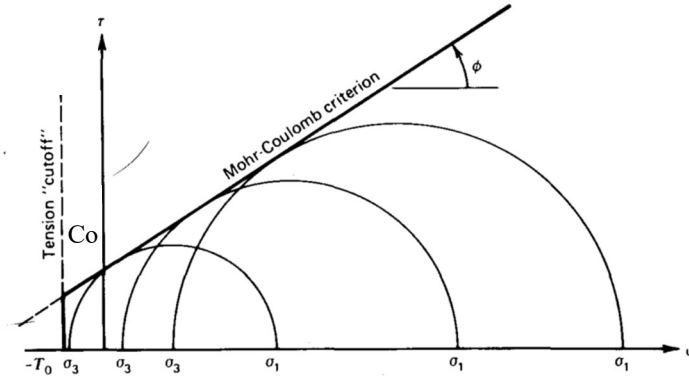
**Figure 2.1. a) Chemical bond break in tension in a microscopic flaw (modified from Eberhardt, 1999). b) Mechanism model of internal crack extension towards the major principal stress.  $\sigma_t$ , major principal stress;  $\tau$ , shear stress. The initial defect is modelled as an elliptical fracture which develops tensile strength concentration at its tips (from Eberhardt et al, 1998).**

In **Figure 2.1b**, new crack growth due to tensile stress, while shear stress is acting in the preexisting flaw. Hoek and Martin (2014) asserts that the failure process is controlled to a very large extent by the intact rock tensile strength or by its component grains. At high confinements, shear failure becomes the dominant process. Griffith (1920) fracture theory was built on the study of manufactured materials (glass), but its application is valid to geological materials as well. In rocks, microcracks and mineral contacts have been identified as the strength-controlling flaws (Hoek and Brown, 1980; Nickislar and Martin, 2014). However, discontinuities of bigger size and with a tensile strength component, such as veins and healed defects, have been acknowledged as controlling factors of rock strength and brittle failure precursors. The increasing inclusion of defects when sample size is increased leads to a decreasing of strength in rocks.

### **2.2.2 The Mohr-Coulomb and Hoek and Brown failure criterion**

The most widely used failure criteria to characterize rock strength are Mohr-Coulomb (MC) and Hoek and Brown (1980). Both criteria map the peak strength values and can be represented in the  $\sigma_1$ - $\sigma_3$  stress space. They correspond to phenomenological descriptions of the failure, based on observations at large scales (Eberhardt, 1998), addressing the rock peak stress related to the minor stress. As phenomenological descriptions, these two failure criteria can be applied to non-upscaled or upscaled properties, proper application of which depends on the engineering judgement.

The M-C relationship is the simplest and most used of the available failure criteria. It is a linear relationship traced tangent to Mohr's circles depicting the principal stresses at failure (Goodman, 1989). It is normally represented in the "normal stress - shear stress" space (**Figure 2.2**), which allows an intuitive understanding of the cohesion and internal friction angle components of the MC criterion.



**Figure 2.2. The Mohr-Coulomb failure criterion in the normal stress ( $\sigma$ ) - shear stress ( $\tau$ ) space. The MC envelope is tangent to Mohr's circles (modified from Goodman, 1989).**

Equation 2.1 corresponds to the MC failure criterion; normal stress is expressed as  $\sigma_n$ , while  $\tau$  is the shear strength. Cohesion ( $C_o$ ) corresponds to the shear strength of the rock at normal stress equal to zero. Internal friction angle ( $\phi$ ) corresponds to the slope of the envelope and describes the increasing of peak shear strength ( $\tau$ ) with normal stress ( $\sigma_n$ ).

$$\tau = C_o + \sigma_n \tan \phi \quad (2.1)$$

The MC criterion loses its physical sense in the tensile area since there cannot be development of shear strength when the normal stress is tensile. Therefore, the intercept of the MC envelope in the normal axis does not have represent the actual tensile strength. To overcome this limitation of the criterion, a tensile cutoff is applied as shown in **Figure 2.2**.

The Hoek and Brown (2019) failure criterion and associated Geological Strength Index (GSI) is probably the most widely used criterion to characterize intact rock and rock mass strength. It was created in 1980 (Hoek and Brown, 1980) by adjusting a curve based on Griffith's theory for the tensile stresses and to laboratory strength data for brittle failure under normal stresses. Hoek and Brown's (H&B) failure criterion relates principal stresses at failure using non-linear equations. Experience gained through the use of the original H&B's equations led to generalized H&B failure criterion (Hoek, 1994 and Hoek et al., 1995) in equations 2.2 to 2.5.







$$\sigma'_1 = \sigma'_3 + \sigma_{ci} \left( m_b \frac{\sigma'_3}{\sigma_{ci}} + S \right)^a \quad (2.2)$$

$$m_b = m_i \exp \left( \frac{GSI-100}{24-14D} \right) \quad (2.3)$$

$$S = \exp \left( \frac{GSI-100}{9-3D} \right) \quad (2.4)$$

$$a = \frac{1}{2} + \frac{1}{6} \left( e^{-\frac{GSI}{15}} + e^{-\frac{20}{3}} \right) \quad (2.5)$$

The factors  $m_b$ ,  $s$  and  $a$  are rock mass material constants. For intact rock  $m_b=m_i$ ,  $s=1$ ,  $a=0.5$ ,  $\sigma_{ci}$  corresponds to the unconfined compression strength. The  $m_i$  constant and  $\sigma_{ci}$  are obtained by adjusting equation 2 to the average UCS and triaxial laboratory test (Hoek and Brown, 2018). The H&B works under the assumption that the material is isotropic, at scales where the effect of individual discontinuities has a negligible effect on the intact rock or rock mass strength. GSI and D variables in equations 3 to 5 correspond to factors related to rock mass. GSI address the two main factors influencing the shear strength of rock masses: Blockiness and condition of joints. GSI can be obtained from the GSI chart based on field qualitative observations (**Figure 2.3**). The chart based GSI was intended as a first approach to rock mass characterization, to be later refined with further site investigation, back analysis and numerical modelling (Hoek and Brown, 2018). In the experience of the author, GSI can become a source of ambiguity and conflict when due training of practitioners and quality of the mapping is not ensured. Given its inherent subjectivity, various authors created quantitative approaches to obtain GSI (Sonmez and Ulusay, 2002, Cai et al, 2004, Hoek et al, 2013). Duran (2017) offers a comprehensive review of the different methods for GSI calculation.

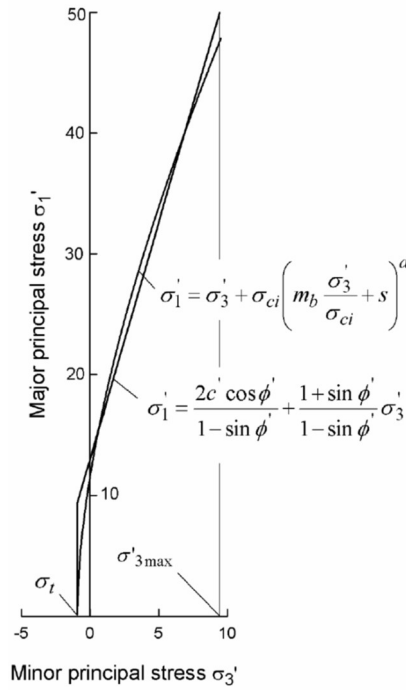
<p><b>GEOLOGICAL STRENGTH INDEX FOR JOINTED ROCKS</b> (Hoek and Marinos, 2000)</p> <p>From the lithology, structure and surface conditions of the discontinuities, estimate the average value of GSI. Do not try to be too precise. Quoting a range from 33 to 37 is more realistic than stating that GSI = 35. Note that the table does not apply to structurally controlled failures. Where weak planar structural planes are present in an unfavourable orientation with respect to the excavation face, these will dominate the rock mass behaviour. The shear strength of surfaces in rocks that are prone to deterioration as a result of changes in moisture content will be reduced if water is present. When working with rocks in the fair to very poor categories, a shift to the right may be made for wet conditions. Water pressure is dealt with by effective stress analysis.</p>		<p><b>SURFACE CONDITIONS</b></p> <p><b>VERY GOOD</b> Very rough, fresh unweathered surfaces</p> <p><b>GOOD</b> Rough, slightly weathered, iron stained surfaces</p> <p><b>FAIR</b> Smooth, moderately weathered and altered surfaces</p> <p><b>POOR</b> Slackensided, highly weathered surfaces with compact coatings or fillings or angular fragments</p> <p><b>VERY POOR</b> Slackensided, highly weathered surfaces with soft clay coatings or fillings</p>							
<p><b>STRUCTURE</b></p>		<p><b>DECREASING SURFACE QUALITY</b> →</p>							
	<p><b>INTACT OR MASSIVE</b> - intact rock specimens or massive in situ rock with few widely spaced discontinuities</p>	<p><b>DECREASING INTERLOCKING OF ROCK PIECES</b></p> <p>↓</p>	90			N/A	N/A		
	<p><b>BLOCKY</b> - well interlocked undisturbed rock mass consisting of cubical blocks formed by three intersecting discontinuity sets</p>		80						
	<p><b>VERY BLOCKY</b>- interlocked, partially disturbed mass with multi-faceted angular blocks formed by 4 or more joint sets</p>			70					
	<p><b>BLOCKY/DISTURBED/SEAMY</b> - folded with angular blocks formed by many intersecting discontinuity sets. Persistence of bedding planes or schistosity</p>				60				
	<p><b>DISINTEGRATED</b> - poorly interlocked, heavily broken rock mass with mixture of angular and rounded rock pieces</p>					50			
	<p><b>LAMINATED/SHEARED</b> - Lack of blockiness due to close spacing of weak schistosity or shear planes</p>						40		
							30		
								20	
									10
				N/A	N/A				

**Figure 2.3. Basic GSI chart. A numerical value for GSI is obtained by qualitatively assessing the joint condition and the blockosity (Hoek and Marinos, 2000)**

The disturbance D factor was introduced to take into account blast damage and relaxation and dilation of the rock mass due to stress relaxation. The factor varies from 0 for an undisturbed rock mass to 1. Guidelines related to the factor can be found in Hoek and Brown (2018). This factor is not applied to the whole rock mass but considering a certain depth of damage or relaxation. For small excavations the recommended depth is no more than a few meters (Hoek and Brown, 2018). For open pit slopes, Rose et al (2018), based on DEM modelling, propose the calculation of a rating, their results yield depth of fully disturbed limit of up to 45% of the slope height.

Not all numerical codes have the option to use H&B type material, while MC criterion is most of the time included in software packages. For these cases, an equivalent H&B cohesion and friction angle can be calculated. Given the linearity of MC criterion, there is no actual mathematical

equivalency between MC and the non-linear H&B. Hoek et al 2002, propose equations to calculate cohesion and friction angle for an average fitted relationship, balancing areas above and below the average MC envelope (**Figure 2.4**). The fitted MC is valid for a specific range of confinement ( $\sigma_3'$ ) that must be set in accordance with the problem to be addressed. Hoek et al (2002) offer guidelines for the maximum confinement  $\sigma_3'$  to be used for tunnels and slopes. This process can be performed in software Rocdata 5.0 (Rocscience, 2017). This procedure was applied to H&B envelopes in Chapter 4 and Chapter 5 to be used as input in ELFEN software.



**Figure 2.4. Relationship between H&B and equivalent MC failure criterion in the principal stresses space (Hoek et al, 2002).**

### 2.3 Rock strength scale effect (strength upscaling)

Rock strength upscaling refers to the strength – size relationship. A decreasing trend with size has been commonly verified in laboratory and field scale tests (Lundborg, 1966, Beniaowsky, 1968, Pratt et al, 1972, Bandis, 1990, Cunha, 1990, Jackson and Lau, 1990, Beran, 2017, among others). This strength decreasing tendency corresponds to rock strength scale effect. Although no scale



effect has been reported in some cases (Thuro et al, 2001), the decreasing strength-size trend is an accepted characteristic of rocks. The reduction of strength with size is explained by the greater probability of including a larger number of defects in bigger samples. Those defects will act as a stress concentrators and crack precursors, following the mechanic of brittle failure showed in **Figure 2.1**.

Hoek and Brown (1980) offer one of the most referenced compilations of uniaxial compression strength (UCS) vs size data. In their work, UCS data of intact rock from samples of similar shape is used to derive an approximate relationship with an exponent equal to 0.18. This relationship covers unjointed samples with a diameter up to 200 mm. This relationship and its exponents are often used when no other data is available. More recently, Yoshinaka *et al* (2008) studied rock mechanical parameters considering the scale effect. In their study, Yoshinaka *et al* concluded that scale effect for UCS depends of the characteristics of the rock type and can be modelled mathematically using a power function. For elastic properties, Young's modulus and Poisson ratio, the scale effect is minimal to non-existent. Yoshinaka's power function is based on Weibull's statistical theory of failure (1951) and can be considered a generalization of Hoek and Brown's mathematical expression. Equation 2.6 shows the power function:

$$\sigma_c/\sigma_{c0} = (d_c/d_{e0})^{-k} \quad (2.6)$$

**Equation 2.6** is intended to obtain an approximated result when samples of different shapes are used, thus parameter  $d_c = V^{1/3}$  (V stands for volume) while  $d_{e0} = 58.1 \text{ mm}$ , which is equivalent diameter to a sample of 50x100 mm. Parameters  $\sigma_c$  and  $\sigma_{c0}$  are the respective UCS. For use with samples of the same shape,  $d_c$  and  $d_{e0}$  can be replaced by samples diameter. The k power determines the drop of strength with size. This strength upscaling function will be revisited in Chapter 4 where it is used to characterize the strength of SR numerical samples of the defected rock. **Figure 2.5** shows both the Hoek and Brown (1980) test compilation and an application of Yoshinaka's power function to laboratory test. Data compiled by Yoshinaka shows that the scale effect can be more pronounced than the compilation made by Hoek and Brown, with a scale effect up to 20% of the laboratory strength.

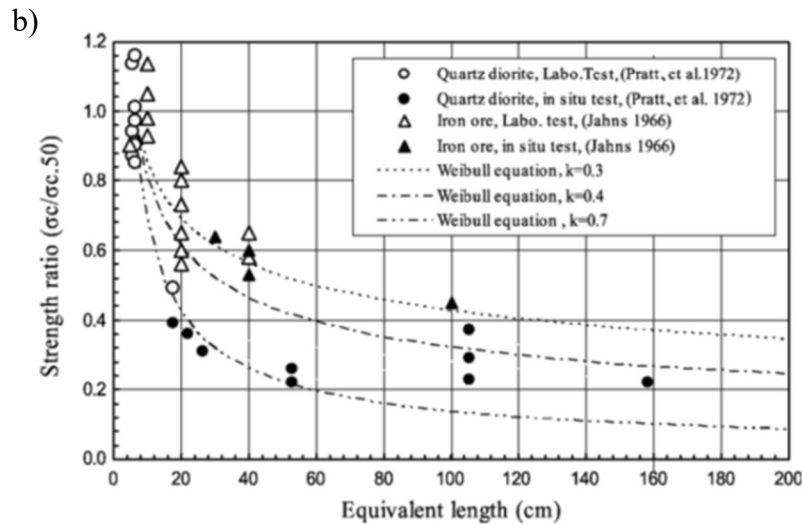
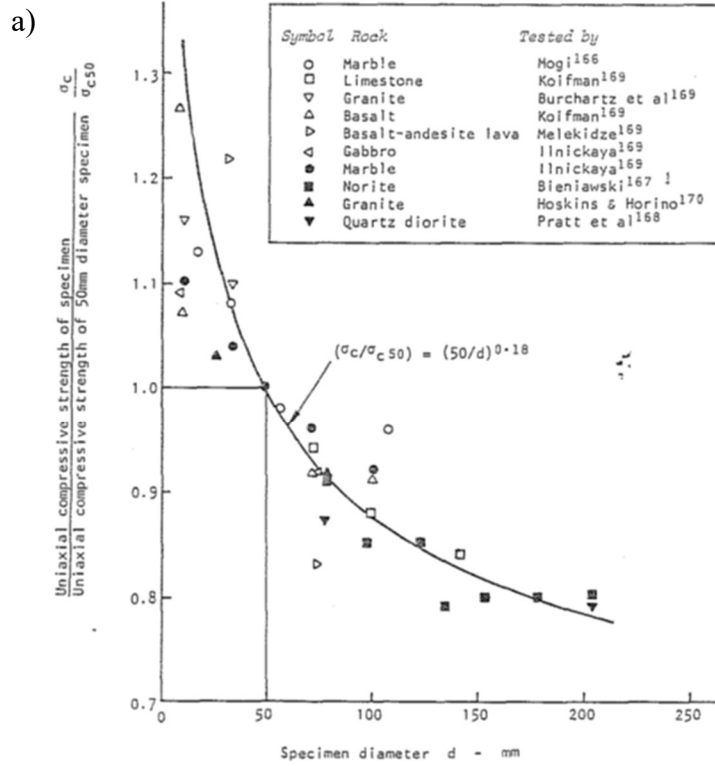


Figure 2.5. Hoek and Brown (1981) UCS data compilation (a) and application of Yoshinaka *et al* (2008) power function to UCS laboratory test (b) (from Yoshinaka *et al*, 2008, after Pratt *et al* 1972). Note that (a) suggests a single exponent equal to 0.18 for different types of rock, while Yoshinaka's power function application in (b) uses  $k$  exponents depending on the rock type.

Although Equation 1 seems to be the natural evolution of the more specific relationship suggested by Hoek and Brown (1980), in practice the strength scale effect is not specifically assessed all the time for the rock type. Hoek and Brown (2019) highlights the importance of the rock block strength in comparison to laboratory strength at scale of 50 mm diameter samples. They refer to data presented in **Figure 2.5a** and in general to the estimation of intact rock strength in the following manner:

*“In the preceding discussion (strength - size considerations), it has been assumed that the intact rock specimens are homogeneous and isotropic and that the values of the unconfined compressive strength  $\sigma_{ci}$  and the constant  $m_i$  are representative of the intact rock in the blocks of the rock mass. In fact, this assumption is not always valid since in many rock masses, defects such as veins, micro-fractures and weathered or altered components can reduce the intact rock strength. Ideally, tests should be carried out on specimens large enough to include representative sections containing these defects, but collection and preparation of such specimens can be challenging.”*

As a corollary, rock block strength is the relevant value to assess rock mass strength. Defects such as veins, alteration and micro-fractures control the rock block strength. The strength drop due to scale effect is specific for the type of rock as showed by Yoshinaka et al, (2008).

Scale effect is not exclusive of defected rocks; jointed rock masses show a reduction of strength when sample size increases. Numerical experiments on this topic were performed by Cundall et al (2008), Elmo (2012) and Farahmand (2017).

### **2.3.1 Defects and Rock Block Strength**

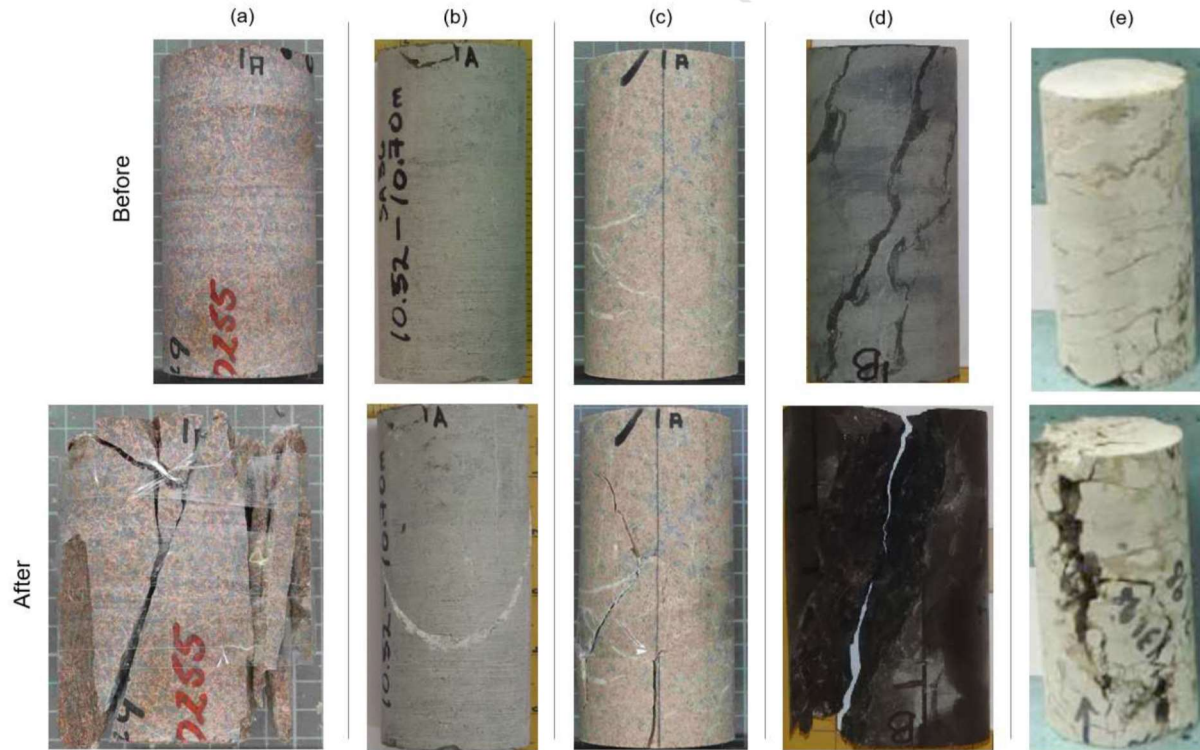
Structural defects are defined by Read, Jakubec and Beale (in read and Stacey, 2009) as “any natural defect in the rock mass that has zero or low tensile strength. This includes Joints, faults, bedding planes and weathered or altered zones”, in summary any discontinuity that can reduce the rock block or rock mass strength significantly. For engineering design, any discontinuity of significant occurrence (intensity) that is not accounted in the rock mass strength estimation and can reduce the strength should be considered for rock block strength estimation (**Figure 2.6**).



**Figure 2.6. Influence of defects intensity in the intact rock strength estimation. Is not uncommon that, as in the case in the central and right photographs, defects are difficult to assign to any type of geological feature. IRS: Intact Rock Strength (From Jakubec, 2013).**

Ideally, rock block strength can be estimated directly from a laboratory test on specimens large enough to be representative of the joint bounded rock. This is rarely possible due to technical and/or economical constraints, and laboratory sample size is most of the time much less than the rock block size. However, a laboratory test performed on these samples is of prime value when the sample break type is properly assessed. This information is basic to estimate strength upscaled to rock block. Without mentioning the concept of rock block strength in their work, Russo and Hormazabal (2016) propose a classification of laboratory tests based on sample break type. Then, the combination of a UCS and triaxial laboratory test with break through rock matrix, rock matrix + defect and multiple defects is asserted as valid to characterize the intact rock strength in porphyry copper deposits with the important development of vein stockwork. Kaiser et al (2015) and Bewick et al (2018, 2019), assert the importance of classifying break type of laboratory test (**Figure 2.7**), aimed to characterize rock block and rock mass strength in sparsely jointed rock masses with a GSI >65 for underground excavations.

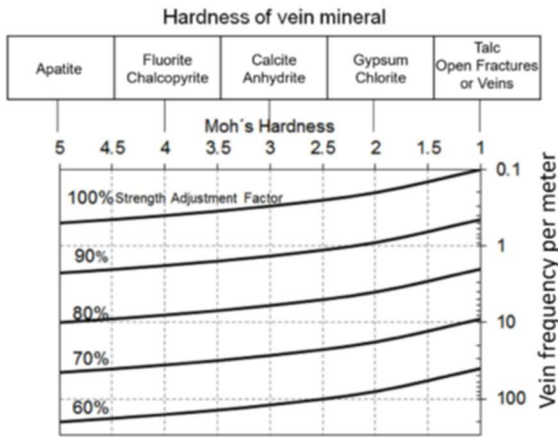
Classification of break type of laboratory test provides information of: i) Intact rock matrix strength, ii) Initial estimation of rock block strength from samples with mixed break (rock matrix + defects) and iii) Defects strength from samples with one defect break. Data from mixed break test can be considered only an initial estimation of rock block strength because this data still needs to be upscaled to a bigger size to be representative of the rock block. Laboratory confined test data from samples with a single defect break can be used to estimate defects strength applying the methodology proposed by Goodman (1998). Laboratory test data classified by break type is used in Chapter 3 to characterize the strength of a defected rock.



**Figure 2.7. Failure types in veined laboratory test specimens before and after testing (from Bewick et al., 2018): (a) homogeneous break via splitting; (b) homogeneous break via shear rupture; (c) combined break; (d) discrete vein break; and (e) break around/along veins, clasts or nodules.**

When no laboratory test is available, methods based on field data can be applied to estimate rock block strength. Laubscher and Jakubec (2000) present an empirical method to estimate rock block strength based on defect intensity and Moh's hardness of their infill. With this method intact rock strength can be reduced by up to 40% (**Figure 2.8a**). Day et al (2012) and Day (2016) propose to modify Hoek and Brown's GSI to include the "intra block structure" to estimate the rock mass strength envelope (**Figure 2.8b**). Both methods, Laubscher and Jakubec (2000) and Day (2016), were applied to data used in this thesis, the results of which are presented in Chapter 4. As asserted by other authors (Pierce, 2009, Bewick et al, 2018), Laubscher and Jakubec's empirical method seems to be appropriate to obtain approximated values of rock block strength. Day's method did not show much upscaling effect when applied to strength data used in Chapter 4.

a)



b)



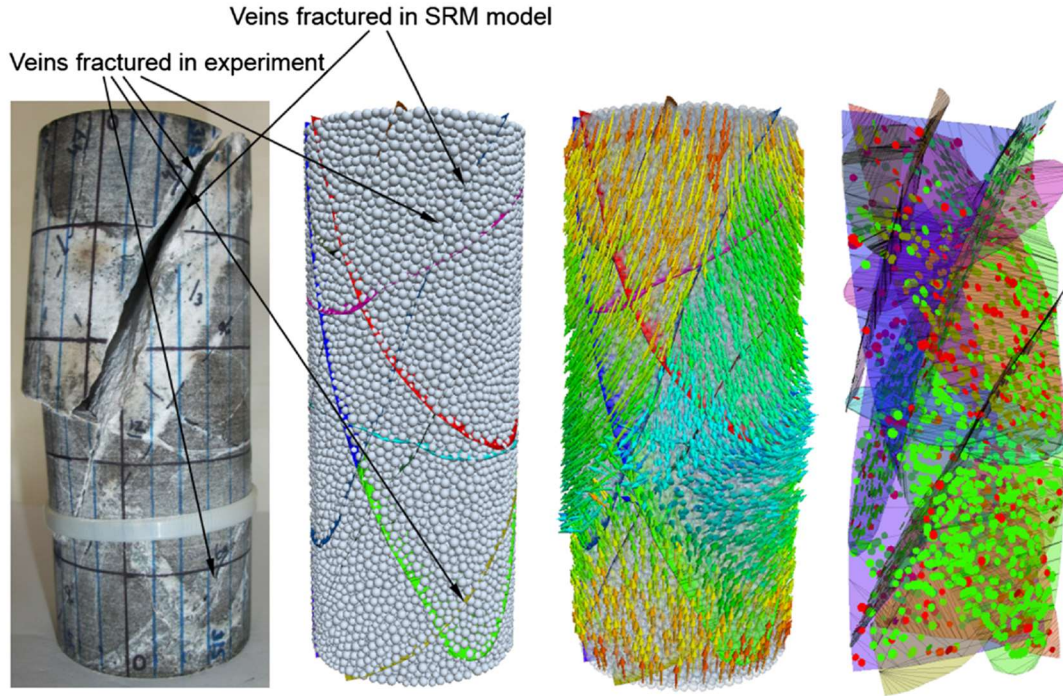
**Figure 2.8. a) Adjustment factor to determine rock block strength based on Laubscher and Jakubec (2000) procedure (from Bewick et al., 2019) b) White arrows indicate joints bounding the “intra block structure” included in Day’s Compound GSI (modified from Day et al., 2012).**

For underground excavations where GSI is applicable, *i.e.* rock block size is approximately 1/10 of excavation span, Bewick et al (2019) propose the direct use of uniaxial rock block strength  $\sigma_{bl}$  instead of intact rock block strength  $\sigma_{ci}$  in H&B’s failure criterion. In such case,  $m_i$  factor is replaced by rock block  $m_{bl}$  obtained from veined laboratory specimens or estimated in the range  $1.3-1.9 \cdot m_i$  when laboratory data is not available (Bewick et al, 2019).

## 2.4 Synthetic Rock numerical modelling

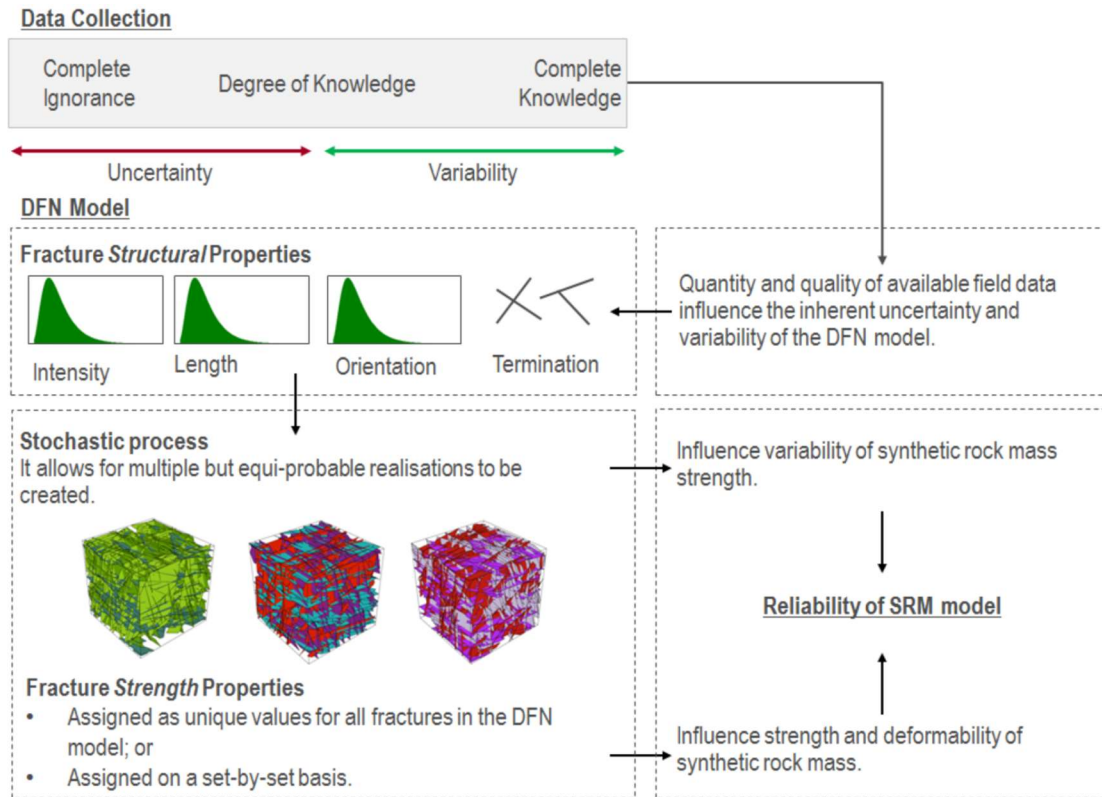
The Synthetic Rock (SR), or Synthetic Rock Mass (SRM), is a numerical approach to simulate the mechanical behavior of rocks with discontinuities. In its classical application it consists of a numerical sample, bi or tri-dimensional, that is submitted to a test that simulates a real laboratory experiment. Then, stress – strain curves, fragmentation of the sample and other measurements can be obtained to characterize the rock strength. The SR couples the rock matrix, for which representation and discretization depends on the numerical method to be used, and a Discrete Fracture Network (DFN). The DFN can replicate discontinuities in a real sample (**Figure 2.9**) or address the DFN statistically, building SR samples for a series of DFN realizations.





**Figure 2.9.** An example of Synthetic Rock that emulates a real sample submitted to biaxial compression test (from Turichshev and Hadjigeorgiou, 2015)

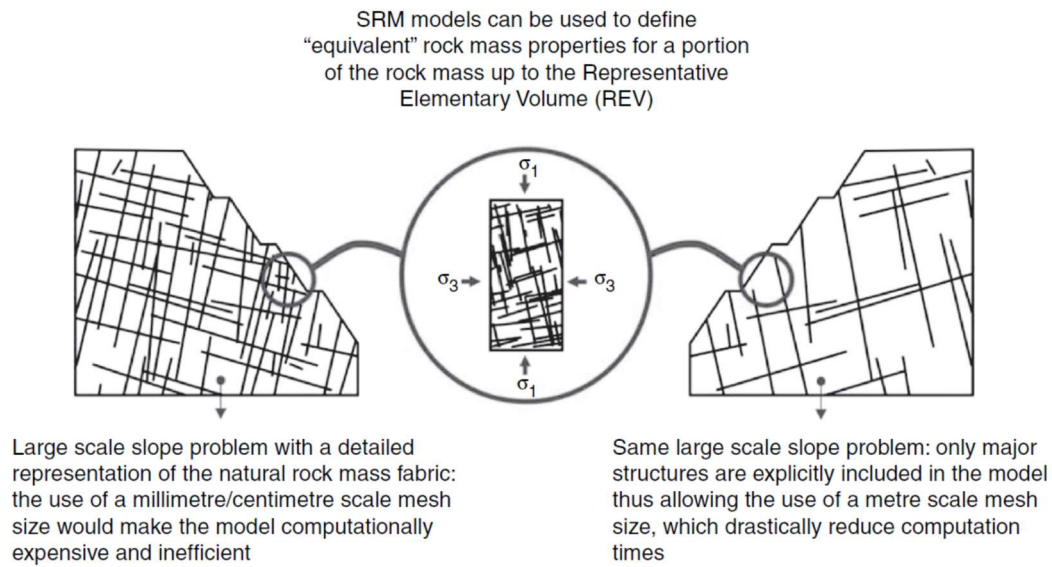
The construction of a DFN is a constant for all the SR types of analysis. Unless the aim of the SR is replicate deterministic discontinuities, as the case in **Figure 2.9**, the embedded fractures correspond to a realization of a stochastic DFN model. In this case the SR analysis becomes stochastic, which implies performing a number of numerical experiments to address the variability of the SR strength. **Figure 2.10** shows the main considerations for this case.



**Figure 2.10. Key aspects of DFN modelling and implication for SRM (Elmo et al, 2016)**

Given the state-of-the-art of numerical modelling, to address the multiple scales at which brittle failure occur is technically not possible when rock mass is evaluated at large size, for instance in a slope. To encompass from a micro scale of randomly distributed cracks and mineral contacts, to an intermediate scale of healed defects up to the size of joints is computationally unpractical due to the size/number of elements necessary for a mesh of such detail. Thus, the SR approach allows scale up rock (or rock mass) properties to implicitly include those geological features that cannot be included in a model due to computational limitations (Elmo and Stead, 2017). The small scale features are implicitly accounted in the physical properties of the equivalent continuum in the model (**Figure 2.11**).





**Figure 2.11. Conceptual definition of the use of equivalent continuum rock mass properties to represent small scale fracturing (from Elmo and Stead, 2017). The same equivalent continuum concept can be applied to SR samples at lower scales.**

The equivalent continuum concept applied to a rock mass in **Figure 2.11** can be used at smaller scales as well. For example, in an SR sample with veins explicitly represented, the mechanical properties in the numerical rock matrix are implicitly accounting for the strength and interaction of all mineral grains, mineral contacts and potential micro flaws that the real rock may contain.

The effect of upscaled rock strength in the stability assessment and engineering design of major excavations is not well documented in literature. The numerical analysis in this thesis is intended to cover this topic.

#### **2.4.1 Numerical discontinuum approach for SR**

The three main approaches used for SR simulations are:

- Particle Flow Code (PFC): The intact rock is simulated with a bonded particle method (BPM) where rigid particles are bonded together at their contacts (Potyondy and Cundall, 2004). Micro stiffness and micro strength are adjusted to replicate the strength response at a macro scale (Pierce 2009). Sliding Joint model is applied to discontinuities (**Figure 2.12**)

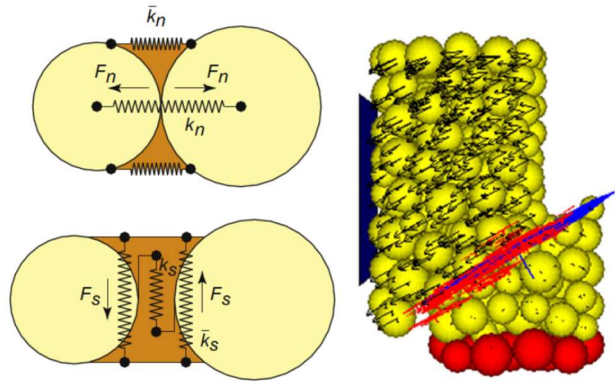


Figure 2.12. PFC particle bond and sliding joint model (Elmo et al, 2016).

- Distinct Element Method (DEM) coupled with Voronoi tessellation: The rock is divided into polygonal grains, hence the name grain based model (GBM). Like Bonded particle method, microproperties are calibrated to achieve the macroscopical rock strength (**Figure 2.13**). This method is especially suited when mineral grains in the SR sample are modelled individually (Hoek and Martin, 2014, Farahmand, 2017)

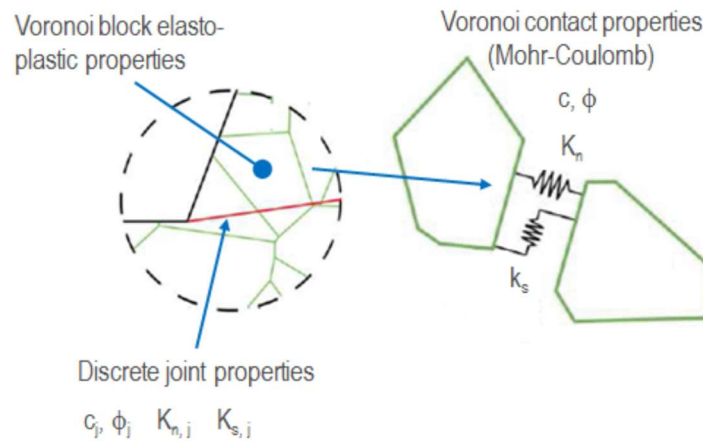


Figure 2.13. Voronoi method implemented into DEM models (Elmo et al, 2016).

- Hybrid Finite-Distinct Element Model (FDEM): These types of models allow the transition from continuum to discontinuum combining a finite element - distinct element approach. These models incorporate fracture mechanics and can simulate crack initiation, propagation and coalescence, with the development of new cracks in Mode I (tensile)

and/or Mode II (shear). Depending of the code, cracks can develop upon only elements contact, or through elements applying an adaptative remeshing algorithm.

The realistic fracture mechanics and capability of reproducing the macro strength of materials with little calibration of input properties make FDEM codes attractive for SR numerical modelling. Hybrid FDEM codes have been used successfully in SR modelling of rock masses (Elmo, 2006, Hamdi 2015, Schlotfeldt *et al*, 2017) and intact rock with defects (Tatone and Grasselli, 2015, Hamdi 2015, Karimi *et al* 2016). The FDEM code ELFEN 4.7 (Rockfield, 2013) was used to perform the SR numerical experiments in Chapter 4 and part of the slope stability back analysis in Chapter 5. The constitutive model used corresponds to Mohr-Coulomb (MC) coupled with Rankine rotating crack tensile cut off, which overcome the limitations of the MC model to represent failure in tension. The Rankine rotating crack model is based on Mode I failure, realizing a tensile fracture in the mesh topology when principal stress reaches tensile strength. In accordance with brittle fracture mechanics, new fractures align perpendicular to minor principal stress. The newly formed surface interacts with other cracks according to the discrete contact properties assigned to new cracks in the simulation settings. Propagation of fractures is controlled in ELFEN by stress intensity factor related to length of the preexisting or new fractures and fracture energy. Detailed explanation of the constitutive model MC - Rankine rotating crack tensile cut off and contact interaction and detection can be found in Klerck (2000), Munjiza (2004) and Elmo (2006).

#### **2.4.2 Applications of SR to defected rocks**

In its early applications, the synthetic rock numerical modelling was used as mean to assess the mechanical behavior of jointed rock masses at such scales that laboratory test was not possible (Carvalho et al, 2002, Elmo, 2006, Pierce et al, 2007). Later, Pierce et al (2009) appear as one of the first applications of SR modelling to simulate intact rock with defects. In their work, scale effect is assessed for a quartzite with veins in PFC3D code, scale effect is verified, with strength drop becoming more pronounced when veins strength is decreased (**Figure 2.14**).

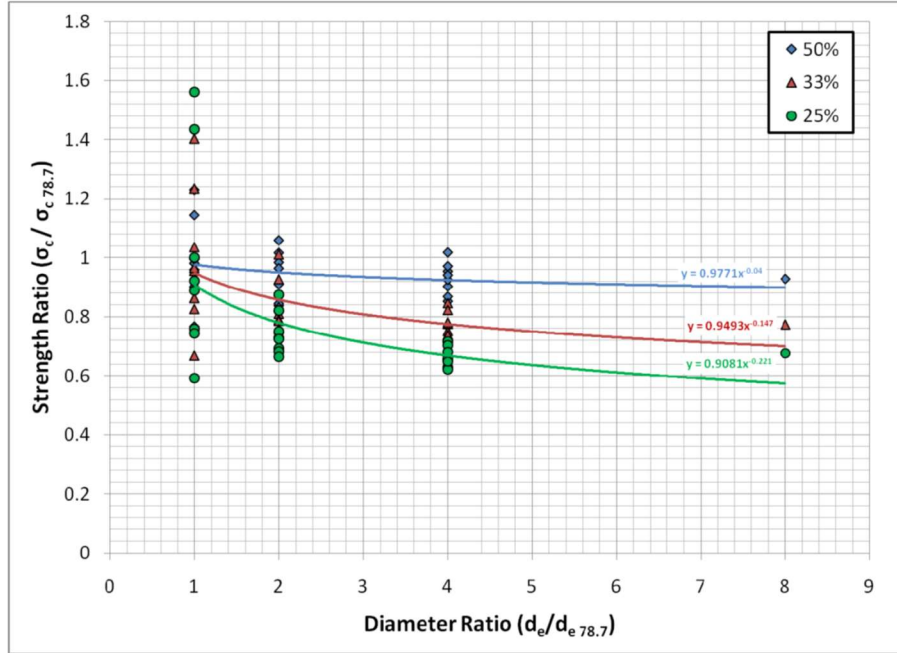
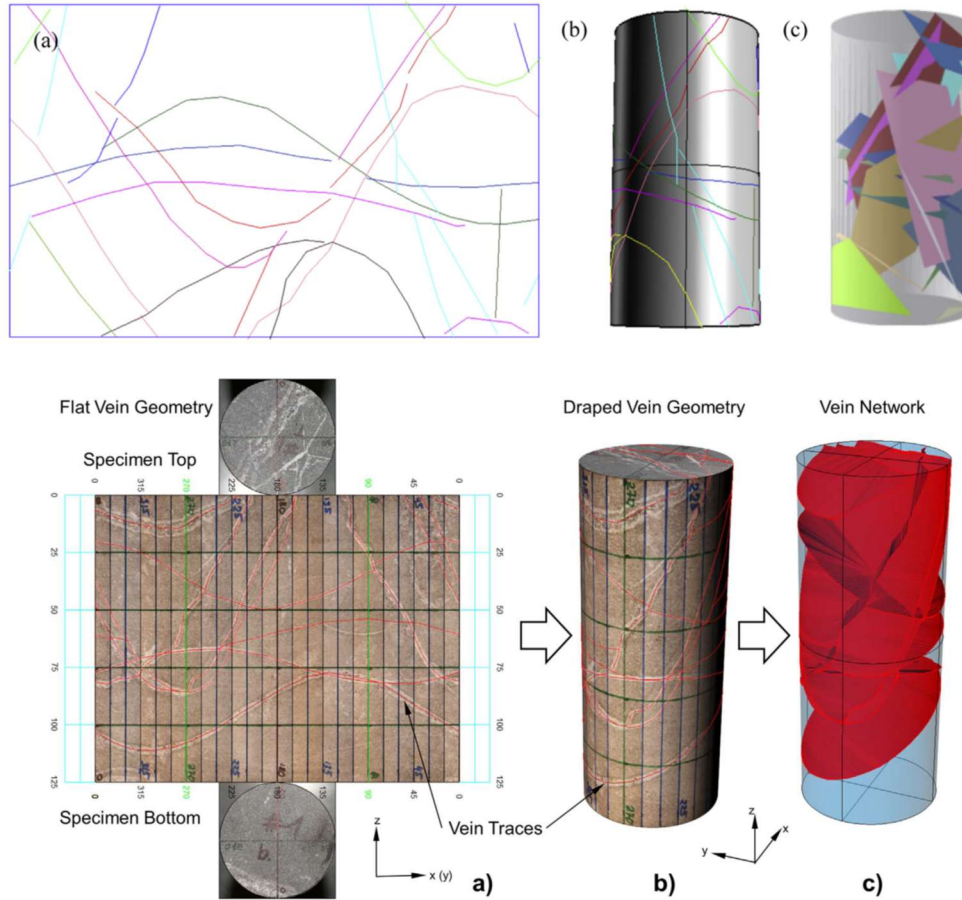


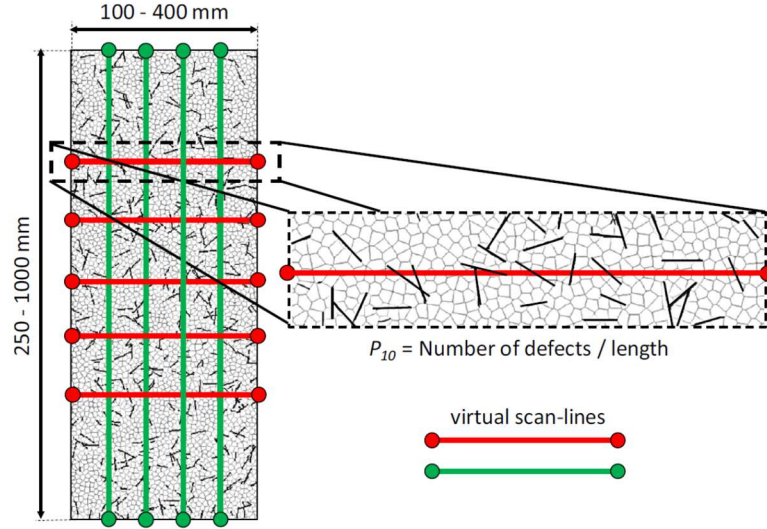
Figure 2.14. Scale effect on SR samples. Scale effect becomes more pronounced as vein strength decrease, percentage indicates vein strength is relative to host rock (from Pierce et al, 2009).

BPM code (PFC) coupled with deterministic DFN have been used by Vallejos et al (2016) and Turichshev and Hadjigeorgiou (2015, 2016), to explicitly reproduce real triaxial test on veined rocks from El Teniente mine (**Figure 2.15**). These authors fairly reproduce the real laboratory tests, showing the primary control of vein strength and geometry on the test outcome. The importance of detailed characterization of vein mineralogy, geometry and mechanical properties is emphasized by both authors. Zhang (2011) assessed scale effect in tridimensional samples in PFC3D with defects without tensile strength; additionally, he proposes a mathematical relationship to characterize scale effect.



**Figure 2.15. SR with deterministic DFN embedded in a BPM were assessed by Vallejos et al (2016) (above) and Turichshev and Hadjigeorgiou (2016) (below). The diameter of samples in both cases is approximately 50 mm.**

Grain Based Models (GBM) has been used to assess scale effect on defected samples as well. Distinct elements UDEC-Voronoi is the most common tool to build and assess the SR samples. Bahrani and Kaiser (2016) used GBM to study scale effect in samples with defects. They found no scale effect for non-defected rocks, and samples with defects show crack orientation and size as the main strength controlling factors. Stavrou et al (2018, 2019) investigate the scale effect and rock block strength in numerical samples with a stochastic micro DFN (**Figure 2.16**). In their work they propose diagrams for estimating the Rock Block Strength as a function of defect intensity, persistence, and strength.



**Figure 2.16.** Micro DFN and Voronoi tessellation used in the work of Stavrou et al (2019). Red and green are virtual scan-lines.

SR performed in FDEM codes has been used for numerical experiments simulating intact rock with defects without tensile strength and mineral grain strength. There were no FDEM including simulation of veins in the literature reviewed. Mahabadi (2012), uses Y-Geo code to replicate Brazilian test on disc of 40 mm of diameter with microcracks and grain heterogeneity, then uses obtained properties as input for UCS numerical test. Mahabadi's work is one of the few SR experiments in literature that couples SR results at multiscale. Hamdi et al (2015) uses ELFEN for SR Brazilian and compression tests on Lac du Bonnet granite including a DFN of microcracks (**Figure 2.17, left**) based on image analysis of thin sections. Unconfined strength and cohesion decrease when micro cracks increase, while friction angle shows no change. Hamdi shows that spalling development in Lac du Bonnet granite is related to microcrack intensity. Karimi et al (2016) uses Irazu and ELFEN to simulate crack propagation in a rock bridge between centimetric defects (**Figure 2.17, right**), then assesses the crack patterns with the aid of proprietary analytical post processing tools.



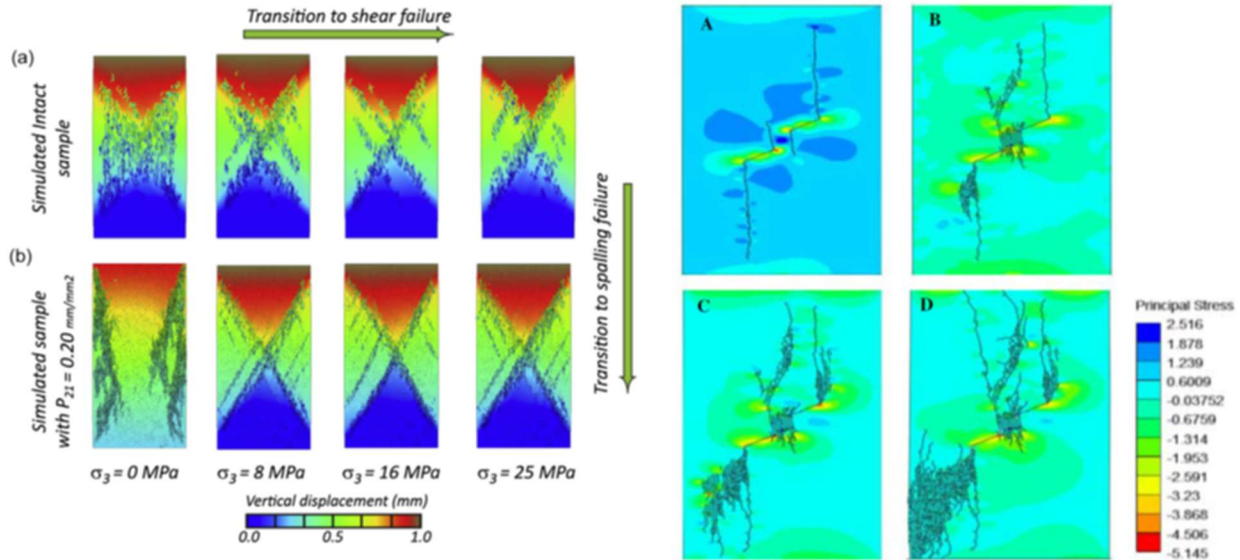
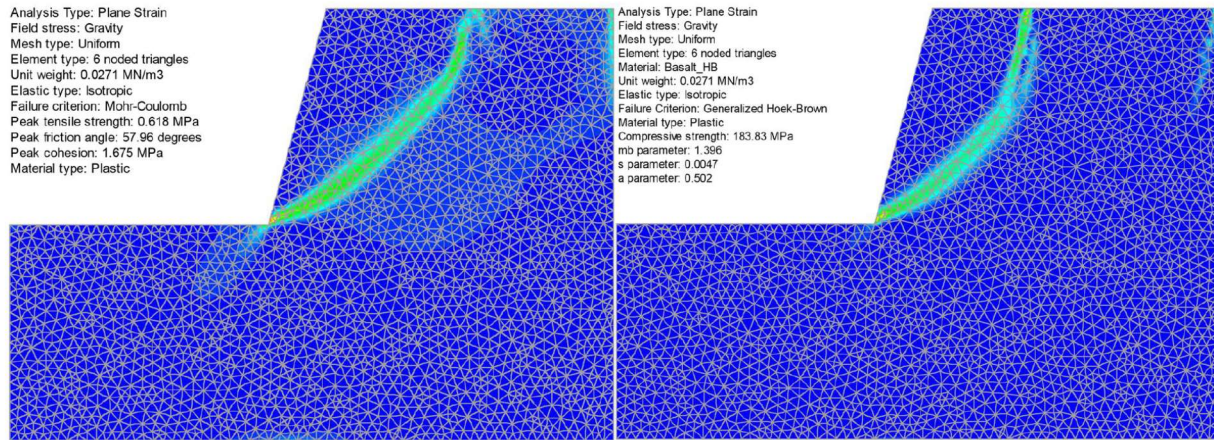


Figure 2.17. SR simulation of defected rock in FDEM code. Hamdi's biaxial test on samples with microdefects on the left (Hamdi et al., 2015) and Karimi et al (2016) rock bridge simulation on the right. Both experiments were developed in ELFEN code.

## 2.5 Slope stability analysis with continuum codes and FDEM codes

In continuum models the material is simulated as an equivalent continuum. Implicit discontinuities can be inserted in continuum models, in which case contact properties are changed to those of the discontinuity but no actual displacement occurs along these fractures. They are normally isotropic, commonly using MC strength parameters to limit the strength that an element can sustain (Lorig et al, in Read and Stacey, 2009). Continuum numerical codes are widely used for slope design, being RS2 (Rocscience, 2019), one of the codes proved successful in the analysis of slope stability. Hammah et al (2007) compared continuum (Phase 2) vs discontinuum (UDEC) codes in the analysis of a slope in rocky block mass, with concordant and credible results. RS2 software allows the application of Shear Strength Reduction (SSR), a simple approach that involves the progressive reduction of strength properties of the rock mass (**Figure 2.18**). Then, Stress Reduction Factor (SRF) indicates the factor at which the slope becomes unstable (Hammah, et al, 2004). SRF and Factor of Safety (FoS) can be considered analogous terms. Given its characteristics, RS2 is especially suited to assess failures in shear controlled by the rock mass. Other common continuum codes are Flac (Itasca), Flac 3D (Itasca) and Abaqus.



**Figure 2.18.** SSR analysis of a slope performed in RS2 (Rocscience). MC (left) and H&B (right) materials can be used in the simulation (Sari, 2019).

Hybrid FDEM codes, and ELFEN software in particular, have been successfully applied to simulate brittle failure of rock slopes (Eberhardt et al, 2004, Stead et al, 2006, Vyazmensky et al. 2010). The possibility of simulating progressive fracturing and the use of DFN representing possible anisotropies introduced by joints, make these codes attractive to simulate brittle failure in rock slopes (Elmo and Stead 2017). The possibility of including a rock fabric from a DFN realization which is an active part of the process of fracturing and block interaction makes FDEM codes more realistic. Computational limitations prevent the use of fracture networks depicting fracture intensity in full when intensity is high, as well as when the model has a great extension. In these cases, equivalent continuum material properties must be calculated to account for the portion of fractures not included in the embedded DFN. Consideration of scale effects, at level of intact rock and jointed rock mass, is of prime importance in such cases. The preferred constitutive model used in ELFEN for rock mechanics simulations is MC with Rankine tensile cut-off. However, linearized H&B equivalent properties can be applied adjusting the tangent MC envelop as described by Hoek *et al* (2002). An example of advanced modelling using FDEM ELFEN code can be found in Vyazmensky et al. 2010 for a case of slope instability triggered by block caving subsidence at Palabora mine (**Figure 2.19**).



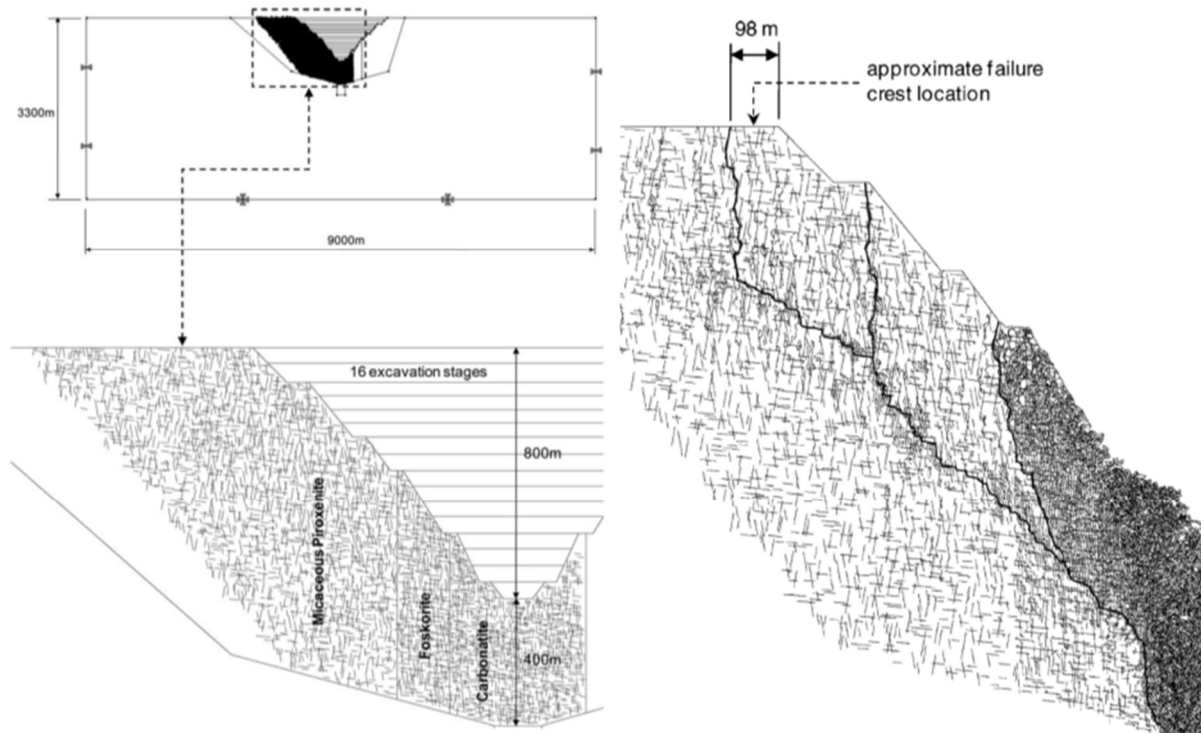


Figure 2.19. Elfen model geometry (left) and pit slope deformation at 40% of caving extraction at Palabora mine. A DFN fabric with variable intensity is included in the slope rock mass (from Vyazmensky et al., 2010)

## 2.6 Conclusion

The strength of brittle rock at low confinements is controlled by defects and tensile stress developed at their tips when the rock is loaded. The strength scale effect is a known characteristic of rocks which is related to the increasing probability of having more defects when size increase. The strength drop due to scale effect is specific for each rock type and depends on the strength and geometry of defects. Brittle rock strength and failure has been successfully studied using SR numerical models on defected rocks. However, there is no record in the reviewed literature of the use of upscaled strength of a rock with defects to assess slope stability or other types of excavation. In general, the appropriate use of upscaled strength in engineering assessment seems to be a topic treated more often in theory than in practice, with some exceptions. This apparent gap in literature is covered in the next chapters. Chapter 3 presents the characterization of the rock matrix, defects and rock mass of a geological unit that hosted a major slope instability. Chapter 4 shows the use

of SR to obtain the specific scale effect of the defected rock. Chapter 5 presents the back analysis of the instability, using the upscaled strength obtained in Chapter 4 to characterize the rock mass strength of the unit that hosted the major slope instability.

## **Chapter 3. Basic Geological and Geotechnical characterization of the Leached rock**

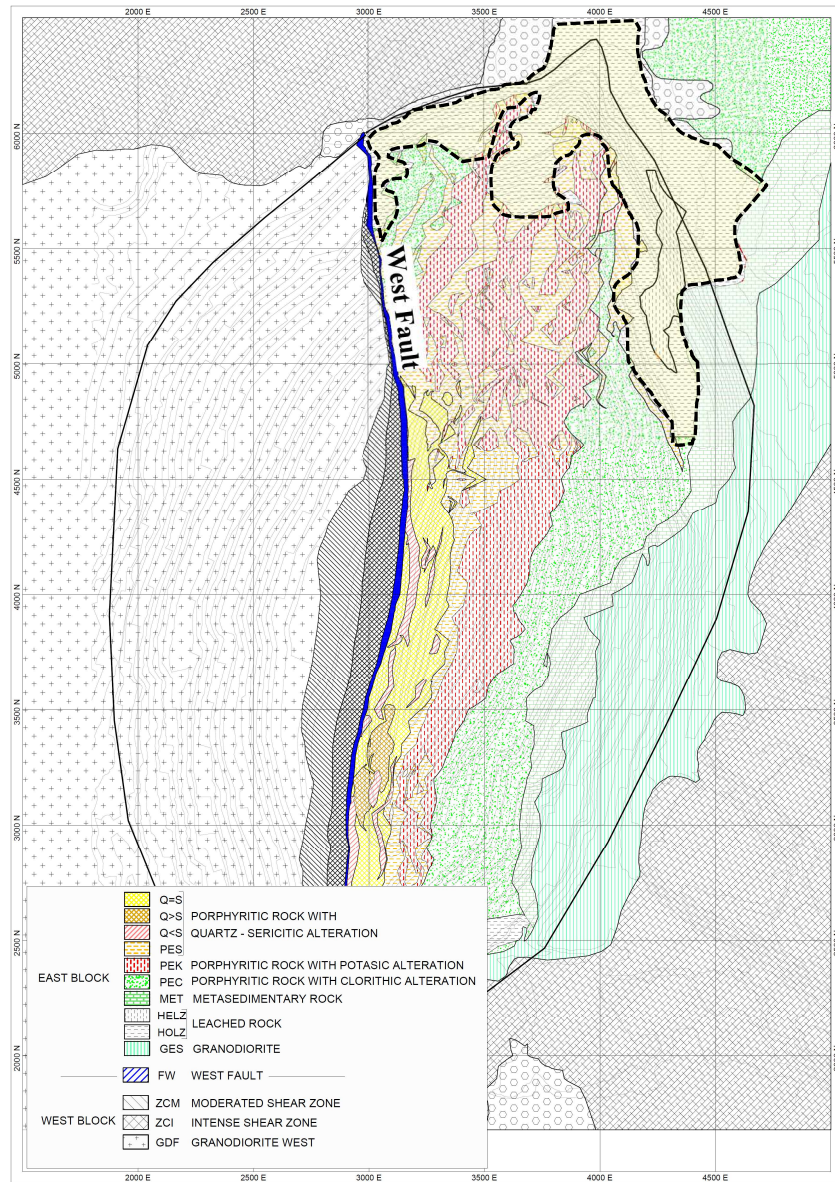
### **3.1 Introduction**

This chapter presents the geological and geotechnical data and characterization used to develop the numerical experiments in Chapter 4 and Chapter 5. The information comes from Chuquicamata mine and is focused on a naturally leached granitic rock with supergene alteration product of percolation of meteoric water. The strength of this leached rock is controlled by abundant healed defects. A major slope failure occurred in this geological unit, for which back analysis was used to assess the suitability of numerically upscaled strength to assess slope stability in the next chapters.

### **3.2 Geological Setting**

#### **3.2.1 The Leached rock in the context of Chuquicamata Mine Geology**

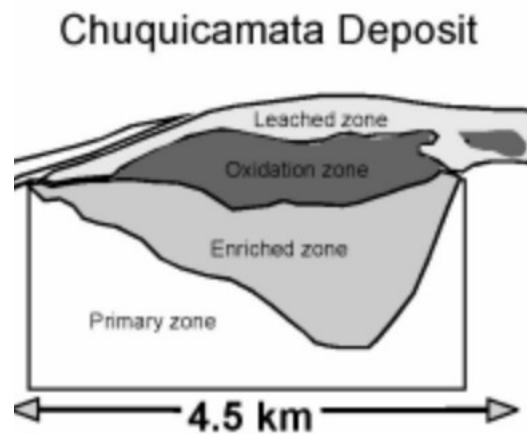
The main geological feature in Chuquicamata mine corresponds to the West Fault, a branch of the 2000 kilometers north-south structural system located in the Chilean pre- Andean mountain range (Tomlinson *et al*, 1994). The West Fault, in Chuquicamata open pit, separates a ~36 Ma non-mineralized Granodiorite in the west from mineralized porphyritic intrusions of 32-30 Ma in the east block (Reuter *et al*, 1993). The host rock in the east block corresponds to a Granite of Paleozoic age. The porphyritic intrusions generated three types of alteration in the host rock: potassic (tardi-magmatic), chloritic and quartz-sericitic. The higher copper grades are located in the central part of the pit, associated with quartz-sericitic alteration. The leached rock, remnant of secondary enrichment, is located in the north-east zone of the pit and is the focus of the geological and geotechnical characterization in this chapter. A shear zone is located at the west, next to the West Fault product to its geological activity. A combination of lithology, alteration and in some cases degree of fracturing and deformation has been applied by Chuquicamata geotechnical department to define the geotechnical units that serve as base of the geotechnical characterization (**Figure 3.1**).



**Figure 3.1. Plan view of geotechnical units in Chuquicamata mine. Pit border in black. The West Fault (in blue) is a hard geological limit between the ore in the east block and waste rock in the west block. The dotted line encloses the leached rock (geology by Chuquicamata mine Superintendency of Geotechnics)**

Between 20 – 15 Ma ago, after porphyritic intrusions that carried the primary mineralization, vertical percolation of meteoric water led to the geological processes of leaching, oxidation and secondary enrichment of Chuquicamata ore body. These processes, called supergene alteration,

produced a zone of copper-rich secondary ores, the secondary enriched zone, which was mined and depleted decades ago. **Figure 3.2** shows a scheme of the supergene zones in Chuquicamata mine.



**Figure 3.2.** Schematic cross section showing the supergene zonation of Chuquicamata mine (modified from Dold, 2003).

Remnants of the supergene leached and oxidized zone, without the commercial content of copper ore, are still located at the north and north-east margins of the pit (**Figure 3.1**). To reach the ore located at lower levels, new pushbacks must be excavated throughout the remnants of the leached rock. During the mining operation, a portion of the leached rock is removed while the rest of it forms part of the newly-excavated slope.

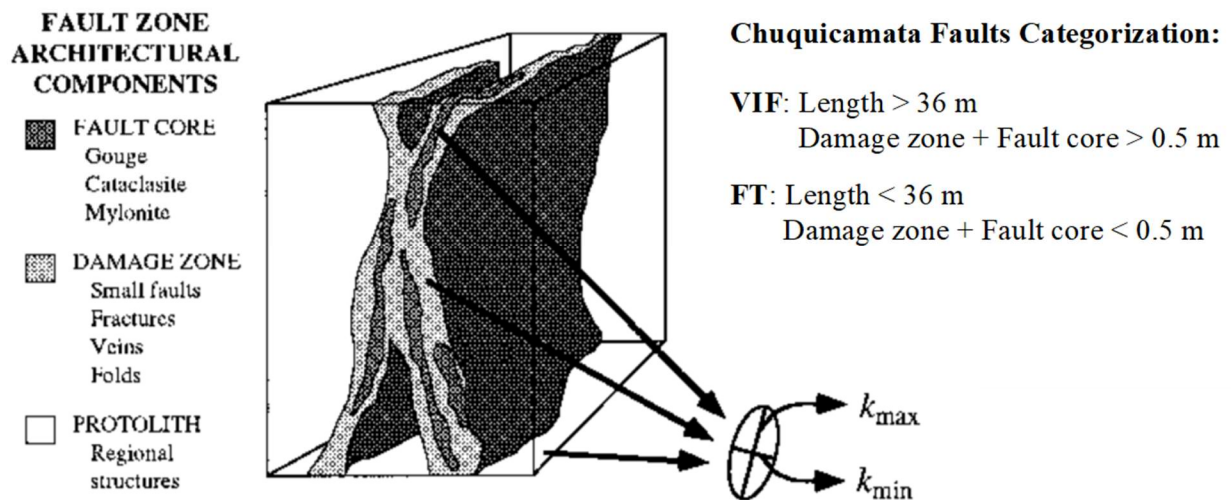
The Leached rock was divided in 2 subunits based on H&B's GSI, namely: Heterogeneous Leached Zone (HELZ) and Homogeneous Leached Zone (HOLZ). A section at the end of this chapter shows the data analysis that supports these subunits. A 250 m height outcrop of Leached rock exposed in the north-east slope of the pit was affected by an inter-ramp failure enclosed in the HELZ. The information presented in this chapter, used as input in Chapter 4 and Chapter 5, comes mainly from this zone.

### 3.2.2 Structural geology of the north east slope

As mentioned, the main structural feature in Chuquicamata mine is the West Fault, a major structural feature of NS azimuth and west dip direction that completely crosses the 4 kms pit. In

accordance with the formerly tectonically-active terrain, there is an abundance of faults in Chuquicamata mine with lengths varying from a few meters to hundreds of meters. Joints in general are congruent with main structural sets.

Along its history of geotechnical characterization, the categorization of faults in Chuquicamata mine has been used as a successful practice that aids the modelling of major continuous faults and the definition of structural domains. The categorization is based in the model of fault architecture proposed by Caine et al (1996). Based on mapped length at the scale of bench, and the width of core zone plus damage faults are classified as Very Important Faults (VIF) or Fault Traces (FT) (**Figure 3.3**). The same categorization is applied to faults logged in drill cores, but, for the obvious limitations of the sampling support, length component was not recorded.

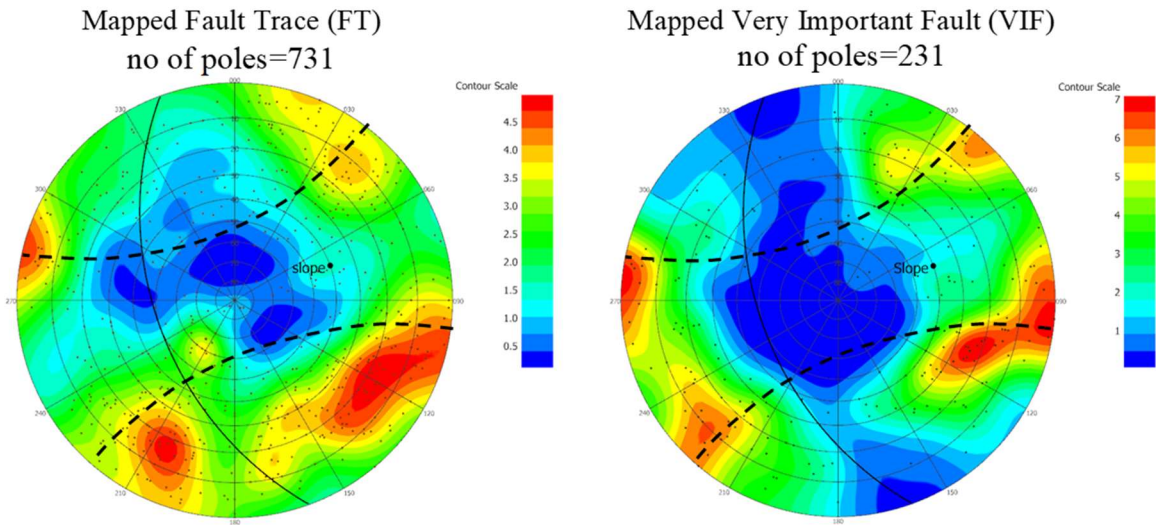


**Figure 3.3.** Fault zone components used to categorize mapped structures in Chuquicamata mine. Fault core + damage zone, together with mapped continuity are used to classify the faults as VIF or FT, as indicated in the figure (modified from Caine et al, 1996).

Faults from bench scanline mapping, collected in the north east section of the pit slope where the leached unit is located, are presented in **Figure 3.4**. For VIF faults, the main structural directions (azimuth) are north-south and north-west, while for FT the main structural directions are north - west, approximately coincident with one of the VIF sets, and north-east. The history of instabilities in Chuquicamata mine showed that 30° parallelism criteria is appropriate to address Planar faults.



Both daylighting and non-daylighting Planar faults played an important role in the stability of the north east slope and the Leached unit, with VIF and FT partially controlling instabilities at the scale of single bench and inter-ramp.

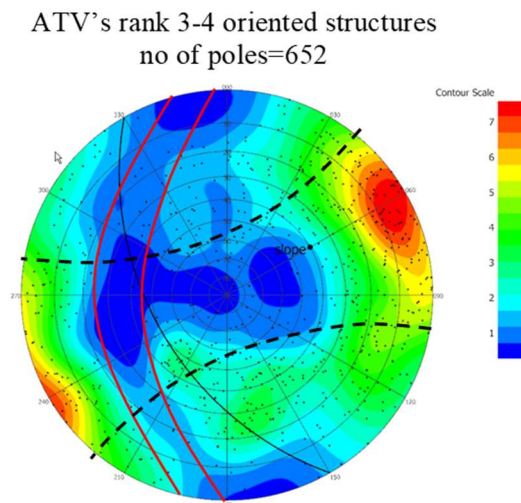


**Figure 3.4.** Stereonets of faults mapped in bench scanline. Great circle for north-east slope is included as a reference together with planar limits (dotted line in black).

Structures oriented using Acoustic Televiwer (ATV) geophysical record were available for part of the drillholes located in the Leached unit. Being a record of an acoustic signal, ATV's structures are categorized based on the "visibility" of the discontinuity in the travel time log regarding their continuity in the hole wall and width. A rank 1 is assigned to the less visible, thin and discontinuous features, while a rank 4 is assigned to the thick, fully continuous traces in the travel time log. In general, when no further drill core logging /ATV correlation is available, some assumptions can be made, rank 1-2 features corresponding to joints and minor structures (defects and centimetric cracks and joints), and rank 3-4 corresponding to joints and faults. Some mixing of structures categories occurs between ranks. Depending on local conditions of the rock mass, the counting (intensity) of discontinuities could not correlate exactly with the core logging, the latter being more reliable for intensity data.

**Figure 3.5** shows the stereonet for ATV oriented structures of ranks 3-4, which are assumed to be VIF and FT faults. The poles concentration is approximately concordant with VIF and FT faults.

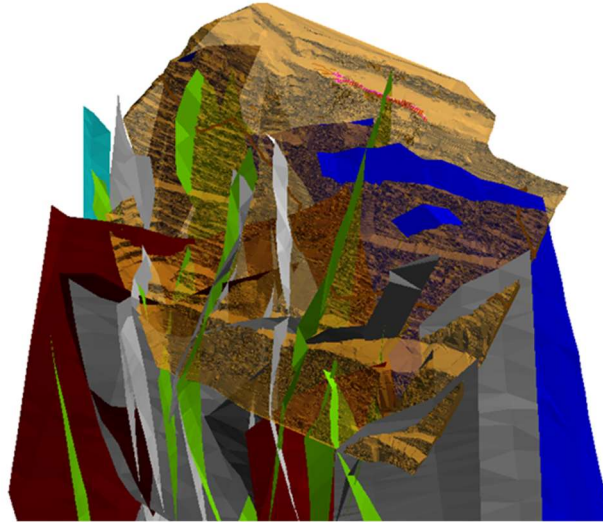
structural set of north-west orientation from bench mapping. Most of the drillholes were drilled in a west to east direction, dipping 60° towards east. This generates a blind zone (red lines in **Figure 3.5**), and a bias that cannot be removed with anything other than new measurements in drillholes with different orientation. Thus, this ATV information is useful to model major faults (tying structures intercepted in different drillholes) but biased for frequentist orientation analysis.



**Figure 3.5.** Structures with rank 3-4 are interpreted in ATV record as faults VIF and FT. A blind zone, delimited with red lines, is formed due to preferential drilling of holes. Only one planar, non-daylighting set is defined by poles concentration; the absence of other structural sets is likely due to bias related to the orientation of drillholes.

Bench mapped VIF faults, together with ATV structures with rank 3-4 were used by the Chuquicamata geotechnical department to model the major faults with continuities of tens to hundreds of meters. The tridimensional surfaces of major faults (**Figure 3.6**) were used in this research as explicit faults in the back analysis in Chapter 5.

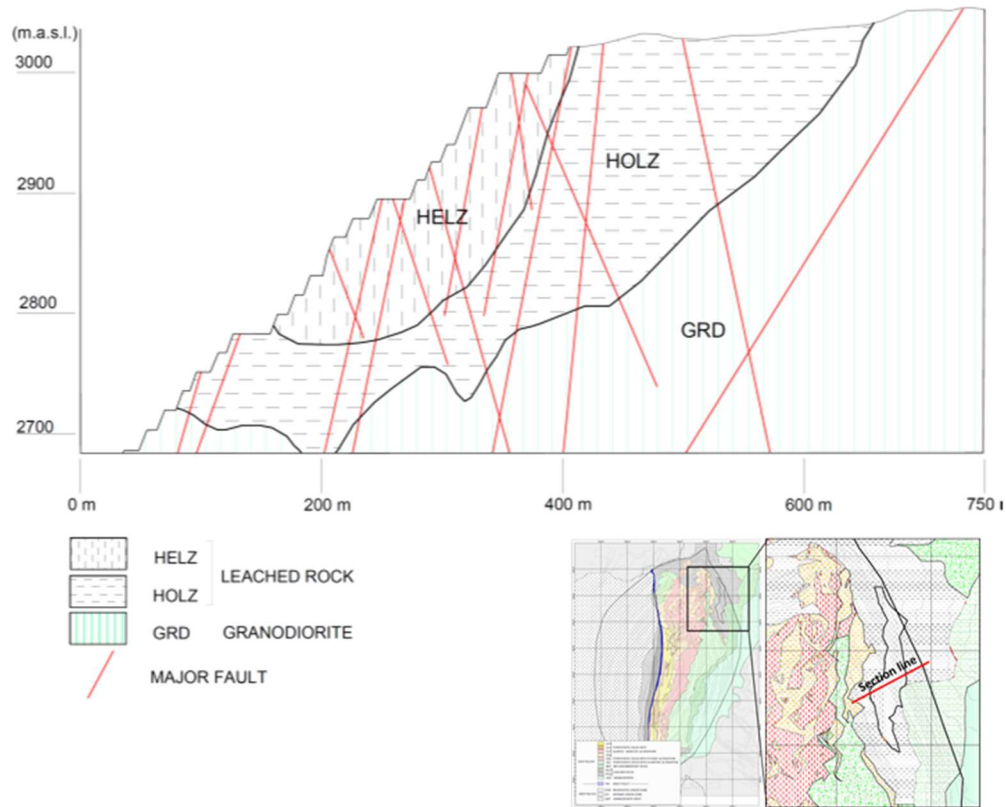




**Figure 3.6.** Tridimensional wireframes of major structures in the north-east slope, in the leached rock and surrounding units. Bench scanline mapping of VIFs and drillhole's interception of faults, oriented with ATV, are the supporting information.

### 3.2.3 Geology of the Leached geological unit

The leached rock is a product of the secondary enrichment of the ore body, with physical properties determined mainly by the alteration byproducts of this geological process. The geological enrichment process is characterized by the oxidation of primary ores (mostly Chalcopirite and Pyrite) which in turn produces the acidification of meteoric waters, leading to the leaching of primary minerals. Thus, the copper-rich solution migrates vertically, depositing the copper as secondary oxides and sulphide minerals at lower levels. The result is the vertical zonation presented in **Figure 3.2**. The Leached geological unit in this work is a remnant of the leached upper zone and is located in the periphery of Chuquicamata deposit. With the aim of separating the weaker and more fractured zones in the Leached rock, the unit was split in two sub-units based on H&B's GSI, the heterogeneous leached zone (HELZ) and homogeneous leached zone (HOLZ). **Figure 3.7** show a cross section of Chuquicamata mine in the area of the pit where the leached geological unit daylights.



**Figure 3.7. Cross section of the leached unit. This cross section is used in Chapter 5 to back analyze the slope instability that occurred in the leached rock.**

The lithology of the Leached unit (and sub-units) is Granodiorite. Concordant with its leached nature, copper mineralization is scarce, corresponding mainly to traces of chrysocolla, atacamite and chalcopyrite (partially oxidized), that can be found together with variable amounts of pyrite. Alteration minerals are mainly amorphous iron oxides and hydroxides (limonite and hematite) occurring as infill of defects and veinlets, replacing primary copper sulphides (mostly chalcopyrite) or pyrite in the veinlets and in mineral grains. Gypsum, calcite and pyrolusite are also abundant and commonly present mixed with iron oxides and hydroxides as infill of defects. Locally, granodiorite's silicates have shown alteration to clay minerals, which is related to the leaching process. Even though there is a profuse alteration, abundant defects and partial replacement of silicates, the HELZ preserve its soundness (**Figure 3.8**), allowing the unit to be treated as a rock for the current analysis.



**Figure 3.8. Bench excavated in Heterogeneous Leached Zone (HELZ). Brown colors corresponds to abundant Iron Oxides and Hydroxides. Note the high degree of fracturation of this geotechnical unit.**

### **3.2.3.1 Healed defects in the Leached unit**

Defects in the context of the Leached rock refers to healed discontinuities, commonly filled with iron oxides - hydroxides, gypsum and calcite, with low tensile strength. Due to its abundance, these defects have a high impact on the rock block strength in the Leached rock; hence, they are considered the main factor controlling the strength upscaling of the intact rock.

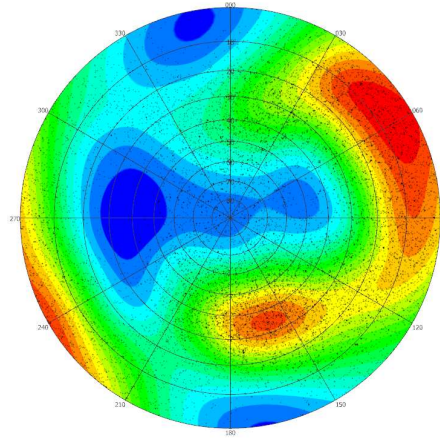
Defects intensity P10, obtained from drill core logging, varies from 1 to 25, with an average P10 of 8.9 #/m. Given the low tensile strength of defects with higher amount of iron hydroxides, this average P10 is probably a conservative intensity for defects, given that part of the discontinuities logged as joints can likely be defects that opened during drilling (**Figure 3.9**).





**Figure 3.9.** Photograph of drill core with defects. Infill of defects and joints coating correspond to the same mineralogy of iron oxides and gypsum. Orientation of defects and open joints is in various cases similar.

Based on drill core photographs (**Figure 3.9**), the orientation of open joints and defects in drill core seems concordant, therefore, ATV's orientation of discontinuities ranked 1 and 2 have been assumed valid for joints and defects. As pointed out previously, this information is biased due to the preferential orientation of drillholes. **Figure 3.10** shows the stereonet of those ATV structures.



**Figure 3.10. Stereonet of drillhole's ATV for discontinuities of rank 1 and 2 (number of poles =13722). This orientation was assumed the same for joints and healed defects in the Leached unit.**

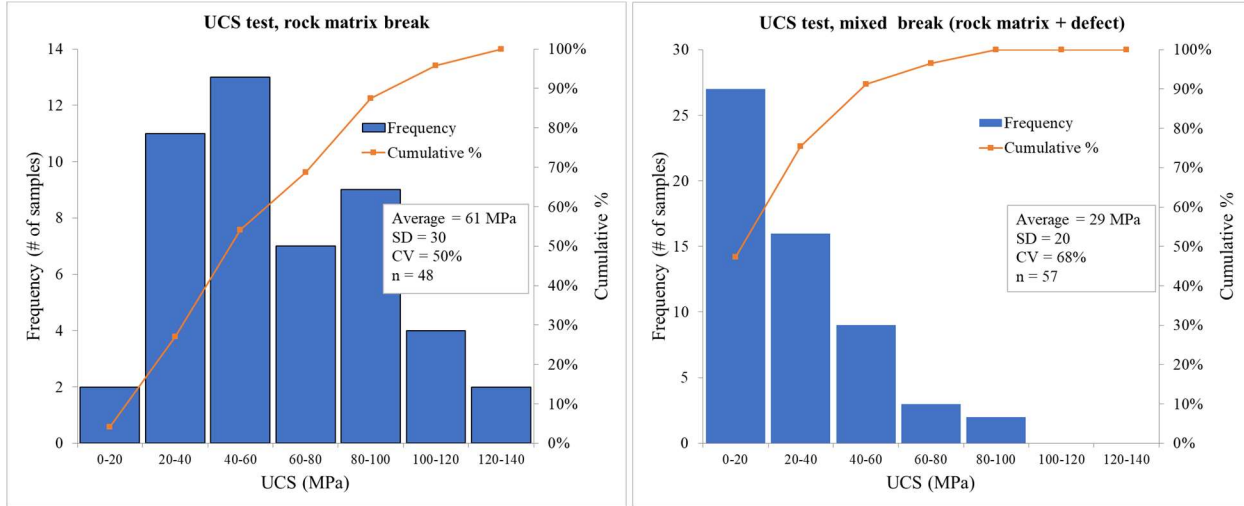
### **3.3 Laboratory strength test of leached geological unit**

Since the leached geological unit correspond to a highly defected rock, its mechanical behavior at failure is controlled by the combined strength of rock matrix and defect. Rock matrix is defined here as the geological material in which the visible defects are embedded. The rock matrix, in the manner the term is used in this work, can contain flaws or cracks that are not visible to the naked eye.

#### **3.3.1 Uniaxial compressive strength**

The importance of differentiating the type of rupture in laboratory samples to appropriately describe the strength of defected rocks has been highlighted by several authors (Marambio et al, 2000; Jakubec, 2013; Russo and Hormazabal, 2016, Bewick et al, 2018). Thus, laboratory test strength data of the leached unit was addressed based on the type of rupture of the samples. Three categories of rupture were used: rock matrix break, mixed break (rock matrix + defect) and defect break. These categories are a simplification of laboratory test rupture classification created by Marambio et al (2000) and are analogous to those defined by Bewick et al (2018). Most of the samples with a rock matrix break came from blocks extracted from blasted material in the leached unit. Cylindrical samples of diameters between 45 to 60 mm were drilled from these blocks. Given that the blasting process probably destroyed the weaker blocks, this value can be considered an approximation of the actual strength of the rock matrix in the defected rock. Mixed break samples

came exclusively from drillholes of 61 mm diameter located in the slope of the interramp failure. **Figure 3.11** shows Uniaxial Compressive Strength (UCS) for the leached unit laboratory test with rock matrix break and mixed break.

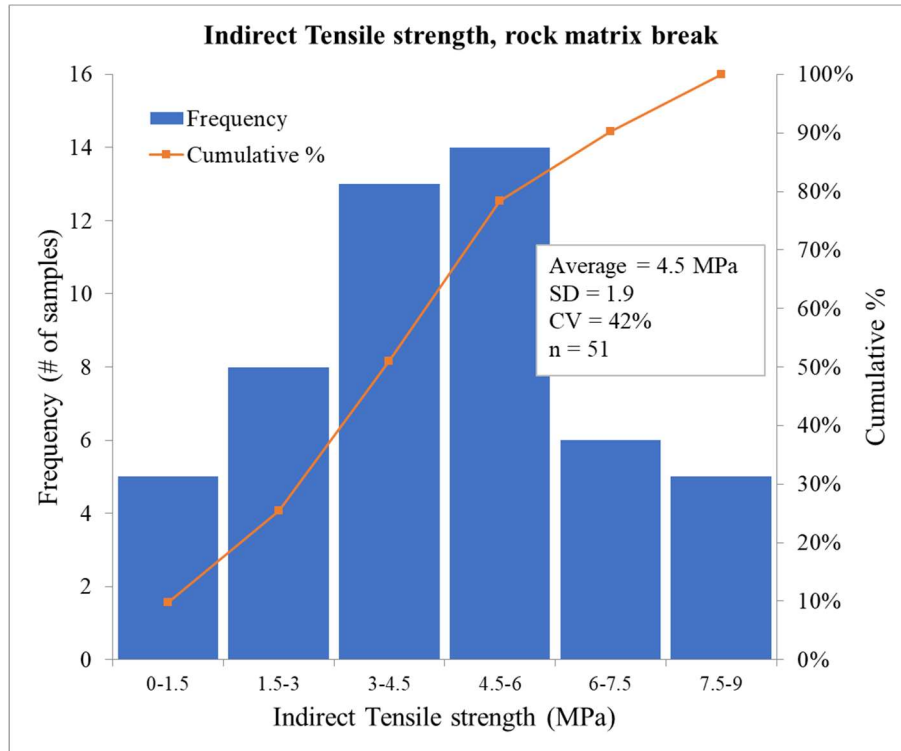


**Figure 3.11. Histograms of UCS laboratory test performed on samples from the leached geological unit. The diameter of samples with rock matrix brake (left) varied from 45 to 60 mm, diameter of samples with mixed rupture (right) was 61 mm. All strength data was converted to a 50 mm diameter sample using Hoek and Brown (1980) size-strength relationship. Basic statistics presented for each data set. SD: standard deviation, CV: coefficient of variation, n: total number of samples.**

The coefficient of variation for UCS data of both types of break, rock matrix and mixed, is quite high (**Figure 3.11**), which is related to the natural heterogeneity of the alteration and intensity of defects in the leached rock. Due to a lack of complete geological descriptions or insufficient test data, attempts to classify the strength in function of the degree of alteration and intensity of defects were infructuous. For use in the next chapters, the UCS of samples with mixed break was approximated at 30 MPa while the rock matrix average UCS was approximated at 60 MPa

### 3.3.2 Tensile strength, confined strength and intact rock failure envelope

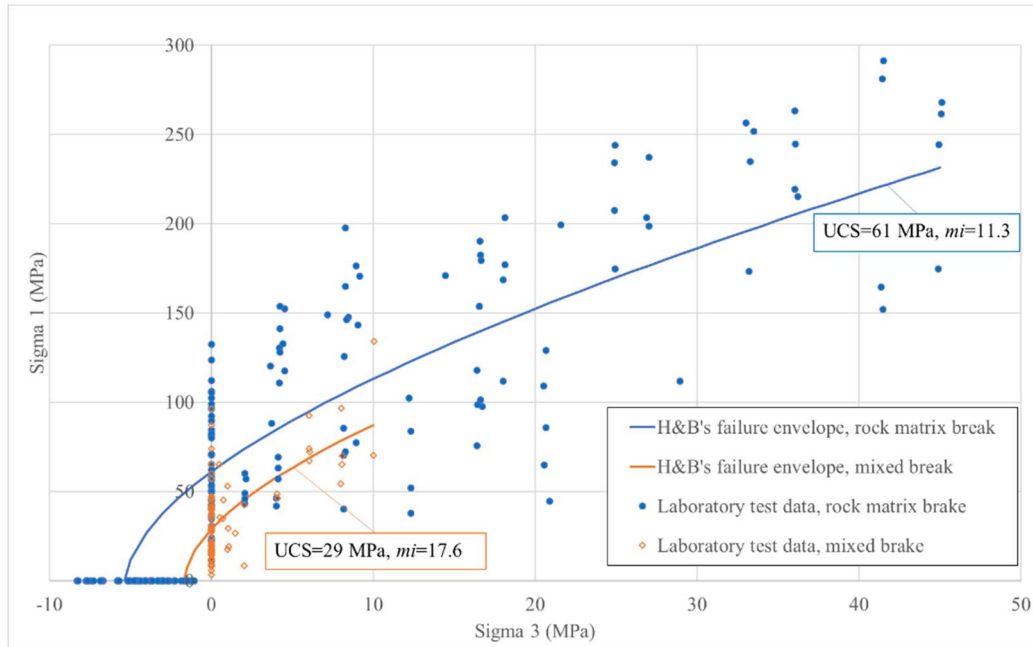
Indirect tensile strength test (Brazilian) data was available for samples with rock matrix break only. As in the case of the UCS test, the coefficient of variation is quite high (42%). **Figure 3.12** shows the histogram for tensile strength.



**Figure 3.12. Indirect tensile strength (Brazilian) test for the leached unit. Rock matrix break only. SD: standard deviation, CV: coefficient of variation, n: total number of samples.**

Analogously to UCS data, biaxial laboratory test was classified based on the type of break in the sample after loading. Failure envelopes, separately for rock matrix break and mixed break, were characterized by fitting H&B's failure criteria to Brazilian (available only for rock matrix brake), UCS and biaxial laboratory testing. The fitting process was performed in Rocdata (Rocscience, 2017) software. Those samples that broke throughout defect were used to estimate the defect's strength and were not included to estimate the material failure envelope. **Figure 3.13** shows H&B's curves fitted to the laboratory test separated by break type.





**Figure 3.13. Laboratory strength test and H&B's failure envelopes for rock matrix break and mixed break. Data points are 183 for rock matrix break and 80 for mixed break. Note that there is no tensile strength data for mixed break test. UCS and  $m_i$  factor that characterize each H&B's failure envelope are included in the figure. H&B's envelope fitting was carried out in Rocdata software.**

As asserted by Bewick et al (2015), interpretation of laboratory test data of defected rocks can be quite challenging due to its dispersion, which is related to the heterogeneity of the material. In the strength data presented here, even in the case of laboratory data with break through rock matrix, the coefficient of variation is around 50%, considered a high value (Read in Read and Stacey, 2009).

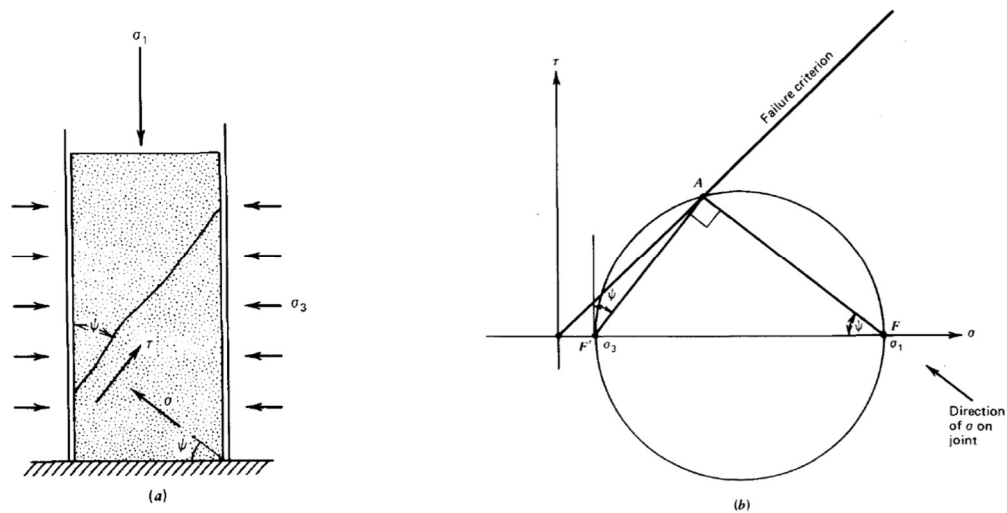
None of the failure envelopes in **Figure 3.13** can be considered as representative of the rock strength for the leached geological unit. Samples with break through rock matrix do not include the mechanical effect of the abundant defects. Samples with mixed break includes the effect of defects in strength, however, considering the sample size and upscaling effect, the failure envelope is valid only for the specific sample size that was tested. This is true not only for defected rocks but for any type of rock. As showed in Chapter 4, size – strength reduction cannot be generalized and is specific for the rock type.



Chapter 4 shows that strength can decrease significantly with size. Thus, rock block strength becomes a more meaningful parameter than the rock strength that is commonly tested at sizes way below the average rock block size. However, to obtain samples at the size of rock block is difficult and expensive, and its preparation is challenging. Synthetic rock mass (SRM) offers an alternative to estimate rock block strength. Strength data presented here, specifically rock matrix strength and defects strength, is part of the necessary inputs to assemble numerical SRM samples presented in Chapter 4.

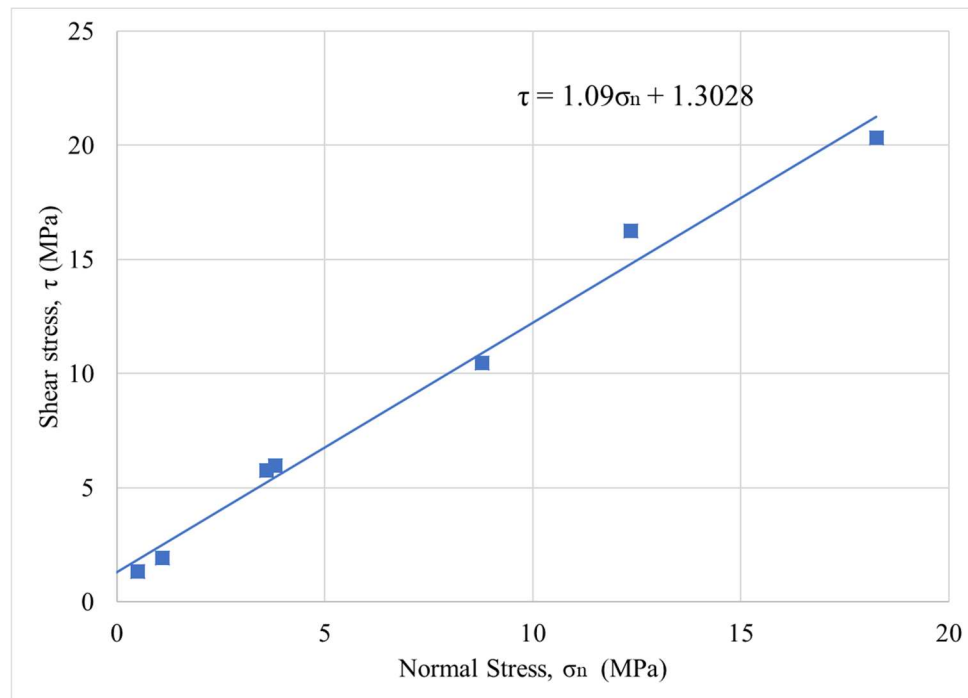
### 3.3.3 Strength of defects

Strength of defects was assessed applying the methodology proposed by Goodman (1989) on biaxial laboratory testing with break throughout a single defect (**Figure 3.14**). Thus, sigma 1 and sigma 3 from biaxial test were transformed to M-C space. The cohesion and friction angle calculated for seven samples that broke throughout a single defect was used. The linear regression of this data corresponds to the failure criterion for defects.



**Figure 3.14.** Biaxial test with break throughout a single defect (or joint) was used to characterize defect's strength;  $\psi$  is the angle between the defect and the axial load (a). Normal and shear stress in the defect are located at point A (b), which is formed by the intersection of a line from F, making an angle  $\psi$  with the horizontal axis, and Mohr circle. Alternatively, normal and shear stress can be obtained drawing a line from  $F'$ , making an angle  $\psi$  from the vertical, and piercing the Mohr circle at A (from Goodman, 1989)

Because the angle of breakage was not available, this information was obtained from ATV register or from drill core photography when available. Therefore, there is a degree of error on these measurements, given the potential differences between the ATV's depth record and the depth measured in the core or inaccuracies in the identification and angle of defects in photographs. Goodman's methodology should be applied when the discontinuity forms an angle between 25° to 40° with the axial loading, but due to the scarcity of data defects with angles of 10° with the axial load were included as well. **Figure 3.15** shows the cohesion and friction angle obtained for the single defect breakage biaxial test data. The linear regression curve yields the failure criterion for defects. Cohesion and friction angle from regression in **Figure 3.15** were used as input for defects strength in SRM simulation of the defected rock (Chapter 4).

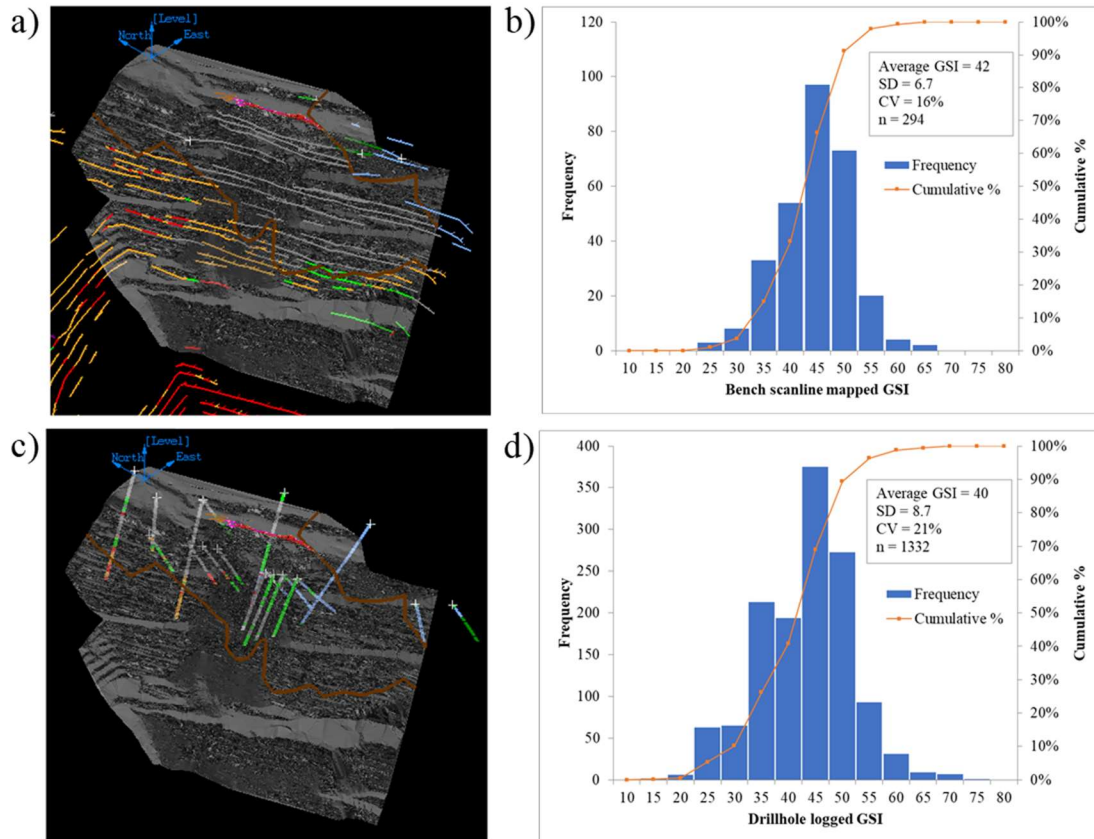


**Figure 3.15.** Biaxial laboratory test data with rupture trough single defect converted to normal stress ( $\sigma_n$ ) - shear stress ( $\tau$ ) space using Goodman's procedure. The linear regression of the data yields the failure criterion for defects, namely: Cohesion=1.3 MPa, Friction angle = 45°

### 3.4 Geological Strength Index (GSI) of the Leached geological unit

From the three parameters needed to fully characterize rock mass strength using H&B's failure criterion, namely intact rock  $m_i$ , intact rock UCS and Geological Strength Index (GSI), the third one describes the blockosity and quality of the discontinuities and scales up to rock mass the intact rock strength. The objective of the rock mass characterization presented here is to obtain GSI parameter for the leached unit. This parameter will be used in Chapter 5 to calculate rock mass strength and perform back analysis of the inter ramp failure that occurred in the leached unit.

Two data sources were used to characterize the GSI of the Leached unit: bench mapping scanlines and drill core logging. In both cases the estimation of GSI was made visually using GSI's chart. While GSI's chart can be applied directly to the rock exposed in the bench face, visual estimation from drill core requires validation. Guest and Read (in Read and Stacey, 2009) asserts that GSI from drillhole must be calculated indirectly from Bieniawski's RMR by  $RMR_{89}-5=GSI$ , formula proposed by Hoek and Brown (1997). From drill core logging, the mean  $RMR_{89}$  is equal to 47, while the chart estimated mean GSI is 40. Thus, applying the formula, both GSIs values, RMR based equal of 42 and chart estimated equal to 40, are quite near, validating the GSI estimation from drill core. **Figure 3.16** shows the GSI histogram from the bench mapping scanline and from the drill core. The support of the data, logged in the leached unit, is 2080 m of drill core and 16645 m of bench scanline mapping. The latter was collected in different pushbacks excavated in a period of 14 years in the leached unit.

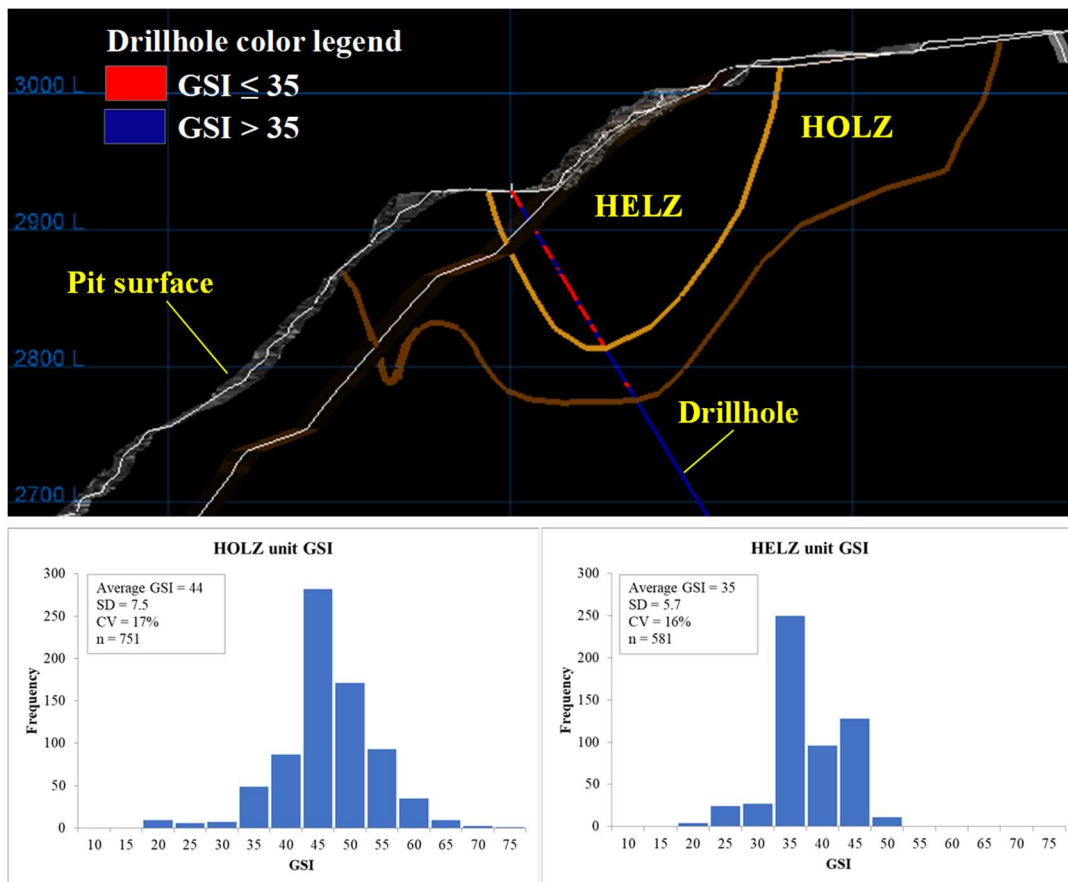


**Figure 3.16. GSI mapped in leached rock on the north east slope. Figures a and c show the north east slope (in gray) with bench scanline mapping and drillholes respectively. Average GSI from bench mapping is equal to 42 (b), while drillhole GSI is equal to 40. More detailed characterization can be performed in drill core logging, hence the higher dispersion for that support. Further analysis of the apparent bimodal distribution in (d), lead to a subdivision of the leached rock based on GSI.**

The leached rock mass can be described as a well-connected fracture network. Fracture frequency of joints range (P10) is 2 - 20 with an average of 8.8 #/m while RQD varies from 15% to 90% with an average equal to 60%. In general, geotechnical parameters describing the leached rock mass show a high dispersion.

A possible bimodal distribution for GSI data from drill core (**Figure 3.16**), in addition to high dispersion of rock mass geotechnical parameters suggested the possibility of separation of the leached rock in subunits. Thus, drill core data was explored with the aim of splitting the leached rock in subunits of contrasting GSI. It was found that when a GSI threshold equal of 35 is applied to drillhole data, the leached geological unit can be subdivided in two differentiable subunits, with

average GSI of 35 and 44 each one, and a lower coefficient of variation regarding calculations for drill core data all together. In this manner, the subunits Heterogeneous Leached Zone (HELZ) and Homogeneous Leached Zone (HOLZ), with an average GSI of 35 and 44 respectively, were defined. The names of these subunits are related to the pattern of GSI when the 35 threshold is applied to drill cores, visualized as a spotted pattern in the HELZ and flat pattern in HOLZ unit. **Figure 3.17** shows the descriptive statistics for the subunits and a geological cross section with drillhole information included.



**Figure 3.17.** GSI logged on drill core showed a spatially consistent spotted distribution of GSI less than 35. This spatially traceable pattern allowed the mapping of two separated geotechnical units in the leached rock, namely HELZ and HOLZ (upper cross section). Statistics on drill core logging showed a reduced dispersion of GSI values when the leached unit is separated in HELZ and HOLZ (lower histograms), which confirms the suitability of the differentiation. Coefficient of variation for the leached unit without differentiation is 21%, which compares to 17% for HOLZ and 16% for HELZ.

Laboratory testing of the Leached rock was explored considering their spatial location. It was not possible to conclusively define a differentiated strength for HELZ and HOLZ unit. The lower quality HELZ unit contained only 8 of the tested samples. Given that the strategy of laboratory test sample extraction was to take all the pieces of rock that can be prepared to be tested, it is clear that HELZ encloses the weaker rock inside the leached unit. Strength from laboratory test cannot be differentiated per subunit due to insufficient data.

### **3.5 Conclusion**

The supergene alteration produced leaching of the primary sulphides, weakening the rock and depositing the products of alteration in the rock's defects. The weak but sound leached rock contains abundant healed defects which govern the rock block strength. The defects infill is composed mainly by the secondary minerals, product of the supergene alteration.

Rock strength was characterized using laboratory test; the data was classified, based on the type of rupture of the samples, in defect break, break through rock matrix and mixed brake. H&B's failure envelopes are presented for rock matrix break and for samples with mixed break (rock matrix + defect). Due to the abundant defects and strength upscaling effect, neither is considered representative of the strength of the block in the leached rock, but they are input parameters for the numerical experiments presented in Chapter 4. The methodology proposed by Goodman (1989) was applied on biaxial laboratory test with single defect brake to characterize defects strength.

The leached rock mass was characterized using H&B's GSI. The bi-modal distribution of this parameter in the leached geological unit was addressed by dividing it into two geotechnical units: Heterogeneous Leached Zone (HELZ) and Homogeneous Leached Zone (HOLZ). The validity of this differentiation was confirmed by the reduced variance of the GSI for each geotechnical unit.

Bench scanline mapping, drill core logging and acoustic televiewer (ATV) of drillholes are the sources of information.

## **Chapter 4. Numerical investigation on rock strength upscaling using synthetic rock approach**

### **4.1 Introduction**

With the aim of characterize/explore the strength upscaling of the defected rock introduced in Chapter 3, bidimensional (2D) Synthetic Rock (SR) samples were assembled and tested using the ELFEN hybrid numerical code. A combination of previously presented physical properties for defects plus calibrated properties for rock matrix, together with Discrete Fracture Network (DFN) of defects, created in Fracman software (Golder, 2017), are the inputs for SR samples. Uniaxial, biaxial and indirect traction Brazilian type tests were performed on synthetic samples, the results of these tests were used to characterize the strength upscaling of the defected rock adjusting a mathematical relationship based on Yoshinaka et al (2008) relationship, which in turn is based in Weibull's statistical theory. Compressive numerical SR experiments combining defects and purely frictional fractures (joints) are presented at the end of the chapter as a means of exploring the global strength of a rock mass with a defected rock matrix, for which upscaling of rock bridges strength is verified.

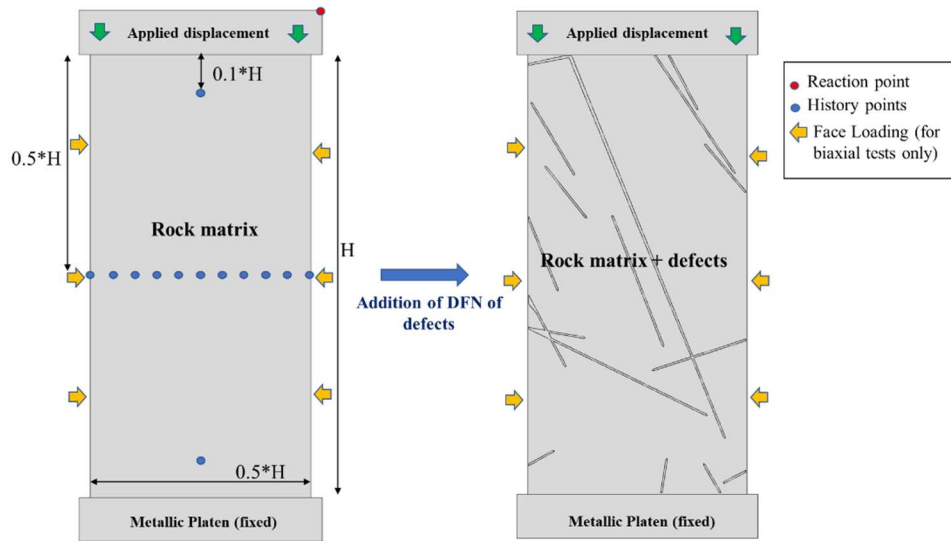
### **4.2 Synthetic Rock (SR) test model setup**

The geometry for uniaxial and biaxial 2D tests was constituted of two rectangular platens located in the upper and lower ends of the rock sample. Physical properties are assigned in accordance to the material, with elastic type material for metallic platens and plastic properties for the rock. This sample geometry was scaled to the size of the test to perform. Discrete Fracture Network (DFN) of defects was then added to this geometry to finally assemble the SR model to be tested. For compressive tests height/width ratio was set equal to 2. Thus, six different sample sizes were assembled (all sizes in millimeters): 50x100, 125x250, 250x500, 500x1000, 750x1500 and 1000x2000.

With respect to applied loads, the lower platen offer support for the whole system and remains static during the test, while the load is applied assigning a vertical displacement to the upper platen. Horizontal movement on platens is totally restrained during the test. In ELFEN the vertical

displacement is defined by a time-load curve, allowing the use of an increasing, nonlinear load application throughout the displacement of the platen if required. SR trial models were run to assess sensitivity of the test to the applied load. No important variation was found when variable or constant displacements (0.5 mm/s, 1mm/s and 2mm/s) were applied. Therefore, constant linear displacement of 2 mm/s was used for most of the SRM test. For biaxial test, constant confinement was applied by assigning a face loading equal to desired confinement on both sides of the rock sample. No material was simulated to apply the confinement for biaxial test.

To register stress and strain during the test, 11 history points were located in the center of the rock sample, plus 2 history points near the upper and lower end of the sample. Reaction was measured in the platen using the coupled freedom facility in ELFEN, where the upper platen is constrained to follow the displacement of one single point (acting as master entity), then, reaction, displacement and velocity are recorded for this point. Given the good agreement found between the average stress-strain curve of the 11 central history points and the reaction point located in the platen, this configuration is up to certain extent redundant. However, history points are needed to record strain in the x-axis. **Figure 4.1** shows the test setup.



**Figure 4.1. SR sample setup. Basic setup geometry to the left. Final SRM with DFN of defects added for a 250x500 mm sample size to the right side of the figure (H: sample height).**



With the aim of facilitate the assemblage of SR models, defects geometry was trimmed at 2 – 5 mm from the sample border (depending on sample size). This procedure allows direct importing of defects geometry into ELFEN and does not require further editing of geometry inside the software to eliminate overlapping lines.

#### **4.3 Discrete Fracture Network of Defects**

As stated previously, SR models are composed of a combination of rock matrix and a Discrete Fracture Network of discontinuities, described as defects in the current case. A tridimensional (3D) Discrete Fracture Network (DFN) was built using Fracman Software (Golder, 2017), based on the characterization of defects presented in Chapter 3. For DFN building, intensity (P10) and orientation components were sourced from core logging and Acoustic Televiewer geophysical survey respectively. No actual measurements of defects size were available; thus, size distribution was largely based on qualitative observations made by the author. A lognormal distribution, with mean equivalent radius of 15 cms was assumed, standard deviation was set as 50% of mean equivalent radius and a minimum size cut off of 5 cms was used to generate defects DFN. As is the case for real rocks, discontinuities size has a high impact in the strength of numerical samples (Elmo et al. 2014), therefore size distribution assumption is the main source of uncertainty for the numerical experiment, with direct influence in the Representative Elementary Volume of the simulated rock.

Observation in core samples allows to assume the orientation of defects to be similar to orientation of fracturing, therefore this information is used to bootstrap defects orientation in Fracman software. ATV structures were first filtered, using the available categorization of structures into ranks, from rank 1, corresponding to discontinuous and sealed structures, to rank 4, open and continuous structures with thick infill in the hole wall (likely faults). Thus, discontinuities ranked 1 and 2 were used to bootstrap defects DFN.

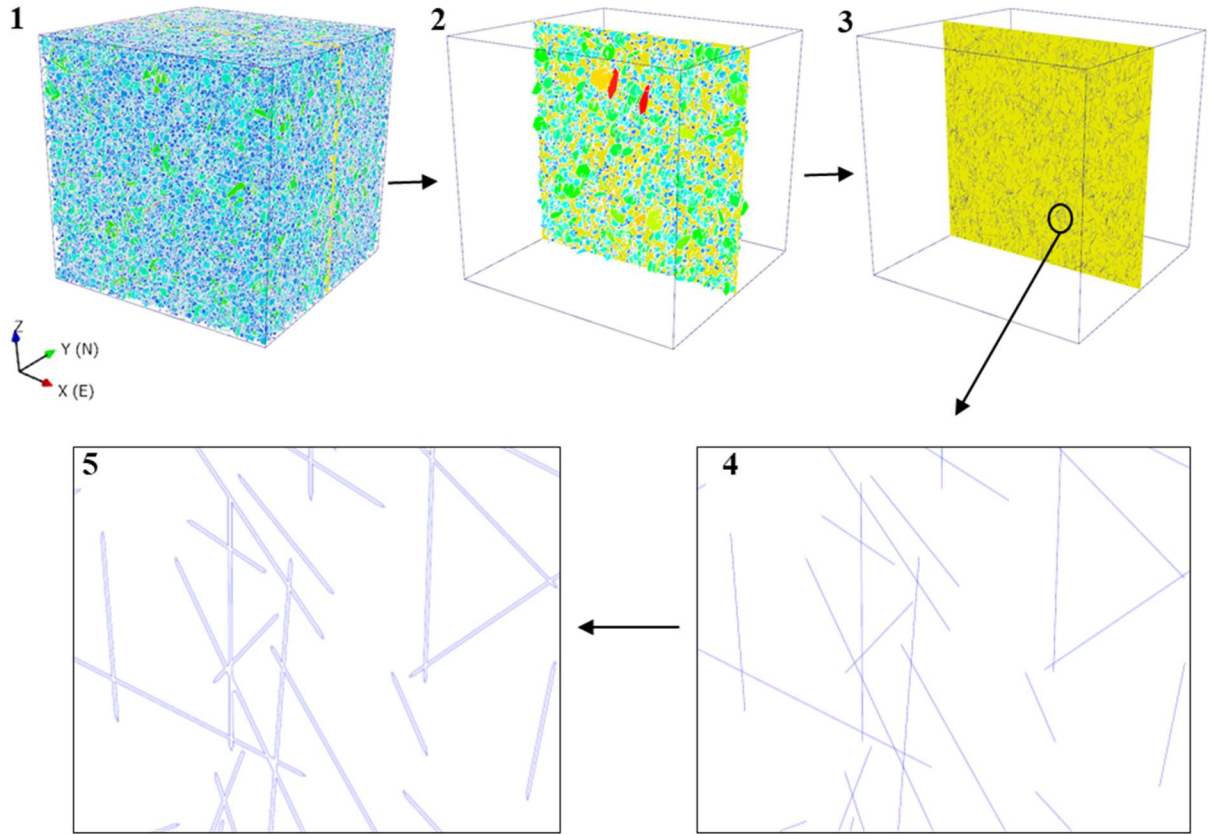
Volumetric intensity P32 (surface of fractures contained in volume of rock) was obtained applying simulation process described by Elmo (2006), yielding the relationship  $P32=2.1*P10+0.17$ ; given a mean P10 intensity of defects equal to  $8.9 \text{ m}^{-1}$  (from core logging CHDD10027) a P32 of  $18.89 \text{ m}^{-1}$  was obtained for defects DFN. Table 1 shows the input parameters for DFN of defects.

**Table 4.1. Input parameters for defects DFN**

Parameter	Source of information	Method	Values
Orientation	ATV	Bootstrap	--
Intensity P32	Core logging	Simulation	P32=18.89 (m <sup>2</sup> /m <sup>3</sup> )
Discontinuity equivalent radius	Qualitative observations	--	Lognormal, Mean=7.5 cms, SD 3.5

Input parameters presented in Table 4.1 were used to create a single 3D DFN realization of defects, then a vertical cross section of 5x5 meters was extracted from the realization. Discontinuities subparallel to the cross section were removed applying a filter of  $\pm 20^\circ$  regarding the section strike. This single realization was the source of all the defects used to assemble SR samples of the defected rock presented here.

Defects traces (single lines) obtained from the vertical cross section were initially used to assemble SR samples, with strength properties (friction and cohesion) obtained from triaxial test that failed through defects as described in Chapter 3. Tensile strength was assigned based on infill mineralogy. The use of single lines as a representation of defects was not possible in ELFEN software. Models run in version 4.4 crashed when tensile strength was assigned to the defect traces (the lines). ELFEN version 4.7, although is able to handle discontinuities with tensile strength, it can only use a single set of fracture properties, meaning that new fractures would have tensile strength, as is used in pre-existing fractures, which is physically incorrect. In addition, the possibility to use cohesion for pre-existing fractures and friction only (cohesion =0) in the new generated fractures is not part of the functionalities of ELFEN 4.7. This limitation was overcome using defects with actual width (2D polygons) instead of the unidimensional traces as proxy. Thus, the lines became polygons, resembling the material in the defects, which were assigned defects properties. **Figure 4.2** shows the process to obtain the defect geometry finally used in the SR models.



**Figure 4.2. Defects generation for SRM modelling. 1 Defects DFN realization (input parameters from Table 1). 2 Vertical cross section (5x5 m) showing intercepted 3D defects. 3&4 shows defect traces as obtained from the cross section. 5 Defects were drawn using linear traces as guide, defect's material properties are then assigned to these polygons in the SRM model (width of each defect is 2mm).**

The modelling of defects as elements featuring a width affects SRM modelling in two ways the: 1) Introducing a limit for mesh size in the defects, 2) the mandatory use of plastic properties (Mohr-Coulomb + elastic properties) instead of the simpler contact properties for defects (Mohr-Coulomb) when using single lines.

#### **4.4 Synthetic Rock properties**

##### **4.4.1 Material properties**

The SR was modelled in ELFEN using a Mohr-Coulomb with Rankine tensile cut-off type material model, detailed explanation of this model is presented by Klerck (2000) and Elmo (2006).

Mandatory parameters for material definition in ELFEN for the mentioned model are: Young's modulus, Poisson ratio, Density, Cohesion, friction angle, dilatancy angle, tensile strength and Fracture Energy (Elmo, 2006).

In ELFEN FDEM hybrid code, the initiation and extension of cracks is controlled by Fracture Energy (Gf), calculated by the following expression (Klerck, 2000):

$$Gf = \frac{K_{IC}^2}{E} \quad (4.1)$$

Where  $K_{IC}$  is the fracture toughness and E is the Young's modulus. The following relationship proposed by Zhang (2002) was used to calculate fracture toughness:

$$K_{IC} = \frac{\sigma_t}{6.88} \quad (4.2)$$

In the SR assemblage, veins properties are a combination of test data and estimation of elastic parameters based on the author's observation. Rock matrix cohesion and friction were calibrated to match average UCS of mixed rupture test (failure trough rock matrix + defect).

Platens (**Figure 4.1**) were modelled as stiff elastic entities, with material properties equal to steel (Young's Modulus = 200 GPa, Poisson ratio = 0.3 and density = 7.85 ton/m<sup>3</sup>).

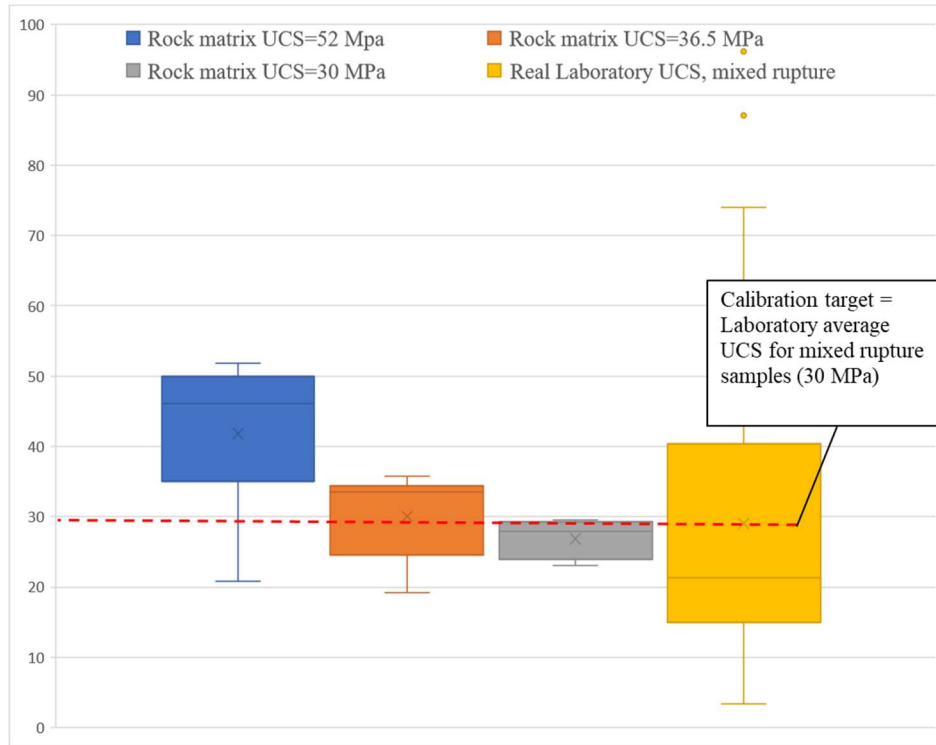
#### 4.4.2 Veins properties

As previously mentioned, due to software limitations, DFN unidimensional traces of defects were transformed into discontinuities with actual width, introducing the need for using elastic properties, Poisson ratio and Young's modulus, in addition to Mohr-Coulomb properties, which were available from triaxial test described in Chapter 3. Elastic properties were then assigned based in the mineralogy of defects and the author's criteria, namely, a Young's modulus of 30 GPa and Poisson ratio equal to 0.26, both values closer to gypsum (Yilmaz and Sendir, 2002) than to iron hydroxide. There is no data available for tensile strength of defects, therefore, a value of 1 MPa was estimated based on tensile strength of incipient filled veins reported by Shang et al (2016).

#### 4.4.3 Rock matrix (Leached Granodiorite) properties

Considering the multiscale nature of the discontinuities in the rock, it can be expected that visible and well-defined defects occur together with less visible flaws at a scale of millimeters. In this manner, for two rock samples coming from the same geological unit, one with defects and the second with no visible defects, the strength of the rock matrix, ie the inter defect portion of the sample, will be lower in the former due to the presence of flaws at a scale of millimeters. Thus, strength from laboratory test that failed through rock matrix must be calibrated to be applied in SR with defects, to account implicitly for micro flaws. Following this principle, the calibration of the defected SR was made adjusting the rock matrix strength while veins strength was kept constant.

As described in Chapter 3, the strength of the leached Granodiorite with no defects can be characterized with a HB failure envelope of UCS 60 MPa and H&B's  $m_i$  coefficient equal to 11.3. MC's parameters were obtained by the linearization of the H&B's failure envelope in Rocdata software (Rocscience, 2017); friction angle of  $48^\circ$  and cohesion of 10.8 MPa. For the rock without defects, Young modulus (21.9 GPa), Poisson ratio (0.27) and tensile strength (4.5 MPa) were available from laboratory test as well. These properties, together with defects properties and corresponding DFN, were used to assemble 15 numerical samples submitted to uniaxial compression. In addition, rock matrix UCS of 52 MPa, 36.5 MPa and 30 MPa were tested in an iterative process. Similarly, MC cohesion and friction angle were obtained for these rock matrix strength values linearizing HB's envelope in Rocdata software, keeping  $m_i$  equal to the laboratory value (11.3). The aim of this calibration is not to reproduce the real distribution of UCS data for the defected leached granodiorite, but to match the average laboratory UCS to the sample size of 50x100 mm. Aiming to reproduce the actual variability of the rock strength would be an unrealistic goal, requiring much more detailed data and long analysis, making the experiment unpractical. **Figure 4.3** shows the comparison of UCS yielded during the calibration process and UCS test on real defected rock. Input cohesion of 7.6 MPa and friction of  $47^\circ$ , corresponding to 36.5 rock matrix UCS, show a good average match with real test data and was used for the SR experiments.



**Figure 4.3. SR calibration on 100x50 mm samples. MC’s cohesion and friction angle were obtained linearizing H&B’s envelope for a  $\mu$  of 11.3 (from real laboratory test) and the UCS indicated in the figure for each box. Rock matrix UCS of 36.5 MPa yield SR strength matching actual laboratory test.**

Table 4.2 shows the final properties for veins and rock matrix used in the SR experiments. Uncalibrated properties for rock matrix are presented too.

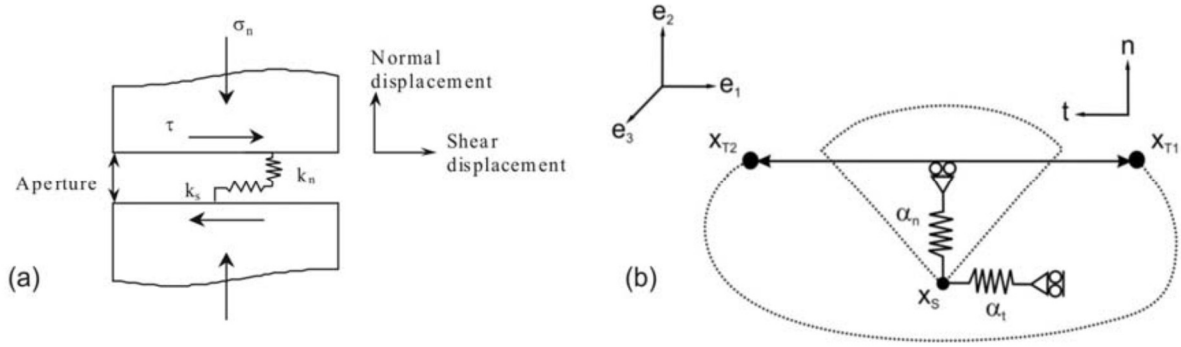
**Table 4.2. Final properties used for SR modelling highlighted in grey.**

Parameter	Rock matrix uncalibrated (Leached Granodiorite)	Rock matrix calibrated (Leached Granodiorite)	Defects
UCS (MPa)*	60	36.5	--
mi (Hoek & Brown)*	11.2	11.2	--
Tensile Strength, Ts (MPa)	4.5	4.5	1
Cohesion, Co (MPa)	10.8	7.6	1.3
Friction, $\phi$ (degrees)	48	47	45
Fracture Energy, Gf (J/m <sup>2</sup> )	19.5	19.5	2.1
Young's modulus, E (GPa)	21.9	21.9	30
Poisson ratio, $\nu$	0.27	0.27	0.26
Density (Ton/m <sup>3</sup> )	2.5	2.5	2.4

\* Parameters used for linearization of Hoek and Brown failure criterion to obtain friction angle and cohesion

#### 4.4.4 Contact Properties

Contact properties refers to those properties applied in ELFEN to any surface or discontinuity along which a material is in contact with itself or other. In the context of this work this includes the contact platen-sample, preexisting fractures (faults and joints) and new cracks product of loading during the development of the numerical simulation. For the SR tests presented here, Mohr-Coulomb (MC) relationship was used for contact interaction. Additionally, ELFEN uses a scheme of normal and tangential penalty (Pn and Pt respectively), for contact detection and to avoid elements penetration (Klerck 2000, Elmo, 2006). Elmo (2006) explores the correlation between numerical contact penalty coefficients and joint stiffness, showing that Pn can be considered effectively as equivalent to joint normal stiffness. **Figure 4.4** shows a scheme comparing the concept of joint stiffness and penalties coefficient in Elfen.

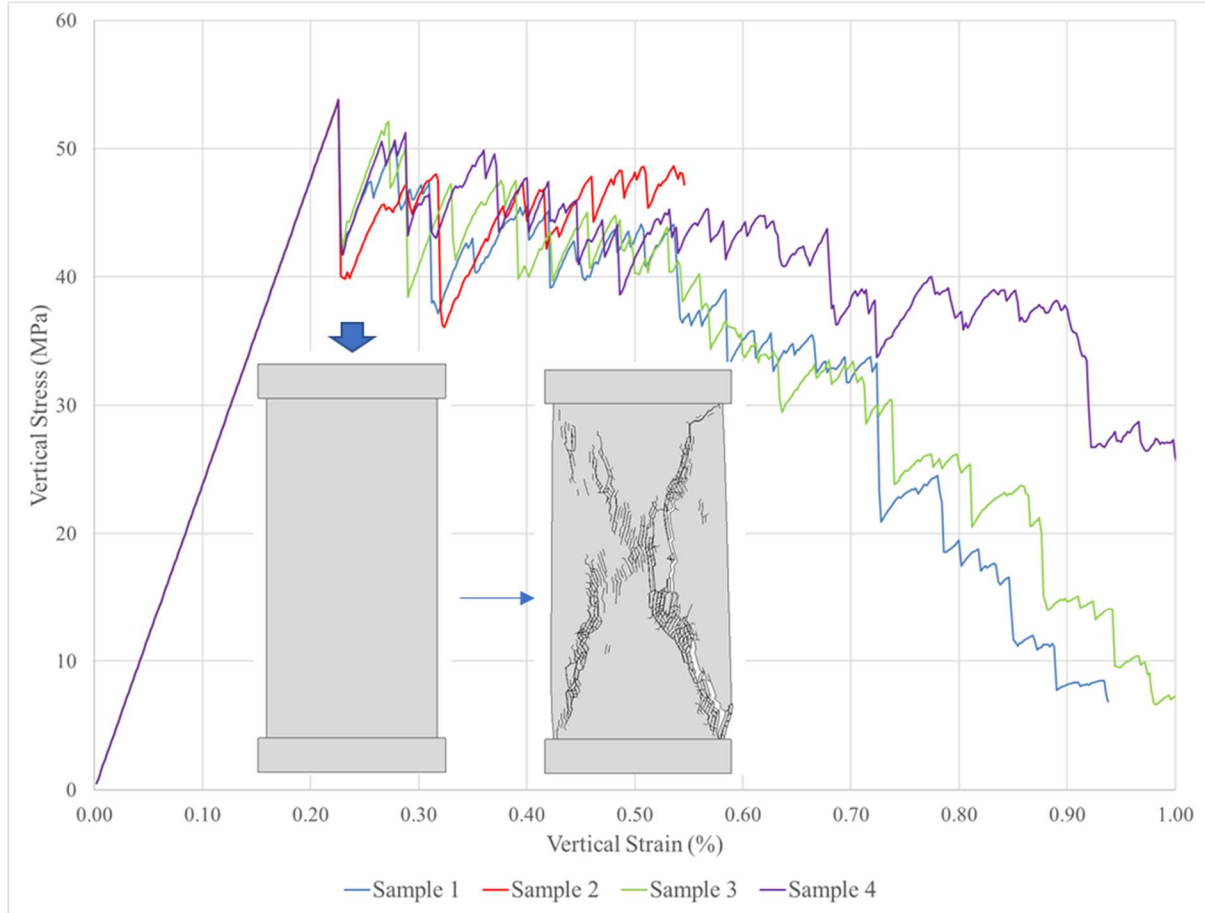


**Figure 4.4. (a) Schematic representation of a block containing a single discontinuity (after Bandis, 1993) (b) Penalty contacting couple in ELFEN as an equivalent spring system (after Klerck, 2000).  $k_n$ : normal joint stiffness,  $k_s$ : tangential joint stiffness (Elmo, 2006)**

$P_n$  is usually set in the range of  $0.5E < P_n < 2E$  (where  $E$  is the Young's modulus) with  $P_t$  equal to 0.1 of the normal penalty (Rockfield, 2005?). Sensitivity analysis performed by Elmo (2006) on  $P_n$  in combination with contact damping for pillar numerical simulations showed a more realistic mechanical behavior when a low  $P_n$  value is applied ( $P_n < 2\text{GPa}$ ). No Contact damping was used in the SR models described here.

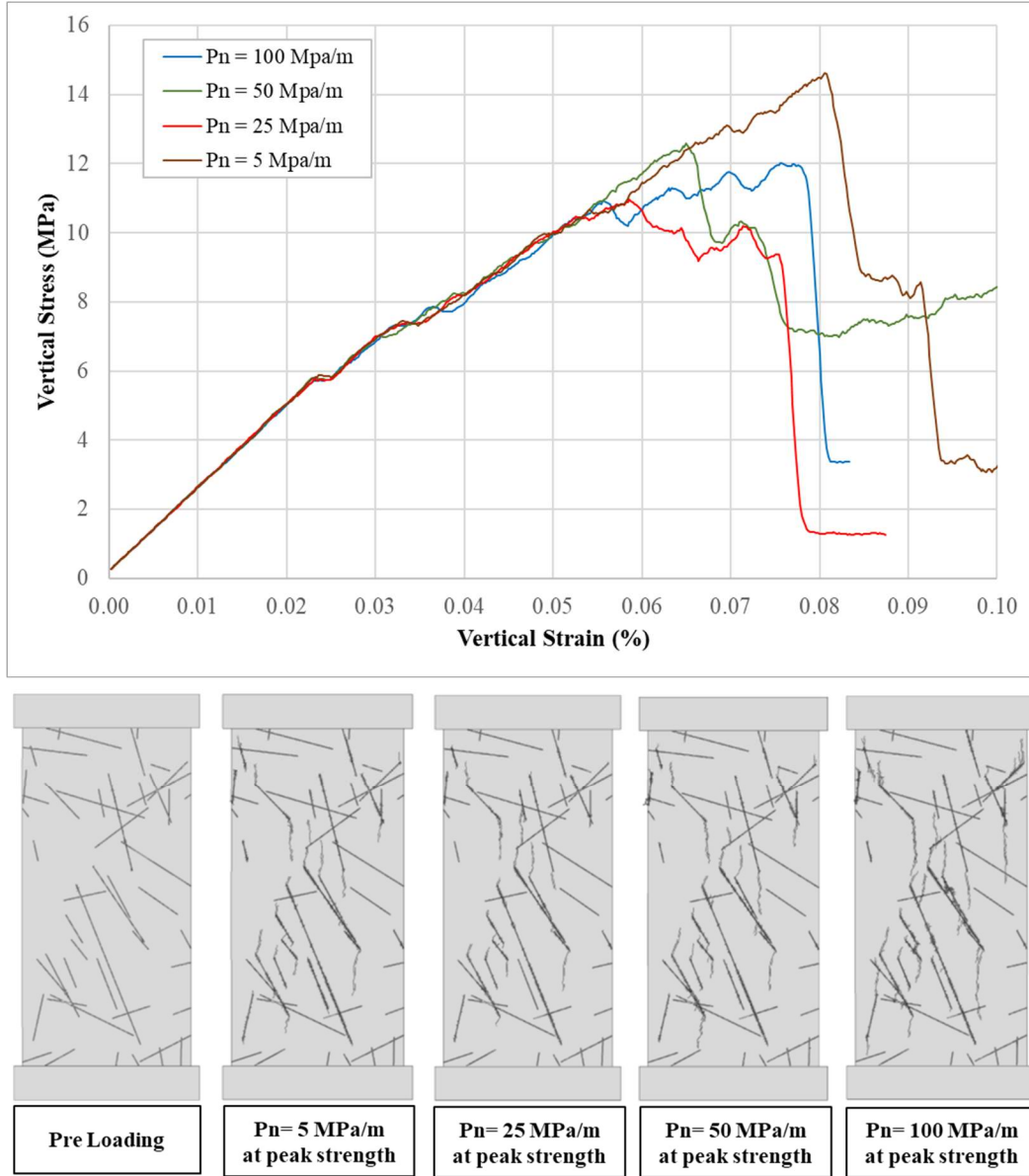
The effect of penalties after peak strength was shortly investigated. Trial uniaxial compression tests in a sample with no defects (sample strength properties of uncalibrated Leached Granodiorite in Table 2) were performed to evaluate the impact of different values of  $P_n$  and  $P_t$  for new formed cracks.  $P_n$  values of 100 GPa, 25 GPa and 5 GPa, with  $P_t = 0.1P_n$ , were used, friction was kept constant and equal to  $35^\circ$  and only one sample included a non-null cohesion of 1 MPa. In ELFEN, in samples with no joints, new cracks appear at peak strength, therefore no difference was expected nor found in the pre-peak and at peak strength behavior among the different penalty values tested. Post peak showed noisy but quite similar trends in the stress-strain curve, with little difference for the one sample where cohesion was used (sample 4, purple line in **Figure 4.5**). Similarly, cracking pattern in these trials is in general terms the same and shows the expected geometry for uniaxial compression test.





**Figure 4.5.** Stress – Strain curves for different values of default penalties (Sample 1:  $P_n=5$  GPa, Sample 2:  $P_n=25$  GPa, Sample 3:  $P_n=100$  GPa;  $P_t=0.1P_n$  for all samples). Sample 4 (purple line) shows different post peak trend due to the use of cohesion in the default contact property ( $C_o=1$  MPa). In grey the uniaxial test geometry, before loading (left) and showing the typical post peak cracking pattern (right). Numerical test performed using uncalibrated rock matrix properties.

The effect of penalties on SR defected sample was quickly investigated using a single 500x1000 mm sample under uniaxial compression. Four different values of penalties were applied (5, 25, 50 and 100 MPa/m), with  $P_t=0.1 \cdot P_n$ . Peak UCS varied between 10.9 to 14.6 MPa (**Figure 4.6**), with no clear relationship between peak strength and the penalty value used. Fracturing at peak strength does not show significative differences, although it seems slightly more developed for  $P_n=100$  MPa.



**Figure 4.6. Stress-strain curves for 4 different penalty variations ( $P_t=0.1 \cdot P_n$ ) in a 500x1000 mm SR UCS test. Figures at the bottom show the sample before loading and fracturing pattern at peak strength.**

Although penalties are only related to fractures (pre-existent and new) and the defected SR does not contain initially any crack, penalty has an influence on peak strength. This is explained by the new cracks, which onset occurred around 30% - 40% of peak strength, thus the penalties associated to these new cracks are influencing the peak strength. There is no clear trend of strength related to penalty, but the variation of peak strength (around 3.5 MPa) was considered not relevant. Thus, penalty values were set as  $P_n = 5$  GPa and  $P_t = 0.5$  GPa for cracks. With the aim of avoid any

penetration, a higher value of penalties was used for platen – rock interface;  $P_n=25$  GPa,  $P_t=2.5$  GPa. Although this penalty coefficient was maintained for most of the experiments, later a  $P_n$  of 5 GPa and  $P_t$  of 0.5 GPa were found equally suitable to avoid penetration with no much influence in global strength.

Friction angle for cracks was assigned equal  $35^\circ$ , value that can be considered as reasonable but not based in actual measurements. A friction coefficient of 0.2 was assigned to the platen – rock interface to replicate friction in real test. The difference in the elastic properties between steel platens and the rock generates friction when the sample is loaded, leading to stress concentrations with effect in the obtained strength (Feng, 2017). Thus, a low value of friction is desirable for this interface.

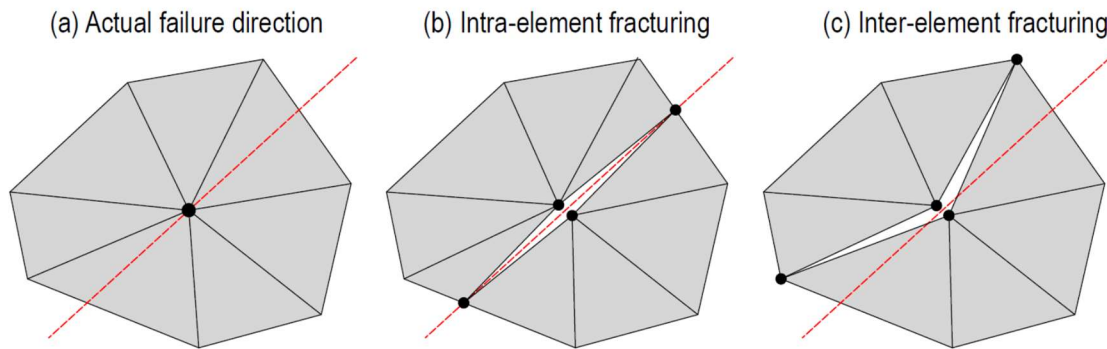
Default contact properties are mandatory in ELFEN and are applied to new formed cracks. Depending on the software version, individual contact properties can be defined for each set of joints (versions 4.0 and 4.2) or only a single set of default properties is allowed for all joint sets (version 4.7). **Table 4.3** shows the contact properties used for SR test.

**Table 4.3. Contact Properties used for SRM modelling**

Parameter	Default contact properties (new cracks)	Platen – Rock contact
Friction Coefficient (friction angle $\phi$ )	0.7 ( $\phi=35^\circ$ )	0.2 ( $\phi=10^\circ$ )
Cohesion (MPa)	0	0
Tension Cut-off (MPa)	0	0
Normal penalty (MPa)	5000	25000
Tangential penalty (MPa)	500	2500

## 4.5 Mesh, critical time step and computation time

As in finite and distinct element approach, materials modelled in ELFEN must be discretized by means of a mesh, for which the equations of movement and contact forces are solved for each single element at each increment of time (time step). For discrete analysis (allow fracturing), the tensile fractures in ELFEN can occur along elements contacts or through them (intra-element), realizing the fracture by splitting preexisting elements (**Figure 4.7**).



**Figure 4.7. ELFEN crack insertion procedure showing: a) the actual failure direction defined by weighted average configuration, b) intra-element fracturing, c) inter-element fracturing. (Klerck et al., 2004)**

### 4.5.1 Mesh quality

To ensure numerical stability and reliable results, mesh elements must accomplish a minimum geometrical quality (mesh quality). The aim is to avoid long and acute elements which are precursors of numerical instability. In general, mesh quality in SR models is mainly related to DFN complexity (DDN in the present work). In consideration of this, mesh quality can be achieved/improved by manual “cleaning” of the DFN realization, by using automated routines to properly integrate DFN and SRM, as is proposed by Karimi et al (2019), or integrating geomechanical meshing routines with DFN generation algorithms, as in Mayer and Stead (2017).

To assess mesh quality ( $Q_m$ ), ELFEN generates a “Mesh report”. For the triangular mesh used here, ELFEN calculates  $Q_m$  as follow:

$$Qm = \sqrt[2]{\frac{3}{2}} \times \frac{3 \times Hmin}{\sum_{i=1}^3 Li} \quad (4.3)$$

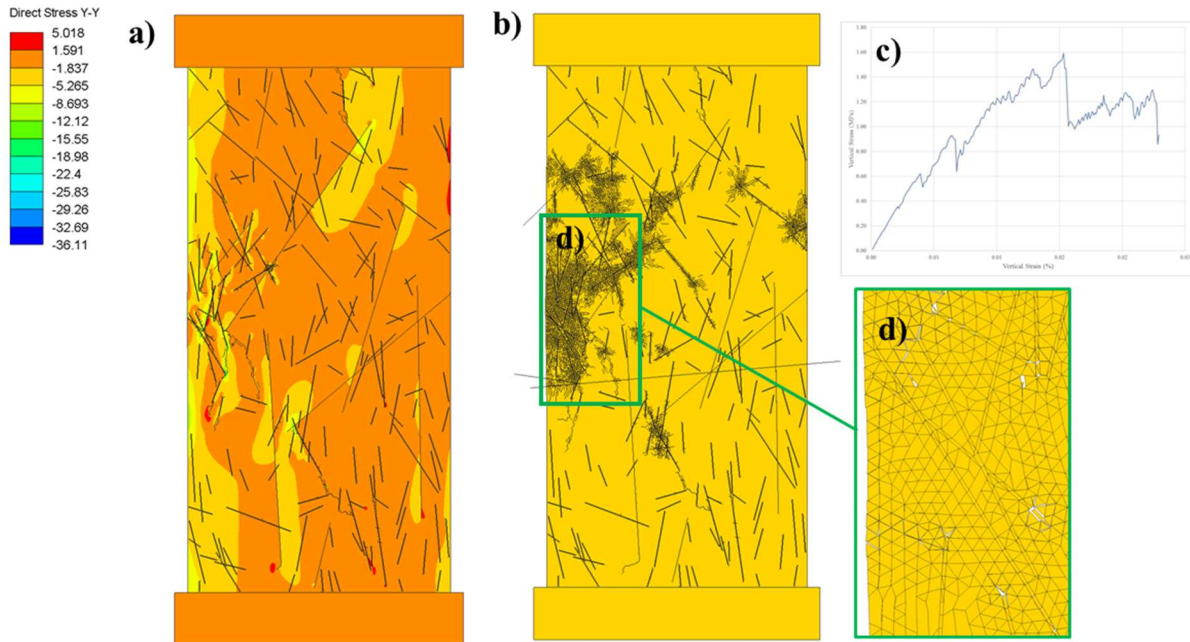
Where:

Qm = mesh Quality (from 0 to 1, being 1 the higher quality)

Li = Length of the i-th element

Hmin = Minimum height of the triangle

Ideally all elements should have a quality ratio  $>0.15$ , but this criterion showed to be insufficient to achieve numerical stability (quasi static condition) in SR models when an element size  $>5$  mm was used for defects. **Figure 4.8** shows a numerically unstable 1x2 meter UCS SR sample. In this model Qm is  $>0.15$  and mesh size is 8 mm for all elements. Note that strain-stress curve (c) seems to have the correct shape and the mesh elements inside the defects (d) does not look particularly long or acute at first view.



**Figure 4.8.** Numerically unstable 1x2 meter UCS SR test including defects and joints a) SR with incipient cracking b) Abnormal cracking 0.005 seconds after crack onset (at that time the model crashed) c) stress – strain curve d) Zoom in to anomalous zone, note that mesh elements in defects are not particularly long. Qm for all elements is  $>0.15$  and 98.5% of elements has  $Qm>0.5$

The issue showed in Figure 4.8 is related to the mesh accommodated by defects. It was found that a maximum mesh size of 5 mm for defects was suitable to avoid numerical instability. Thus, SR's mesh size was constrained by the capacity of defects to accommodate elements of acceptable quality. In the same manner, acute angles between defects and other possible sources of long meshed elements were eliminated from the base DDN manually.

Mesh quality can be highly improved not only using DFN cleaning procedures but reducing the element size. In addition, a fine mesh prevents possible mesh dependency of the SR results, but for big samples, the resultant model cannot be solved in a time effective manner due to its computational cost.

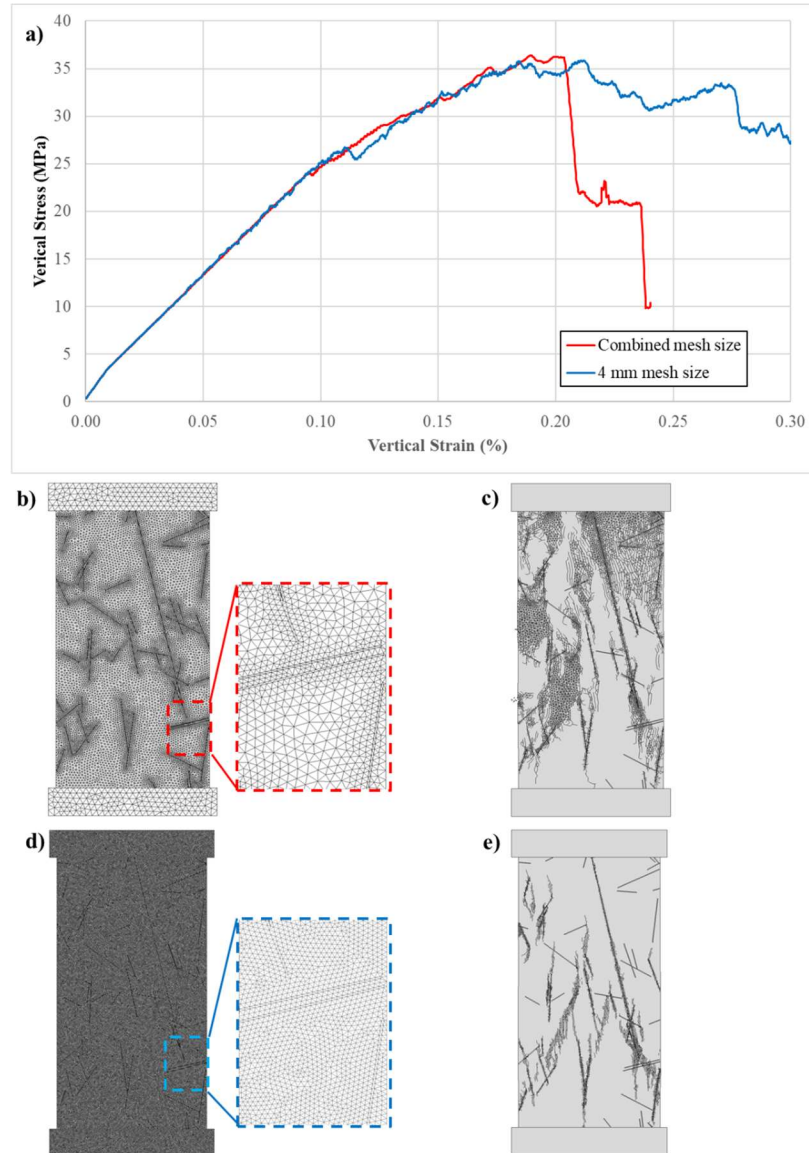
#### **4.5.2 Mesh size dependency**

In fdem numerical simulation, fracturing pattern and strength response can be conditioned by the mesh elements size. For large scale numerical simulations, with elements size in the order of tens of centimeters, Elmo et al (2016) recommend the upscaling of material properties applying the formulation of Hoek and Brown (1980). Given the size of the mesh elements used here, no upscaling of this type was needed.

Potential mesh dependency was tested in a 500x1000 mm numerical sample with defects, subject to biaxial compression under a confinement of 3 MPa. Two mesh arrangement were applied to a unique geometry: a 4 mm triangular mesh and a combined mesh size, with 5 mm in the defects and 10 mm in the rock matrix (**Figure 4.9**). In addition, the combined mesh was set to allow intra element fracturing (**Figure 4.8b**) in the 10 mm elements corresponding to rock matrix. The 4 mm mesh size was considered fine enough to avoid conditioning of strength.

Both samples showed numerical stability, reaching peak strength at approximately 36 MPa and at similar strain. Thus, strength response was considered not affected by combined mesh sizes and safe to apply to SR samples. Post peak behavior was brittle for the combined mesh and plastic for single element size. The main difference lies in the fracturing pattern. While the single size mesh showed well defined shear bands of coalescence of new fractures, this expected fracturing pattern was absent in the combined mesh sample. It was later verified that the absence of shear bands in

the combined mesh was linked to intra element fracturing and not to the mixed mesh. Therefore, although the intra element fracturing capacity seems appealing, it yields less realistic fracturing patterns, at least for combined mesh samples; it did not affect the peak strength.



**Figure 4.9. Results of biaxial test on 500x1000 mm sample with defects. a) stress-strain Curve showing similar pre peak behavior and peak strength. b) Combined mesh with 10 mm elements in the rock matrix and 5 mm elements in the defects. Coarser mesh in the platens has no influence in the test. c) Combined mesh sample at 0.24% vertical strain showing poor development of shear bands. Intra element fracturing was used in this simulation. d) Single size mesh with 4 mm elements size. e) Single size mesh at 0.24% vertical strain showing well developed shear bands.**

Based on results presented above, an unstructured triangular mesh with no inter-element fracturing was used. Mesh size in SR models was set equal to 2 mm for smaller samples (50x100 mm). For SR samples of 1x2 meters an element size of 4 mm for veins and 6 mm for rock matrix was set up. These settings result in a mesh of approx. 160,000 elements for 1x2 meter samples. The cost of mesh size constraints due to defects width is longer running times.

#### 4.5.3 Critical time step and computation time

In Elfen, the time to run a model is determined by the critical time step and the number of elements in the mesh. Critical time step is the differential of time used in the explicit time integration procedure, i.e. the increment of time at which the calculation of the equations of movement, force and contact detection for each element in the model's mesh are performed. It is expressed in Elfen as (Rockfield, 2013):

$$\Delta t_{cr} = \frac{l}{c} \quad \text{where} \quad c \approx \sqrt{\frac{E}{\rho}} \quad (4.4)$$

Where  $l$  is the length of the smallest element,  $c$  is the wave speed (highest frequency of the system),  $E$  is the material Young's modulus and  $\rho$  the material density. Therefore, time step is a function of mesh size. As critical time step does not ensure numerical stability (Klerck, 2000), it is multiplied by a user defined factor (from 0.1 to 1) to obtain final time step to be used in ELFEN. Time step is recalculated during the simulation to account for elements resizing and deformation. Finally, the actual time needed to run a model is approx. given by the numerical duration of the simulation divided by the time step and multiplied by the time the computer takes to make the calculations for all mesh element at each time step. For SR models presented in this chapter, running time to obtain complete stress - strain curve varies from 20 hours for 50x100 mm UCS test, up to approx. 15 days for 1x2 meter, having a mesh of approximately 15.000 elements (2 mm mean element size) the former and 160.000 elements the later. In comparison, computation time can be significantly lower when the scale of the model allows bigger size elements. For example, a complete stress – strain curve for a UCS SRM sample of 25x50 meters, compound of around 50.000 elements of 25 cms mean size, can be obtained in approx. 20 hours.



Computation time can be considerably reduced using mass scaling. In this approach, mass is artificially increased to in turn increase time step. It is intended to be used when a small number of tiny elements, whose total mass is insignificant, are conditioning the time step. This must be used carefully as a large change in mass can affect the quasi-static character of the solution (Hamdi, 2015). Mass scaling was tested on a 750x1500 mm UCS samples in this work. Although time step and subsequently computation time was dramatically reduced, stress-strain curves were not comparable with those without mass scaling. Kinetic energy outbalanced 5% of elastic energy, condition which is recommended to ensure numerical stability (Rockfield, 2013). Probably the impossibility of achieve numerical stability when using mass scaling was related to the fact that tiniest elements are not isolated and insignificant, as in the objective of mass scaling indicated above, but rather abundant since they are related to the mesh accommodated by the defects in the SR samples.

Finally, it must be emphasized that time variables in ELFEN does not correlate with real time (Elmo, 2006) and realistic time – deformation relationships cannot be expected. Deformation of SR models in ELFEN is a result of the applied loadings and change in the continuity of the geometry due to fracturing.

#### **4.6 Synthetic Rock tests**

Numerical test under uniaxial compression, biaxial compression and indirect tensile strength (Brazilian) were performed on SR samples composed of a combination of leached Granodiorite (as rock matrix) and the Discrete Defect Network (DDN). Uniaxial compression strength tests were performed at different sample sizes and a strength upscaling curve was calculated based on the relationship proposed by Yoshinaka et al. (2008). Biaxial test in selected samples are used to examine the relationship of size with internal friction angle, cohesion and H&B's *mi* value.

##### **4.6.1 Uniaxial Compression Strength upscaling relationship**

Size and strength relationship have been largely studied in intact rocks using both physical uniaxial compression tests (Lundborg, 1966, Bieniawsky 1967, Hoek and Brown, 1980, Yoshinaka et al, 2008 among others) and numerical simulations (Pierce et al, 2009, Gao et al, 2014, Stavrou and

Murphy, 2018 among others). Thus, reduction of rock strength with sample size increasing is an accepted characteristic of rocks. In accordance with fracture theory (Griffith, 1920), this phenomenon is attributed to the augmentation of the number of flaws or defects in the rock when the size is increased. Defects act not only as weak links in the continuity of the rock matrix but as stress concentrators as well.

Yoshinaka et al. (2008) shows that scale effect can be described, in specimens of same aspect ratio, by the empirical relationship:

$$\sigma_c = \sigma_{c5} (d/50)^{-k} \quad (4.5)$$

Where  $\sigma_{c50}$  is the uniaxial compressive strength of standard size specimens and  $\sigma_c$  is the uniaxial compressive strength of specimens with same aspect ratio but arbitrary diameter  $d$ . Equation 4.5 can be considered a generalization of the relationship proposed by Hoek and Brown (1980), which, based in a compilation of a number of uniaxial compressive test in different rock types, present a  $k$  exponent equal to 0.18, value that is commonly applied (abused?) when upscaling of strength is necessary.

A relationship suitable to any sample shape is derived by Yoshinaka *et al.* (2008) from eq. 4.5:

$$\sigma_c/\sigma_{c0} = (d_c/d_{e0})^{-k} \quad (4.6)$$

Where  $d_c = V^{1/3}$  ( $V$  stands for volume) is referred as equivalent length,  $k = 3/m$ ,  $m$  is a material constant called coefficient of uniformity and  $d_{e0} = 58.1$ , which is equal to standard-size specimen with a diameter of 50 mm and length of 100 mm. This relationship, although not accurate to evaluate strength value, due to shape effect influence, is useful to describe strength ratio. Both equations 4.4 and 4.5 are linked to Weibull's statistical theory of failure (Weibull, 1951).

Using eq. 4.6 to assess the scale effect in different rock types with different aspect ratios, Yoshinaka concluded that strength's scale effect occurs in hard and soft rocks, but  $k$  factor depends on rock type, being the strength reduction less important in soft rock. In the same work,  $k$  exponent ranges from 0.1 to 0.3 for homogeneous hard rocks, and from 0.3 to 0.9 for weathered and/or extensively microflawed rock (**Figure 4.10**).

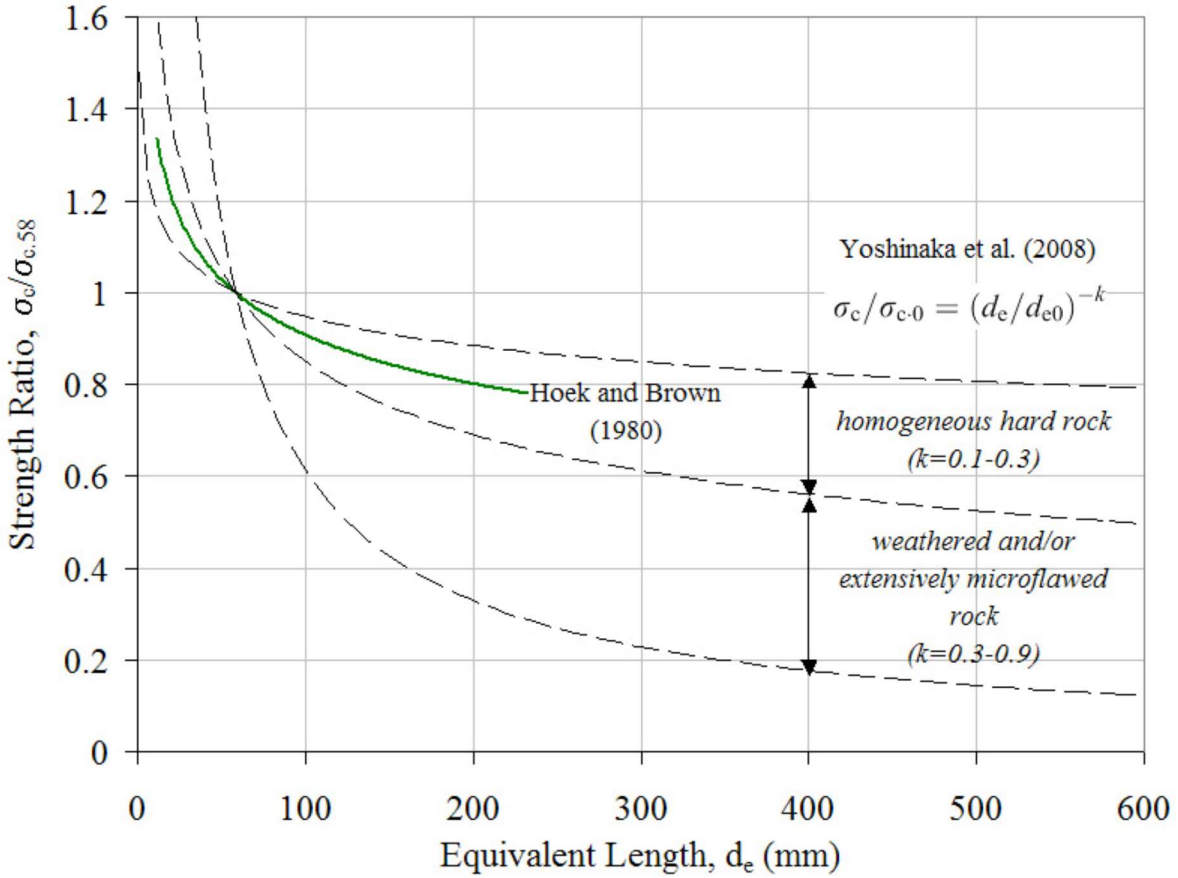


Figure 4.10. Scale effect relations for intact rock UCS proposed by Yoshinaka *et al* (2008). Hoek and Brown relationship ( $k = 0.18$ ) is showed in green (taken from Pierce *et al.* 2009)

In summary, rock strength upscaling is specific of each rock type and can be characterized by the exponent factor  $k$ , applying Weibull's statistic theory of failure. When fracture mechanics is taken in account, characteristics of defects such as geometry, abundance and its individual strength become a key factor.

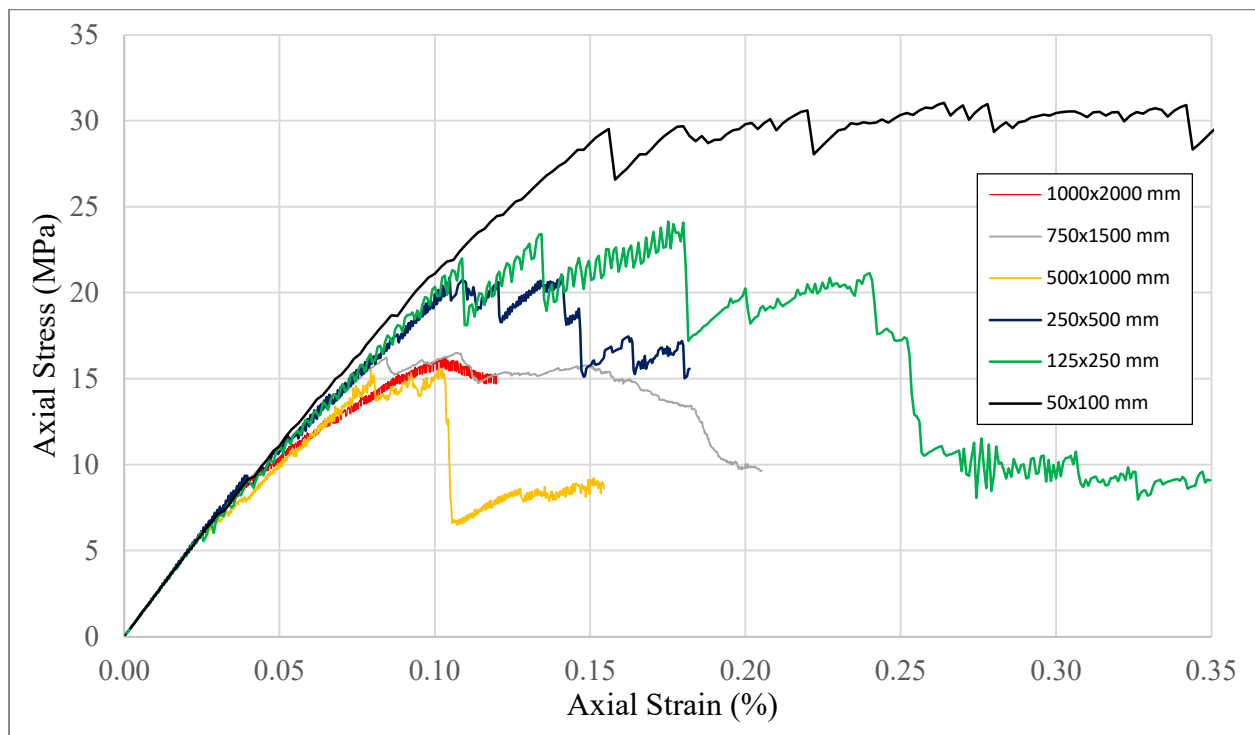
With the aim of obtain upscaling relationship for leached granodiorite, and in particular the  $k$  factor, a series of UCS numerical test were performed on SR samples with defects.

#### 4.6.2 Uniaxial compression strength of Synthetic rock samples

Numerical uniaxial tests were performed to characterize the size – strength reduction for the defected leached granodiorite. Calibrated rock matrix strength for the leached granodiorite, in

combination with DDN and defects properties conform the synthetic rock samples. Aspect ratio was set equal to 0.5 (W:H). Six sample sizes were assessed: 50x100mm, 125x250mm, 250x500mm, 500x1000mm, 750x1500mm, 1000x2000mm.

DFN generation (or DDN in the present case) and the sampling of a DDN realization to assemble a SR is a stochastic process. In accordance, the number of samples to be tested for any given size should be such that the addition of new results does not change significantly UCS mean and variance. Although this desired statistical condition is acknowledged, the number of tested samples was constrained by the time the simulations took to run. Thus, a total of 50 2D SR samples were tested under uniaxial compressive loading. Defects were extracted sampling a single DFN realization. **Figure 4.11** shows six selected stress – strain curves, one for each SR size, while **Figure 4.12** shows the same numerical samples before the test and at peak strength.



**Figure 4.11.** Stress – strain curves for six selected UCS SR samples, each curve represents one of the six sample sizes.

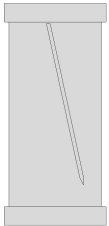
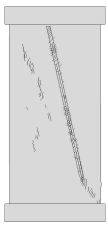
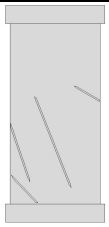


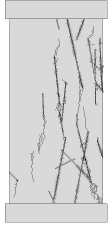

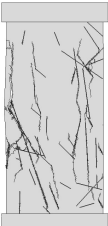




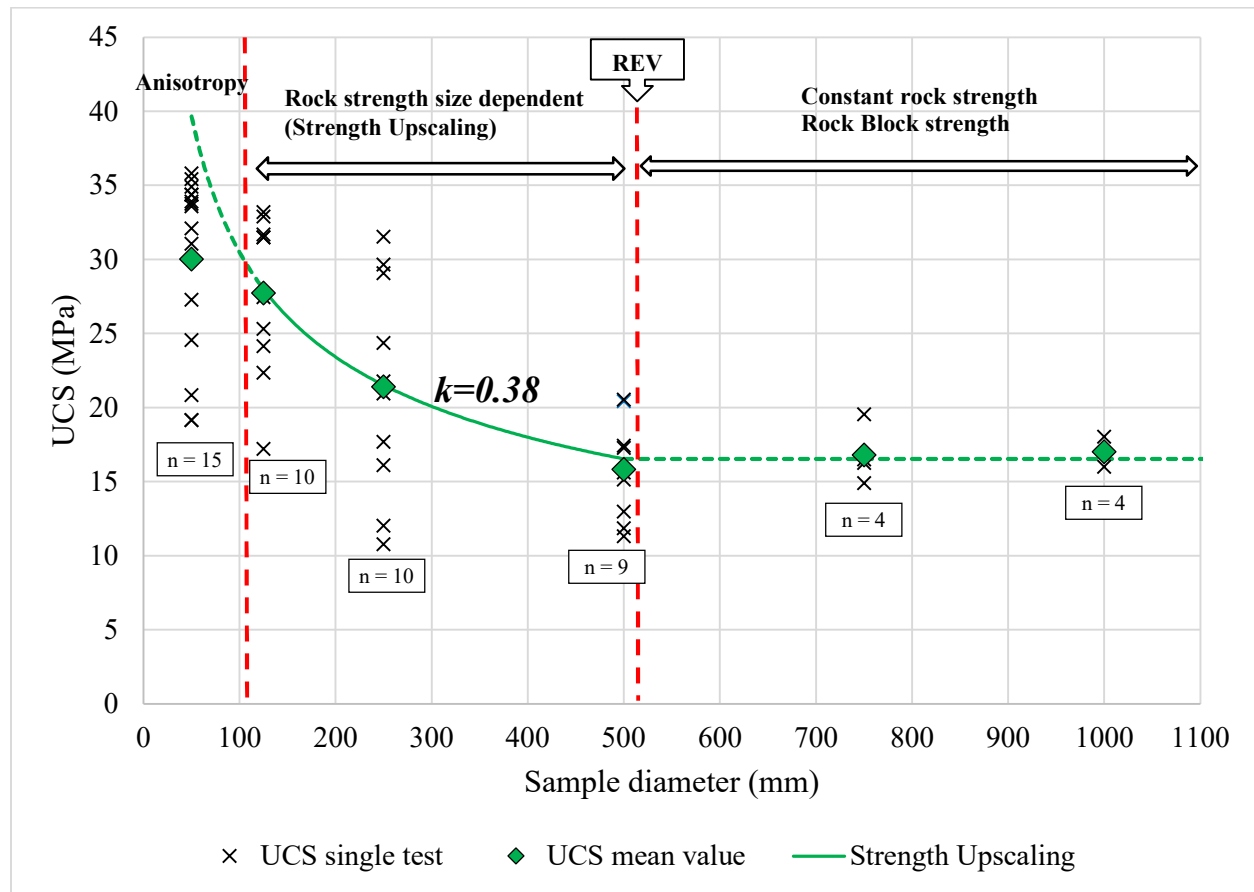
Size (mm)	Defected Sample, pre-test	Defected sample at peak strength	Peak strength Defects Intensity
50x100			UCS = 31.05 MPa P21 = 17.9 (m/m <sup>2</sup> )
125x250			UCS = 24.15 MPa P21 = 9.5 (m/m <sup>2</sup> )
250x500			UCS = 20.94 MPa P21 = 15.8 (m/m <sup>2</sup> )
500x1000			UCS = 15.62 MPa P21 = 10.6 (m/m <sup>2</sup> )
750x1500			UCS = 16.5 MPa P21 = 11.9 (m/m <sup>2</sup> )
1000x2000			UCS = 18.03 MPa P21 = 9.9 (m/m <sup>2</sup> )

Figure 4.12. Selected Synthetic Rock samples for UCS test (same as in Figure 4.9), before loading (pre-test) and at peak strength.

The mean UCS value was calculated for each one of the six size groups. Strength of samples of 50 mm diameter was considered more related to anisotropy, since 8 out of 15 numerical samples include a single defect. On the other side, representative elementary volume (REV) was reached at 500mm size where constant strength of approx. 15 MPa is reached. Strength upscaling in the range of 125-500 mm sample size was characterized using equation 4.6. Therefore, UCS size dependency is characterized by  $k$  exponent equal to 0.38 (**Figure 4.13**), which is congruent with the range proposed for Yoshinaka for an extensively flawed rock (**Figure 4.10**), as is the case of the defected leached granodiorite studied here.

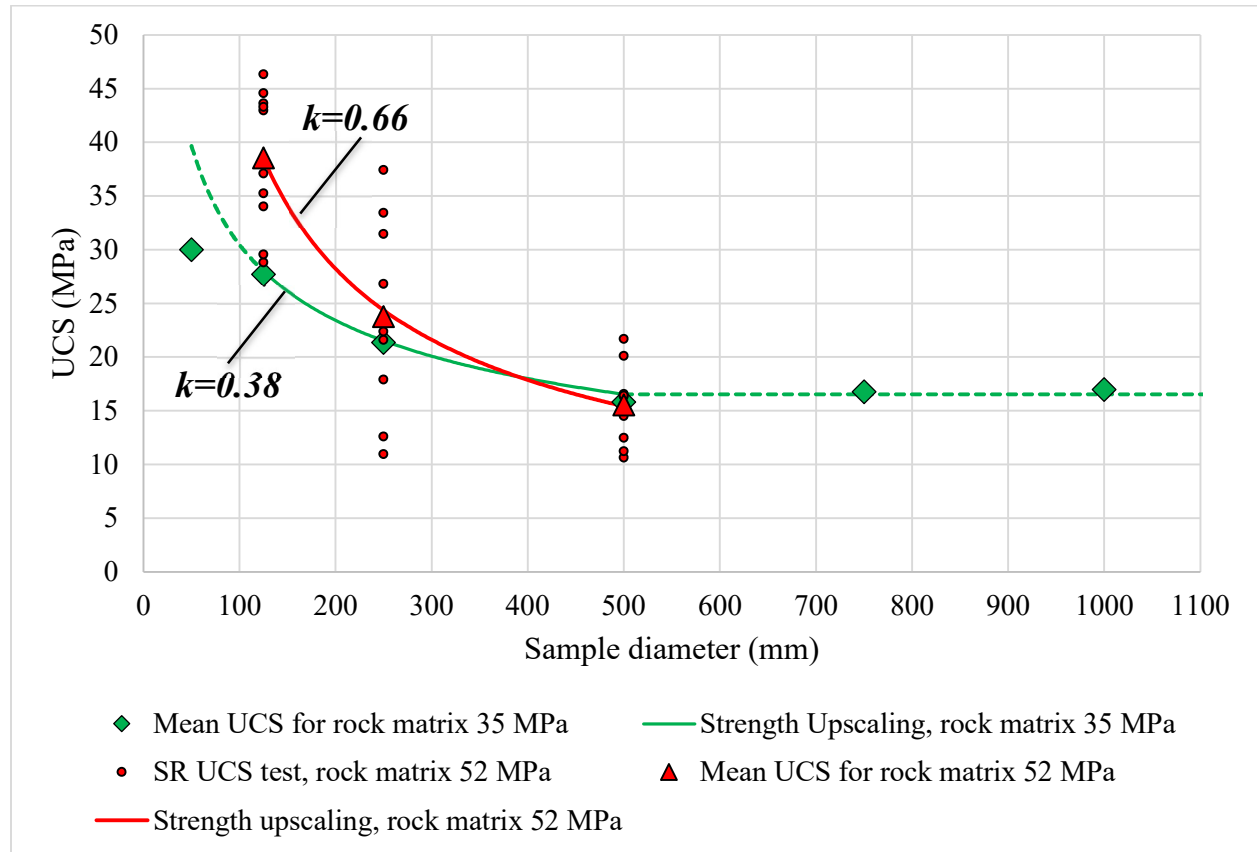


**Figure 4.13.** Synthetic rock UCS vs sample diameter. Exponent  $k=0.38$  in Yoshinaka's relationship (equation 4.6) describes the strength drop in the range 100 – 500 mm sample diameter. (x symbol depicts single UCS test. Averaged UCS for each group size in green. Number of samples (n) indicated for each size)

The three zones proposed in **Figure 4.13** are similar of those described by Bieniawsky (1967) in his investigation of size dependency of strength in cleated coal samples for pillars design, with the

difference that he describes constant strength in smaller samples and relates it to negligible effect of cleats at those sizes.

To explore the effect of rock matrix strength, numerical samples in the range of 125 – 500 mm diameter were re-tested using the same geometry and number of samples showed in **Figure 4.13** but increasing the rock matrix uniaxial strength to 52 MPa. No modification was made on defects strength. The UCS drop is more pronounced in this case and is characterized, applying eq 4.6, with an exponent  $k=0.66$  (**Figure 4.14**).



**Figure 4.14. UCS size dependence for defected rock. In red UCS results and strength upscaling for the defected rock with a matrix of unconfined strength equal to 52 MPa. In green data presented in Figure 4.11 (matrix UCS = 36.5 MPa). Only rock matrix strength was increased, DDN geometry, defects strength and number of samples for each size is same for both cases.**

Numerical experiments performed by Pierce et al. (2009) on veined synthetic samples, showed that strength upscaling effect becomes more pronounced as veins strength decrease. On the other

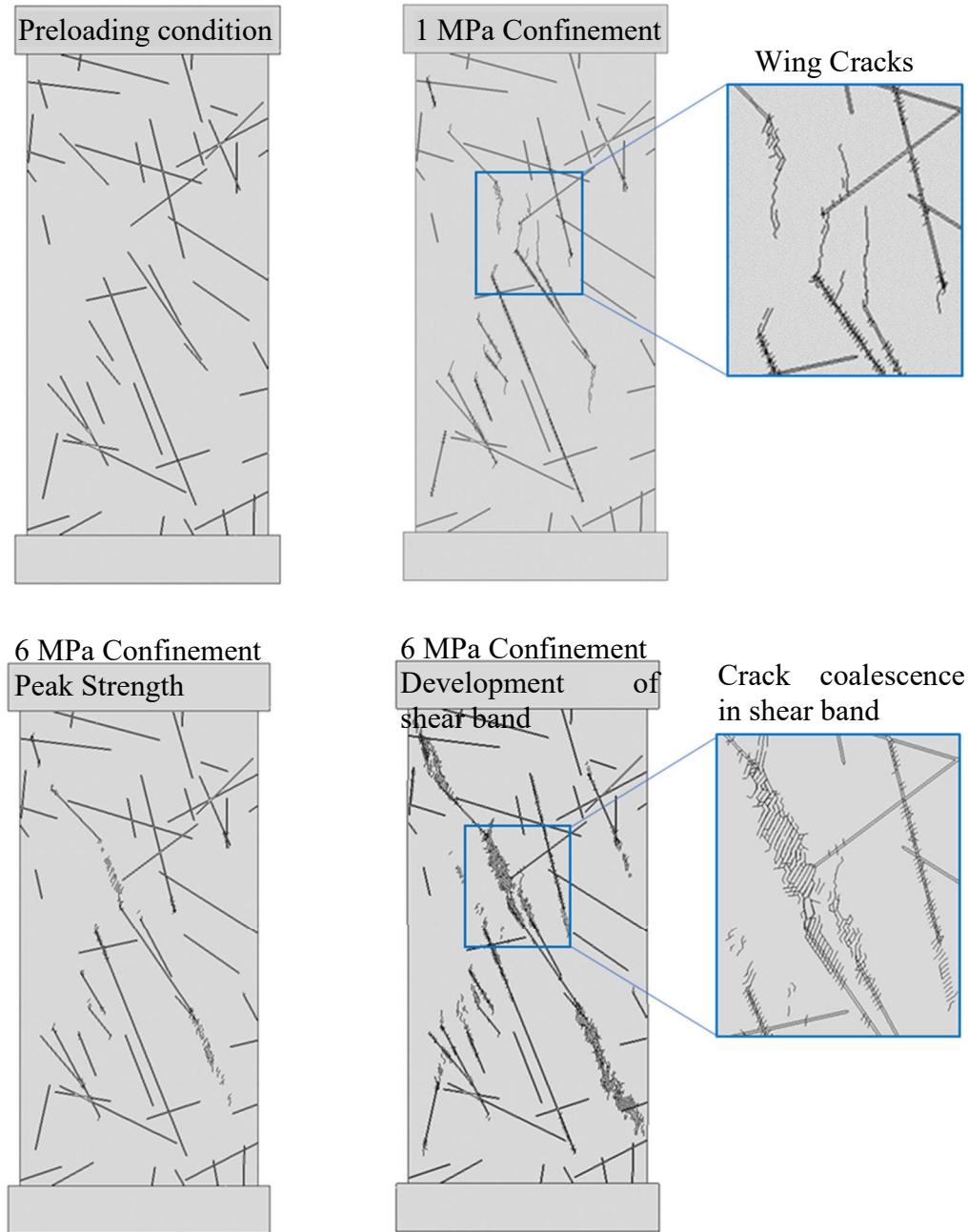
hand, Yoshinaka asserts that scale effect is not significant in weak rocks. Therefore, the drop in the rock strength with size is more marked, and  $k$  exponent higher, when the difference in strength between rock matrix and defects is higher, while strength upscaling is less significative in weak rocks, where difference between defects strength and rock matrix strength is negligible.

#### **4.6.3 Biaxial compression strength of synthetic rock samples**

Two of each 250- and 500-mm diameter synthetic sample were submitted to numerical biaxial test, with confinements from 1MPa to 9 MPa. Selection criteria was minimum deviation from both average UCS and average defect intensity (P21) regarding its group of size.

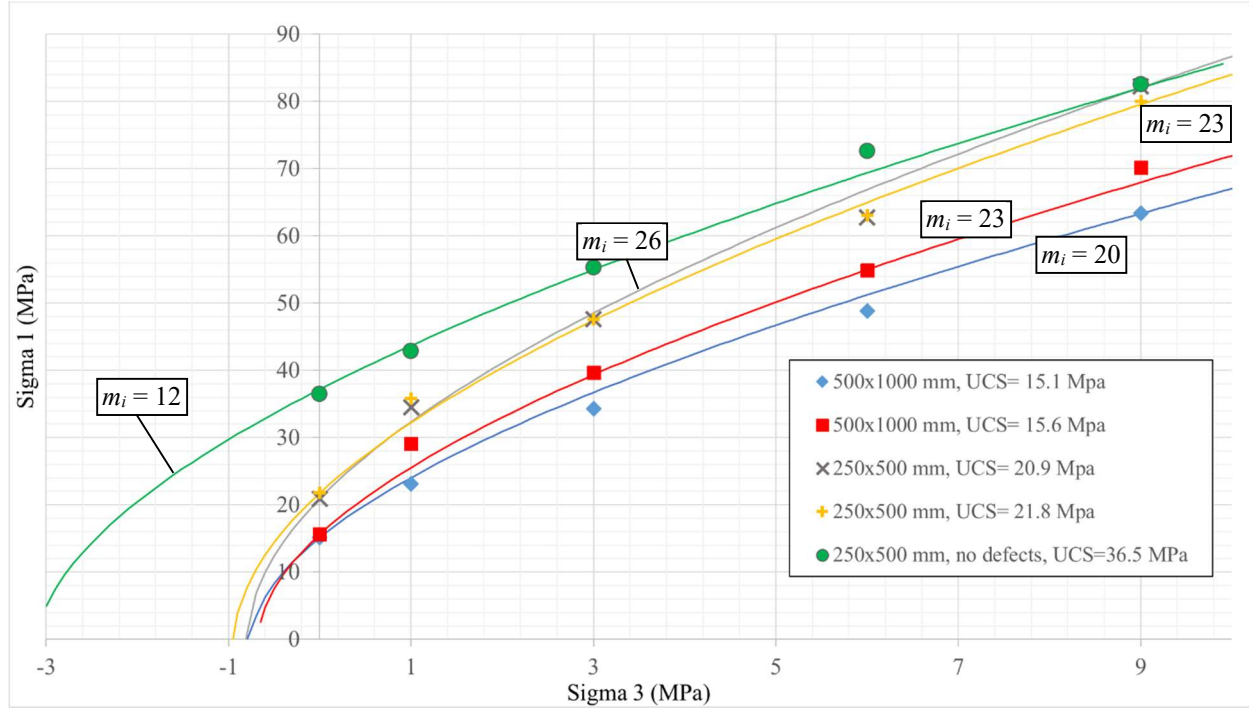
In both, uniaxial and biaxial numerical test presented here, the crack initiation and propagation are coincident with fracture theory initially proposed by Griffith (1920) and with observations from real compression tests. This shows that fracturing mechanics used in ELFEN can fairly represent rock failure. In the current SR models, defects are modelled using a material that includes elastic properties, friction, cohesion and tensile strength. In the same manner as fractures, defects act equally as stress concentrators, generating wing fractures in tension, at the tip of defects at zero and low confinements. Growing of cracks occur parallel to major stress (**Figure 4.15b**). The development of oblique bands of coalescent cracks occur during the test at both low and high confinement, being narrower and well defined in the latter due to the development of a failure in shear (**Figure 4.15d**). Although still present, wing cracks are much shorter at higher confinements. These cracking patterns are in accordance with the failure of rock-type materials in real compression tests (Bobet and Einstein, 1998).





**Figure 4.15. Fracturing patterns in SR biaxial test. a) SR sample, preloading geometry b) 1 MPa confinement biaxial test. Zoom in on the development of wing cracks from defects tip during elastic stage (pre peak strength), parallel to vertical main stress c) 6 MPa confinement biaxial test at the time of reaching peak strength d) 6 MPa confinement biaxial test, zoom-in on crack coalescence in shear band during plastic stage. Same defects geometry and sample size (250x500 mm) for all numerical tests in the figure.**

Compressive vertical loading and confinement were applied at constant velocity, in such manner that both increase at similar rate until reach the desired confinement, at which point vertical loading continued growing linearly while horizontal loading was kept constant. Stress and strain were recorded during the test using history points. H&B's failure envelope was fitted to biaxial results by “manual” process, using UCS as “pivot” point and adjusting  $m_i$  parameter until obtain a satisfactory fit to biaxial test data (**Figure 4.16**).



**Figure 4.16. Biaxial strength of four selected SR samples with defects and non-defected sample (in green). Continuous line show fitted H&B failure envelope characterized by sample UCS and  $m_i$  parameter (in rectangle). Curve and dots in green correspond to sample with no defects.**

The  $m_i$  parameters that fits failure envelope to SR biaxial test varies from 20 to 26. Test of different  $m_i$  parameters in this range showed that the average value of  $m_i=23$  offer a good fit for all the SR data. Based on laboratory triaxial test, Bewick et al (2018) suggest a range of 1.3 – 1.9 times the  $m_i$  of the undefected rock for veined samples with mixed rupture, ascribing the increasing of the value to the high dilatancy of the defected samples at low confinement. For the present numerical experiment,  $m_i$  from real triaxial test of the rock matrix (the undefected rock) is equal to 11.3, while numerical SR biaxial test on non-defected sample ( $m_i=12$ , **Figure 4.16**) is in good agreement

with the real undefected rock. Taking in account the dispersion of SR biaxial results and the sensitivity of  $m_i$  to the “manual” fitting process used here, results from biaxial numerical experiments on SR can be considered congruent with the findings of Bewick et al. (2018) on real biaxial test data of veined rock samples. As pointed by the same authors, this implies that at higher confinements the strength of defected samples tends towards the strength of non-defected rock, but never reaches it. Synthetic rock results presented in **Figure 4.16** seems to be in opposition with this observation around the 9 MPa confinement for two cases (orange and grey envelopes). SR does not include any microcracks, millimetric vein or altered mineral grains nor any other “microdefect”, that normally occur together with “macrodefects”, which likely weakens the rock matrix. Due to difficulties to properly characterize these “microdefects” and computational effectiveness, this natural heterogeneity is “flattened” using a single set of properties for the rock matrix, being the calibrated matrix in the current SR an equivalent continuum for the real “microdefected” rock matrix. Thus, the lack of these features in the SR sample can lead to reach the rock matrix strength at high confinement.

Cohesion and friction angle were calculated for H&B envelopes in **Figure 4.16** using the formulation proposed by Hoek et al. (2002). Results of defected SR showed that while friction angle is practically size invariant, cohesion is inversely related to sample size (**Table 4.4**). This is concordant with the findings of Hamdi et al (2015) on microdefected synthetic numerical samples, when defects intensity is increased on samples of fixed size. Although, differently than Hamdi et al, as here the size is increased, the variation of physical properties in both cases is exerted not by the change in size, but due to the augmentation of the number of defects related to sample size increasing.

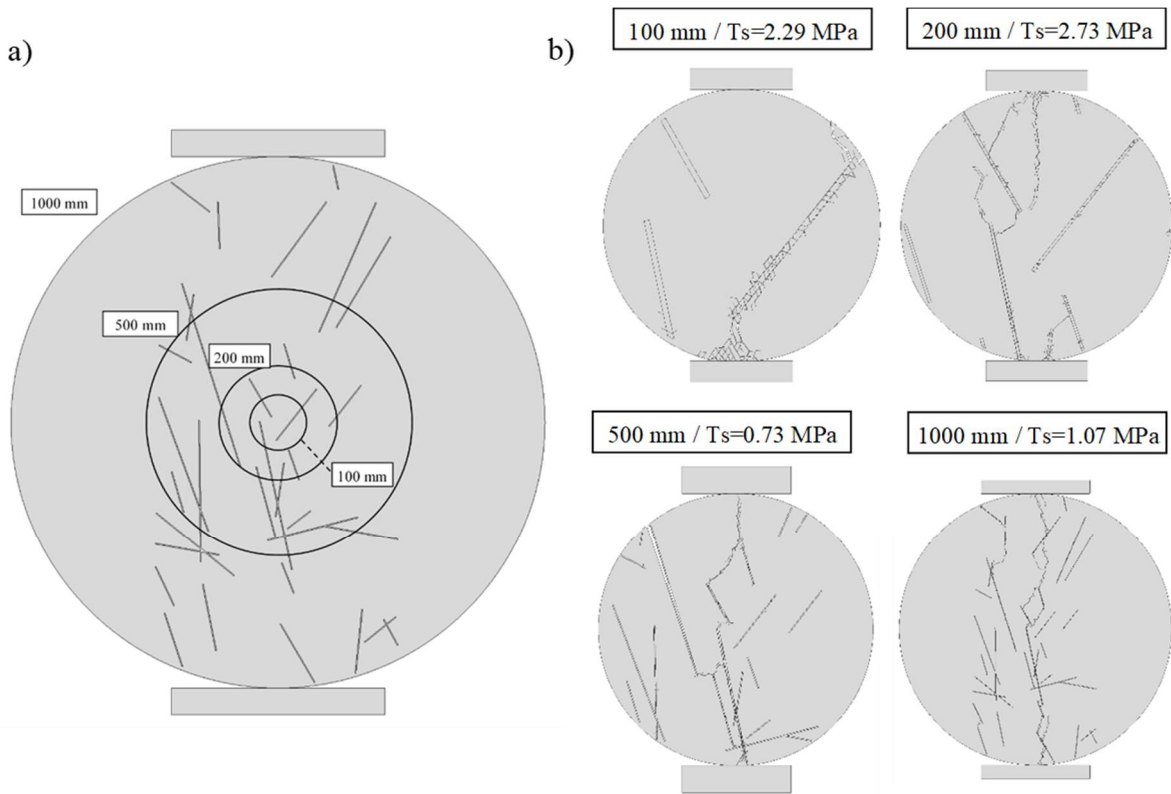
**Table 4.4. Mohr Coulomb and H&B properties characterizing biaxial test in Figure 4.16**

Sample size (mm)	Type	UCS (MPa)	$m_i$	Cohesion (MPa)	Friction angle (degrees)
250x500	undefected	36.5	12	6.3	49
250x500	defected	20.9	26	3.3	54
250x500	defected	21.8	23	3.5	53
500x1000	defected	15.1	20	2.4	53
500x1000	defected	15.6	23	2.4	54

While friction angle shows a practically null dispersion,  $m_i$  is in the range of 20-26. Although both  $m_i$  and friction angle are related; rock matrix UCS, tensile strength and a  $k$  coefficient play a role at confined strength (Hoek and Brown, 2018), which can explain the higher range of variation.

#### 4.7 Indirect tensile strength of synthetic rock samples

Indirect tensile strength (Brazilian test) was tested on four SR samples. The test consisted in a bidimensional disc shaped sample with two platens exerting the loading vertically. A single DDN realization was used in four samples with diameters of 100 mm, 200 mm, 500 mm and 1000 mm (Figure 4.17). Material properties were the same applied to uniaxial and biaxial test.



**Figure 4.17. a) Four disc samples were tested under indirect tensile strength. b) Fracturing pattern after reaching peak tensile strength (Ts), size in mm indicates sample diameter.**

As expected, anisotropy plays an important role in the tensile strength obtained for each sample (Figure 4.17). Certainly, more than one sample per each size is necessary to obtain a statistically robust description of scale effect in tensile strength, however the limited quantity of tested samples

was useful to verify that tensile strength decreases while size increases. Given that the REV for UCS was reached at 1 m length samples (500 mm diameter samples), the Tensile strength obtained for 1000 mm diameter sample can be fairly assumed as the upscaled tensile strength.

#### **4.8 Uniaxial strength of the defected leached rock in combination with joints**

As showed previously, rock strength upscaling is a well established characteristic of rock materials and it is controlled by the quantity, size and strength of defects, veins, mineral contacts or any other weakness existent in the rock matrix. The next step is to explore the effect of strength upscaling on rock mass failure. Admitting the failure as a breakage conducted through a combination of rock matrix and joints, the problem is defined, on the side of rock matrix, by the strength of rock bridges. On this regard Elmo et al (2018) acknowledge the size dependency of strength as an important factor when evaluating step-path failure and propose individual upscaling of cohesion and friction angle depending on size of each rock bridge. This can be depicted comparing two failures, both involving same proportion *rock matrix/joint*, one having a single, longer, rock bridge, while the second has the rock matrix breakage distributed along a number of shorter rock bridges. In this example, the latter yields a higher strength, no matter whether one is measuring shear strength or strength under compression. For this to be true, rock bridges must be shorter than REV, at least in the second case. The difference in strength between both cases will be related to strength drop with size or, mathematically, by the  $k$  factor in equations 4.5 and 4.6. In the extreme, when rock bridges are larger than REV, minimum rock matrix strength acts.

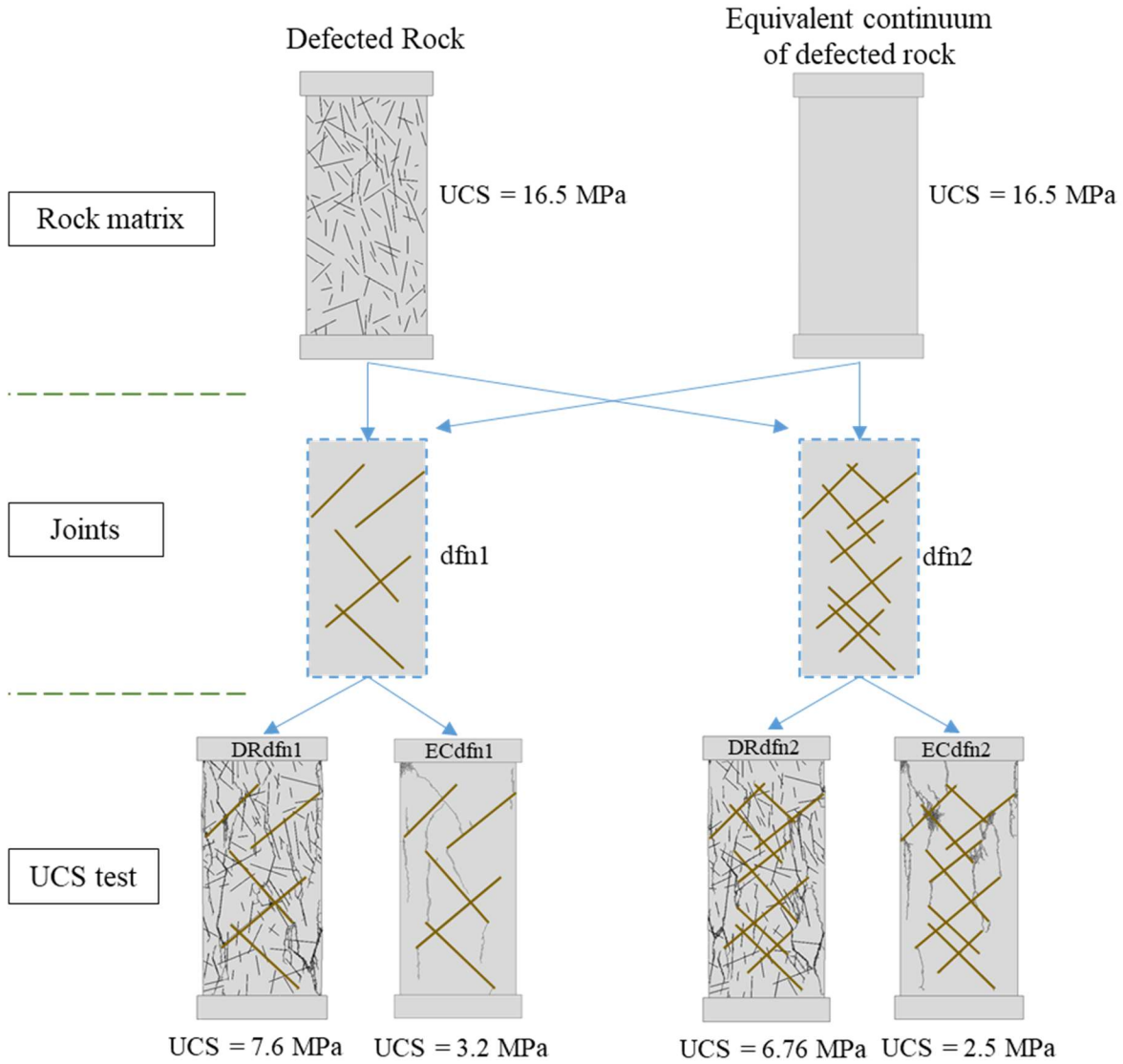
To explore the strength of the defected rock in combination with joints, a uniaxial compression test with multiple joints was assembled. It is emphasized that computational constraints prevent the use of defected rock masses at a size large enough to overpass rock mass REV. Thus, the numerical experiments showed here were not intended to obtain a complete answer for the problem, but to orientate on how important strength upscaling of rock bridges is.

##### **4.8.1 Strength of rock bridges in a defected rock with joints**

The experiment consisted of 2 types of rock matrix samples, the defected rock and the equivalent continuum of this rock with no implicit defects, in combination with two DFN realizations. Thus,

4 geometries were assessed under uniaxial compression in a sample of 1.5 x 0.75 m. The two DFNs were comprised of 5 inclined fractures (dfn1) and 10 fractures (dfn2), the second was assembled adding 5 extra fractures to the initial geometry dfn1. Friction angle was set up equal to 35° and no cohesion was used for fractures in the two cases.

Defected sample corresponds to one previously used to obtain strength upscaling, properties for defects and matrix were not changed. Overall UCS of the defected rock sample of 1.5 x 0.75 m was equal of 16.5 MPa after compression test. H&B's  $m_i$  was assumed equal to 23 based on biaxial test showed previously in this chapter. These values were used to obtain equivalent cohesion and friction in Rocdata software to build equivalent continuum sample, i.e. a plain sample with the overall strength of the defected rock. The defected rock and its equivalent continuum were then combined with dfn1 and dfn2 to be submitted to unconfined compressive test. Samples were named: DRdfn1 and DRdfn2 for the defected rock, ECdfn1 and ECdf2 for its equivalent continuum (**Figure 4.18**).



**Figure 4.18.** Sample assemblage of defected rock, and its equivalent continuum, with 2 joint networks. UCS yielded from the numerical simulation is presented at the bottom of the figure.

The defected rock yielded a UCS approximately 2.5 times the strength of the equivalent continuum sample (**Figure 4.18**). This difference can be explained by the rock bridges and its strength upscaling. For equivalent continuum sample, strength of rock bridges does not vary with its length and it is approximately 16.5 MPa in every place of the sample. Considering this fact, and the higher overall UCS in the jointed sample, it can be deduced that rock bridges in the defected rock (with joints) are stronger than 16.5 MPa. This is due to strength of rock bridges in the defected rock depends on the proportion of “matrix” and defects participating the rupture. Since, in the jointed

defected rock, rock bridges are shorter than the rupture happening in the non-jointed 1.5x0.75 m defected sample, they incorporate less defects and hence they are stronger than the overall 16.5 MPa. The mechanism is the same operating for strength dependency of sample size. It is not the sample size directly producing the strength upscaling, although the shape ratio has an influence, but the length of the breakage(s) at failure.

The mean strength of the defected matrix in the jointed sample can be calculated using H&B's formulation once GSI for DFN's 1 and 2 are known. This was achieved assembling SR samples of known UCS, together with dfn1 and dfn2, and back calculating GSI. In this manner, GSI are approximately 75 and 72 for dfn1 and dfn2 respectively. It must be remarked that GSI was used here as mathematical mean to obtain rock bridge strength, these calculations are not implying the feasibility of GSI for fracture networks with values higher than 65, in which cases its application must be exerted carefully. H&B application in massive rock masses has showed low reliability to predict spalling depth and damage in tunnels at moderate to high stress. Discussion on the limitations of GSI for blocky to massive rock masses ( $GSI > 65$ ) can be found in Diederich (2002) and Bewick et al (2018), among others. Finally, the application of H&B's formulation here is based on: all inputs of the experiment are known, the experiment is developed under no confinement.

Applying H&B's formulation to the back calculated GSI, a rock matrix UCS ( $\sigma_{ci}$ ) of 30.5 MPa is obtained for defected rock in the sample including dfn1, while 32 MPa for defected rock and dfn2. These values can be considered the average strength of rock bridges for the tested numerical samples. It must be recalled that the defected rock consists of a matrix of UCS equal to 36.5 MPa plus weaker defects and is this combination that control rock bridges strength. It is no coincidence that the more fractured sample (DRdfn2) yielded higher average strength for rock bridges. As expected for a more fractured sample, overall strength is lower than DRdfn1, but, since rock bridges are shorter in the more fractured DRdfn2, the strength for rock matrix is slightly higher, in accordance with strength upscaling with size (at shorter breakage, higher strength).

Considering the strength upscaling relationship showed in **Figure 4.13**, rock bridges for the defected rock are in the extreme of higher values. This probably is more related to geometrical particularities of the tested samples and cannot be generalized to a rock mass due to the reduced



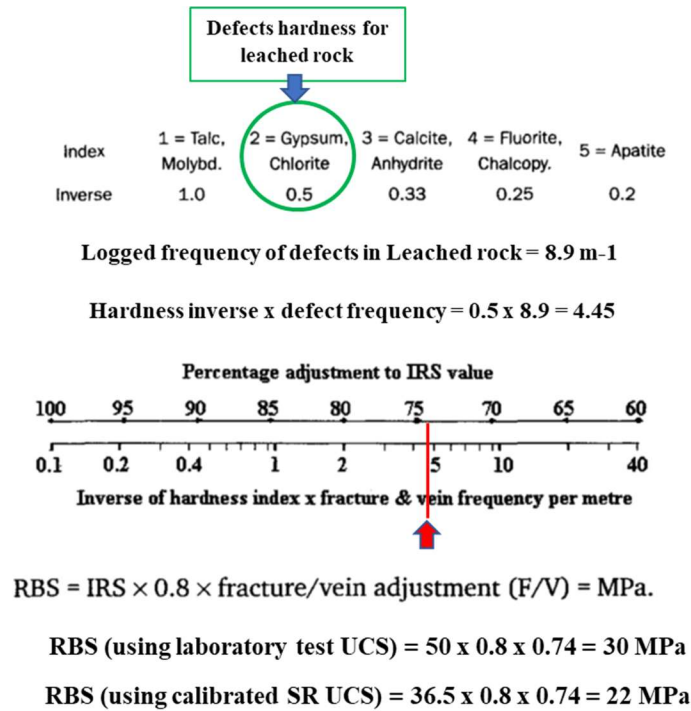
size of the sample and given that the upscaling phenomenon is stochastic in nature. Only general conclusions can be extracted from this experiment. Given that the overall strength of a rock mass is dependent of the length of rock bridges at failure, and strength upscaling operates on rock bridges too, strength upscaling must be considered to derive the rock mass strength as asserted by Hoek and Brown (2018)

#### **4.9 Other methods to upscale defected rock strength**

Two methods to obtain upscaled strength are presented: MRMR rock block strength (Laubscher and Jakubec, 2000), which estimates rock block strength directly based on characterization of defects, and Compound GSI method (Day et al, 2012, Day, 2016) which incorporates the defects network into GSI.

##### **4.9.1 MRMR Rock Block strength (Laubscher and Jackubeck, 2000)**

Laubscher and Jakubec (2000) address strength upscaling of defected rocks introducing adjustment to rock block and rock mass strength into IRMR/MRMR classification system. In their method, intact rock strength (IRS) is corrected first accounting for the intercalation of weaker rock material by means of a nomogram. Then, rock block strength (RBS) is calculated adding a new correction, dependent of the intensity of defects (frequency/m) and the inverse of the hardness of their infill. Since there is no intercalation of weak rock in the current case, only the correction due to defects was applied. **Figure 4.19** shows the calculations performed with data from the leached rock.



**Figure 4.19. Laubscher and Jakubec (2000) procedure to calculate rock block strength, applied to leached granodiorite data.**

IRS in this method refers to the rock matrix strength with no defects. When UCS from laboratory test with rupture through matrix is used (50 MPa), the calculated rock block strength matches almost perfectly the real laboratory UCS of 10 cms samples length with mixed rupture (matrix + defect). This value is still higher than the actual rock block strength, due to it should be less than the UCS at the size of 10 cms sample. On the other hand, it doubles the UCS of the REV (15 MPa) obtained from SR numerical samples. The actual UCS for the rock matrix of the defected leached rock is likely lower than the measured from laboratory test, due to non-defected samples tend to be less altered than the actual rock matrix in defected samples, causing overestimation. Then, when the calibrated rock matrix strength of 36.5 MPa is used, an RBS of 22 MPa is obtained, nearer of the 15 MPa from SR REV.

#### **4.9.2 Composite GSI (Day et al 2012, Day, 2016)**

Day (2016), defines intrablock structure as veins, stockworks and healed defects in general occurring in the rock blocks delimited by joints. She highlights the influence of intrablock structure

in rock mass behavior and mechanical properties. Day et al (2012) and Day (2016) propose intrablock structure inclusion in the rock mass characterization replacing H&B's failure criteria GSI with a compound GSI (CGSI) value, which in turn is based on Cai et al (2004) GSI calculation. Thus, CGSI is a method to incorporate the effect of the intrablock structure into the rock mass strength using H&B's failure criteria, but it is not intended to obtain an upscaled strength for the rock block.

Operationally, CGSI consist of the calculation of factors related to joint condition (scale A) and Block Volume (scale B), for both joints and defects. Then, these factors are combined in a unique CGSI number. **Figure 4.20** shows CGSI applied to the leached granodiorite. Detailed explanation of the method can be found in Day (2016).

As showed in **Figure 4.20**, for the case of the leached rock, CGSI (43) is almost the same than the calculated GSI for joints (42), diluting almost completely the effect of defects in the calculation. On the other hand, it can be noticed that the method does not differentiate the scale at which each set (types) of structures are occurring, therefore it works under the assumption that all structures present in the rock mass (joints and defects or veins) have the same scale. While for veins with lengths in the order of meters such assumption can be arguable true, it is not applicable when defects are less continuous than joints, as is the case of the leached rock.

Given the results obtained for the leached rock, it is clear CGSI is not suitable to be applied to it. Regarding the core idea of CGSI using it to account for the effect of defects, Hoek and Brown (2018) asserted that there is no reason to not use GSI to reduce strength of samples with defects. Although is not in the scope of the present work, an alternative procedure is suggested, applying GSI in a staged manner. In a first stage, rock block strength could be estimated using a specific GSI chart for defects and then, in a second stage, use this rock block strength as input for rock mass strength estimation applying H&B's failure criteria. The complete approach should include adjustments to  $m_i$  value as well.

Table 3-1: Modified Joint Condition rating, Modified JCond<sub>89</sub>, to include intrablock structure

Condition of discontinuities	Strengthening intrablock structure Strong infill minerals welded to wall rock	Very rough or healed surfaces Not continuous No separation Unweathered wall rock	Slightly rough surfaces or weak veins Separation <1mm Slightly weathered walls	Slightly rough surfaces Separation <1mm Highly weathered walls	Slickensided surfaces or Gouge < 5 mm thick or Separation 1-5 mm Continuous	Soft gouge > 5 mm thick or Separation > 5 mm Continuous
Overall rating	37.5	30	25	20	10	0

Guidelines for classification of discontinuity conditions

Discontinuity length (persistence)	< 0.5 m <b>D</b>	< 1 m	1 to 3 m	3 to 10 m	10 to 20 m <b>J</b>	> 20 m
Rating	7.5	6	4	2	1	0
Separation (aperture)	Welded <b>D</b>	None	< 0.1 mm	0.1 to 1.0 mm	1 to 5 mm <b>J</b>	> 5 mm
Rating	7.5	6	5 <b>J</b>	4	1	0
Roughness	Rough, undulating, irregular	Very rough	Rough	Slightly rough <b>D</b>	Smooth	Slickensided
Rating	7.5	6	5	3 <b>D</b>	1	0
Infilling (gouge)	Strong bonded vein (quartz)	None	Hard filling < 5 mm	Hard filling > 5 mm <b>J</b>	Soft filling < 5 mm <b>D</b>	Soft filling > 5 mm
Rating	7	6	4	2	2 <b>D</b>	0
Weathering	Strengthening by alteration	Unweathered	Slightly weathered	Moderate weathering <b>J</b>	Highly weathered <b>D</b>	Decomposed
Rating	7	6	5	3	1	0

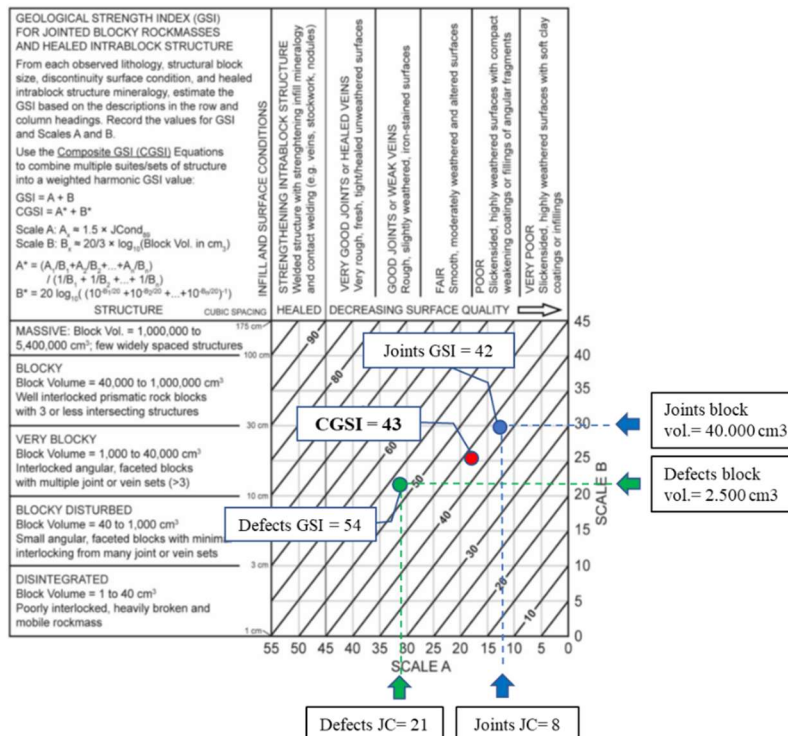


Figure 4.20. a) Modified Joint condition ratings (modified by Day, 2016, from Bieniawsky, 1989), circled: in green ratings for defects, in blue ratings for joints. Raw data for ratings from drillhole mapping and bench mapping. b) CGSI chart (Day, 2016). Block volumes obtained from DFN of defects and joints using Sybill algorithm in Fracman. Joint Condition (JC) from table in a. Calculations performed as indicated in upper left quadrant in the chart.

#### 4.10 Conclusion

Size dependency of strength is a well-known characteristic of rock and has been studied in the past (Beniawski, 1967, Hoek and Brown, 1980, Yoshinaka et al, 2008, among others). It is specific for the rock type and depends of the quantity and geometry of defects and their strength. The obtention of samples to assess strength upscaling experimentally is difficult and expensive, therefore it is rarely included as part of the geotechnical evaluation of mining projects. Indirect assessment of strength upscaling can be performed when rock matrix and defects are characterized properly. The importance of classify and analyze laboratory test by failure type (rock matrix, mixed rupture or defect) and obtain defects strength has been highlighted by the rock mechanics community (Russo and Hormazabal, 2016, Bewick et al 2018). Synthetic Rock modelling is not possible without this information, which obtention does not require an important monetary investment but the adaptation of procedures to analyze laboratory test samples and data.

Synthetic rock experiments presented here were calibrated on a set of UCS laboratory test showing mixed rupture. The available information was not detailed enough to replicate each real laboratory test. In any case, to perform numerical experiments aiming the simulation of each single real test is likely timewise unpractical. Therefore, the numerical experiments developed here are intended to address the stochastic nature of the upscaling problem, simulating the rock failure in a fair manner. Thus, the validity of the numerical tests was verified through the development of realistic cracking patterns in the form of coalescence and development of shear bands. Crack onset for samples of 1.5 m and 2 m height was around 50% of UCS, which is consistent with actual lab tests. The fact that confined tests results can be fitted with H&B's failure envelope is considered part of the validation of the SR experiment. In addition, the increasing of H&B  $m_i$  values for the defected rock are concordant with actual laboratory tests performed on veined samples (Bewick et al, 2018).

Unconfined strength upscaling was obtained from a series of UCS numerical tests of sample diameter in the range of 0.1 m – 1 m. Yoshinaka et al (2008) application of Weibull's statistical theory shows a remarkable good agreement when fitted to average UCS of each sample size class. A  $k$  constant of 0.38 characterizes the strength drop until the diameter of 0.5 m, where REV is reached at a UCS strength of 15 MPa. Results from unconfined biaxial test indicates that while

cohesion is size dependent, friction remains relatively constant. Tensile strength showed to be size dependent as well.

Alternatively, two methods to account for the effect of defects in rock strength upscaling were applied to the leached granodiorite data, namely rock block strength estimation (Laubscher and Jakubec, 2002) and composite GSI (CGSI, Day et al, 2012, Day, 2016). While the former yielded rock block strength higher but near the REV strength obtained from SR, the latter showed not be suitable to be applied to the leached rock, due to there is no much difference in the CGSI in comparison with calculated regular GSI.

A numerical sample of the defected rock in combination with joints was assembled, verifying scale effect on rock bridges. Thus, although the specific result cannot be extended to rock mass, it demonstrates that to derive the strength of a rock mass, scale effect of intact rock must be considered. Regarding their failure criteria, Hoek and Brown (2018) address this topic in the following manner “...it has been assumed that the intact rock specimens are homogeneous and isotropic and that the values of the unconfined compressive strength  $\sigma_{ci}$  and the constant  $m_i$  are representative of the intact rock in the blocks of the rock mass. In fact, this assumption is not always valid since in many rock masses, defects such as veins, micro-fractures and weathered or altered components can reduce the intact rock strength. Ideally, tests should be carried out on specimens large enough to include representative sections containing these defects, but collection and preparation of such specimens can be challenging”. As a comment, for a well-connected fracture network, rock bridge strength and rock block strength can be considered equivalents. Therefore, for a rock matrix with an important strength upscaling effect, as the case of the defected leached granodiorite presented here, rock block strength must be considered to characterize rock mass strength.

Chapter 5 address the importance of consider strength upscaling in stability assessment by means of the back analysis of an inter-ramp slope failure in an open pit mine, where the intact rock corresponds to the leached defected granodiorite already assessed.

## **Chapter 5. Upscaled strength of the defected rock and its application in the back analysis of a slope failure**

In this chapter, back analysis of a slope failure is used to assess the suitability of numerically upscaled rock strength properties to correctly reproduce the instability. A comparison was made between a base case, assessing the slope stability using non-upscaled laboratory strength properties, and the stability analysis using the numerically upscaled properties. The slope failure involves the geological unit Heterogeneous Leached Zone (HELZ, introduced in Chapter 3), through which intact rock strength was numerically upscaled in Chapter 4 to obtain rock block strength. Thus, in this back analysis converges the field data together with the numerical investigation on size - strength dependency, highlighting the importance of the strength upscaling effect in the design and stability assessment of large excavations.

The bidimensional stability analysis was performed using two types of numerical tools, continuum method in RS2 software (Rocscience, 2019) and hybrid FDEM method in ELFEN software (Rockfield, 2013). Comparison of slope stability analysis using non-upscaled and upscaled intact rock properties are presented. Results are concordant between methods and show that upscaled properties are suited to reproduce the massive slope failure without excessively weakening the rock mass. Confined strength, assessed by analyzing H&B's  $m_i$  and friction angle, shown to be of prime importance in the stability analysis.

### **5.1 Description of the slope failure**

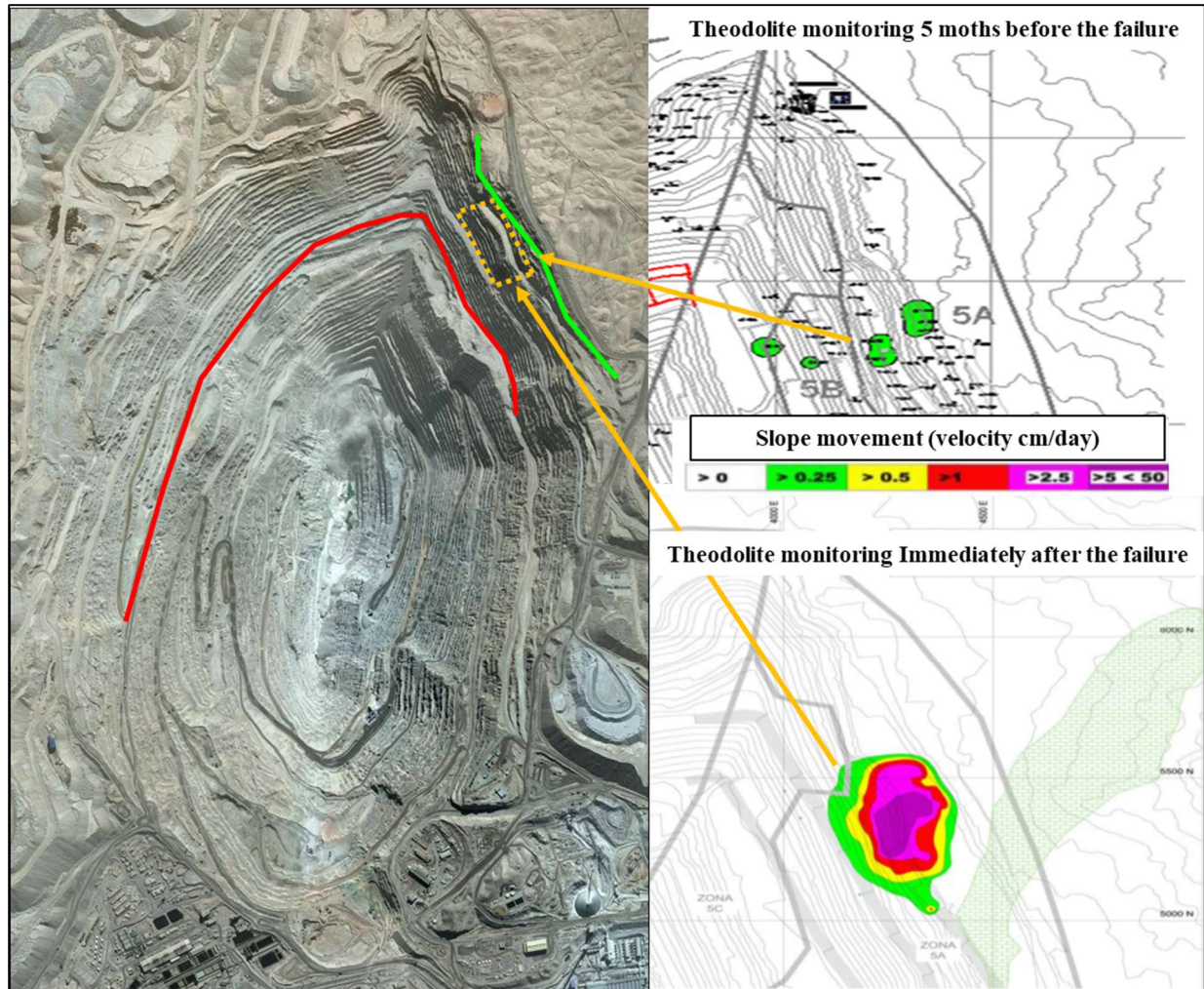
As shown in Chapter 3, the defected Leached Granodiorite corresponds to the rock matrix of a geological unit named Heterogeneous Leached Zone (HELZ). An inter-ramp slope failure of approx. 2 Mton and 170 m high occurred in this unit associated with the early mining activity of a new pushback in Chuquicamata open pit mine (**Figure 5.1**). This instability was back analyzed using upscaled rock matrix strength as input.



**Figure 5.1.** Inter-ramp slope failure on which back analysis was performed. The rupture extends approximately from 3000 meters above sea level (m.a.s.l.) down to 2830 m.a.s.l. A pushback was located on top of the failed rock mass and 180 m below the toe of the breakage. A shovel is shown as scale reference.

Due to the comprehensive geotechnical instrumentation and continuous monitoring with robotic theodolite and georadar, the slope movements were detected and followed 5 months before the occurrence of the massive slide (**Figure 5.2**). Evacuation protocols were applied several hours before the event, which culminated with no material losses or damage to workers in place. The use of state-of-the-art monitoring technology, in addition to the size of the pit (4 kms long x 2 kms wide), allowed mine areas not affected by the failure to remain operative during the event. The early detection of slope deformation lead to an intensive campaign of geological and geotechnical characterization using drillholes. The information collected from these drillholes, in addition to bench mapping performed as constant practice in Chuquicamata mine, are the sources of the data presented in this research.





**Figure 5.2. Contouring of slope velocity at early stage of deformation (5 months before the event) and after the failure. Nearest pushbacks showed in green and red in pit photograph. The pit is 4 kms long by 2 kms wide. Slope velocities monitored with robotic theodolite.**

## 5.2 Geological setting

The geology of the 2d vertical section used for the back analysis of the failure was based on information from bench mapping and drillhole site investigation. The open pit mine is located in a highly faulted terrain as a product of its tectonic history. Several major faults, in which continuity was verified in drillholes and bench mapping, were included in the section. A DFN model was built for less continuous, non-implicitly modellable faults, which importance lies in including in the analysis the potential anisotropy linked to faults systems.

### 5.2.1 Geological units

The slope failure occurred associated with the Heterogeneous Leached Zone (HELZ), a unit that is surrounded by the Homogeneous Leached Zone (HOLZ). As described in Chapter 3, both units correspond to a granodiorite affected by supergene alteration. The term “leached” refers to the supergene process of the percolation of meteoric waters and its acidification, which in turn washed down the primary copper ore and partially altered the host granodiorite. The product of this process was the deposition of secondary minerals: iron oxides, iron hydroxides, gypsum and oxidized copper ore in fractures and defects in the leached granodiorite. Both leached units, HELZ and HOLZ, are geologically similar and were differentiated based in the degree of supergene alteration, i.e. the degree of leaching. The HELZ showed the higher degree of alteration and lower geotechnical quality, with more abundant secondary oxides and gypsum and was much more fractured than the HOLZ. The leached geological units were in contact with a Granodiorite with Chloritic and marginal Sericitic alteration of better geotechnical quality, which did not participate in the slope failure. A Metasedimentary rock was in contact with the leached units. This contact was mainly intrusive and by fault to a lesser extent. The Metasedimentary rock did not participate in the slope failure (**Figure 5.3**).

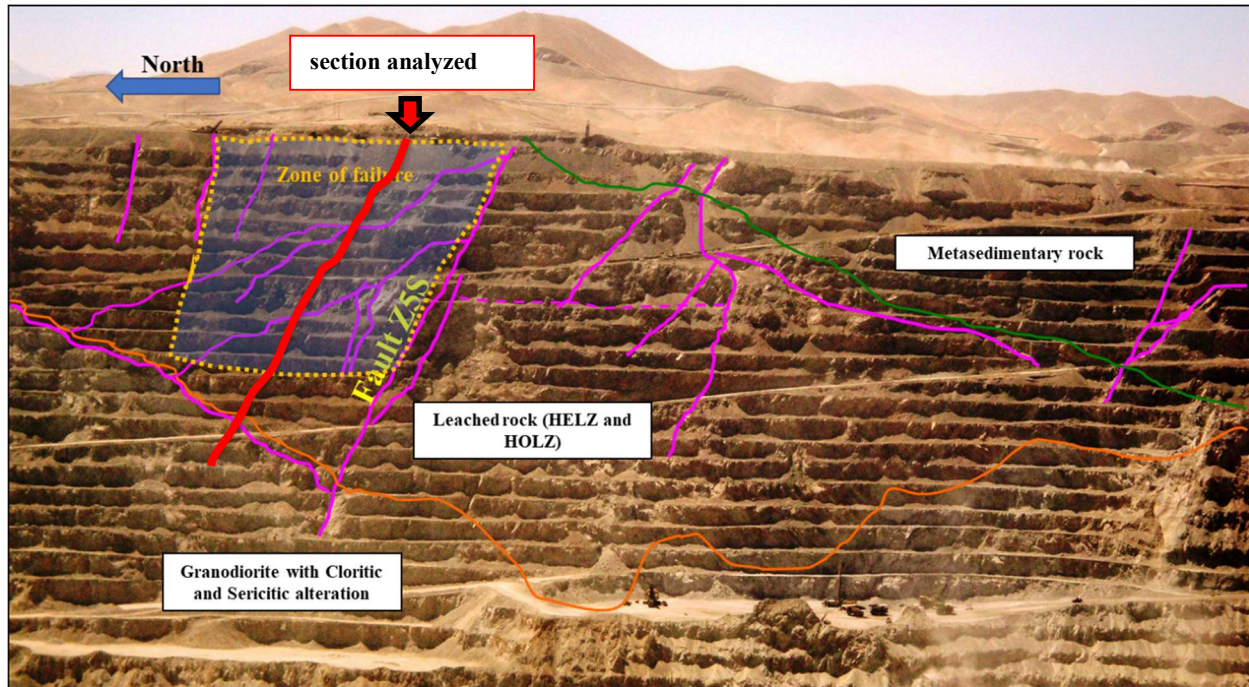
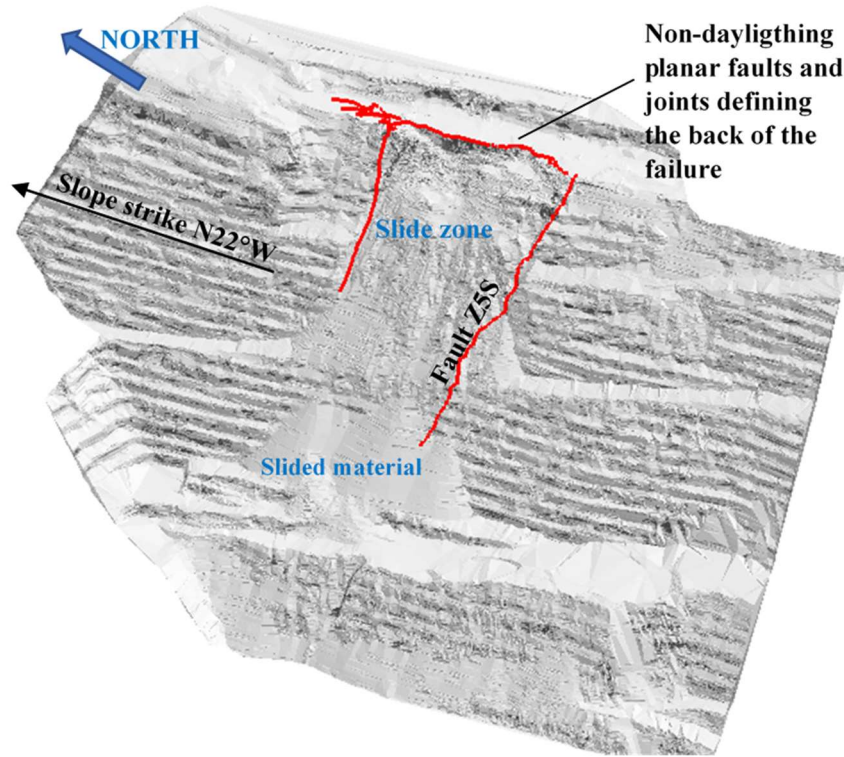


Figure 5.3. Geological units and main faults outcropping in the failed slope. HELZ and HOLZ units not differentiated. Red line indicating the position of the 2d section analyzed in RS2 and ELFEN software.

### 5.2.2 Structural Geology

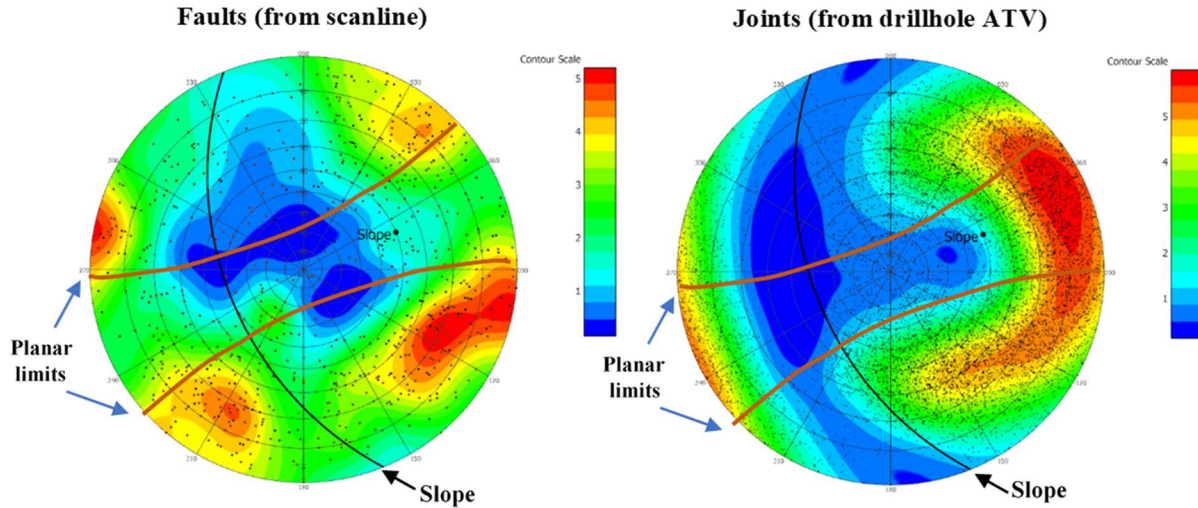
The slope failure was partially controlled by faults and joints pertaining to the main structural sets in the area. Non-daylighting planar faults and joints of azimuth NW delimited the back of the slide. The slide was delimited by fault Z5S in the south, while in the north the limit was a combination of less continuous faults, joints and rock bridges. The rupture in the lower part of the failure occurred mainly throughout the rock mass (**Figure 5.4**).





**Figure 5.4.** Laser topography of the slope failure. Structural limits of the slide in red. Fault Z5S is a continuous structure while the back and north bound of the failure are formed by the combination of faults, joints and breakage of rock bridges.

Planar structures were the most important discontinuities in the area, with planar faults and joints controlling bench scale instabilities in the past. Thus, it is quite likely that discontinuities introduced anisotropy in the mechanical behavior of the rock mass, potentially playing an important role in the slope failure. In addition to planar structures, faults and joints with toppling geometry in the slope could accommodate the deformation of the rock mass as well. Although faults with planar and toppling geometry are not prominent as a structural set in scanline mapping (**Figure 5.5**), their relationship with the slide was verified in the exposure of the back limit of the slide. ATV register of drillholes shown clearly non-daylight planar joints and toppling. Since joint ATV orientations came mainly from drillholes dipping east, a blind zone is generated in joints stereonet in **Figure 5.5** (dark blue zone).



**Figure 5.5. Stereonet of faults (VIF+FT) and joints. Planar limits for a parallelism criterion of  $\pm 20^\circ$ . Joints orientations sourced from ATV of drillholes in the HELZ unit (assuming rank 1-2 as joints). For faults, two structural sets are located at the border of planar limits, although there are no clear planar sets there are faults located within the planar limits ( $20^\circ$ ).**

Given the importance of accounting for potential anisotropies introduced by structures, faults DFN models were built in Fracman software (Golder, 2019) for both categories of structures VIF and FT. These traces were included in the analyzed cross section in ELFEN. Due to the bias in the ATV register of joints, they were not included implicitly in the section analyzed. In addition, the high intensity of joints makes it quite difficult to accommodate a mesh with the appropriate quality in ELFEN software. Finally, it was assumed that faults DFN suffice to represent the potential anisotropy.

### 5.3 Discrete Fracture Network of faults

The source of information for the DFN model was bench mapping performed in HELZ unit, collected in the slope excavated after the slope failure. As presented in Chapter 3, in the available bench mapping information, structures are classified in 3 categories based on continuity and width: Very Important Faults (VIF), Fault Traces (FT) and Joints. VIF and FT faults DFNs were modelled independently, while joints were included implicitly using GSI and H&B properties for geological units. **Table 5.1** shows the input parameters for DFN modelling of faults.

**Table 5.1. Input parameters for faults DFN (SD=Standard Deviation)**

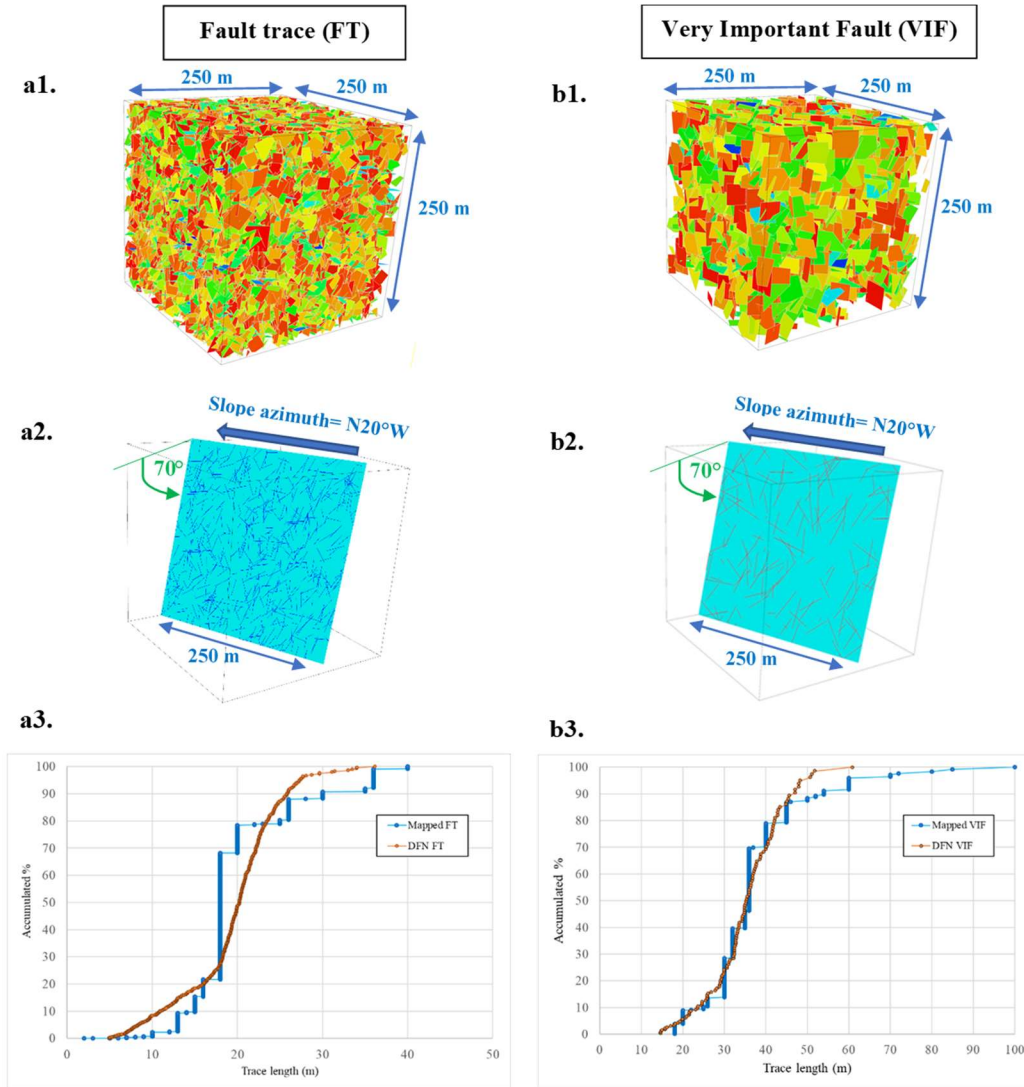
Parameter	Source of information	Method	Values	
			VIF	FT
<b>Orientation</b>	Bench mapping (scanline)	Bootstrap	--	--
<b>Intensity (#/m)</b>		Simulation method	$P32=1.5 \cdot P10 + 0.024$ Scanline Mean $P10=0.05$ $P32=0.098$	$P32=1.4 \cdot P10 + 0.036$ Scanline Mean $P10=0.11$ $P32=0.19$
<b>Equivalent radius (m)</b>		Distribution fitted to bench mapping data	Normal distribution, Mean=15.1 m, SD =2	Lognormal dist., Mean=8.8 m, SD =2.1
<b>Quantity of information</b>		--	Total length of scanlines = 4620 m Data points= 231	Total length of scanlines = 6645 m Data points= 731

Forward modelling method was applied to convert linear intensity P10 to volumetric intensity P32 (Elmo, 2006). A DFN realization was generated for the mean intensity of VIF and FT. It can be noted that P10 intensity is very low both for VIF and FT, with approximately one fault every 10 meters.

For size distribution, although a more comprehensive Power Law size distribution is preferable when discontinuities are categorized, the available information showed a poor fitting to it, hence size distribution was fitted independently to VIF and FT bench mapping data. Based on bench mapping, a minimum equivalent radius of 15 m was used for VIF and 5 m for FT.

### 5.3.1 Faults DFN model validation

All bench mapping was captured along horizontal scanlines with an orientation of N20°W, the same as the orientation of the slope. Therefore, to validate faults DFN the realization was sampled with a traceplane oriented as the slope and with a dip of 70°, equal to the bench face inclination (Figure 5.6).



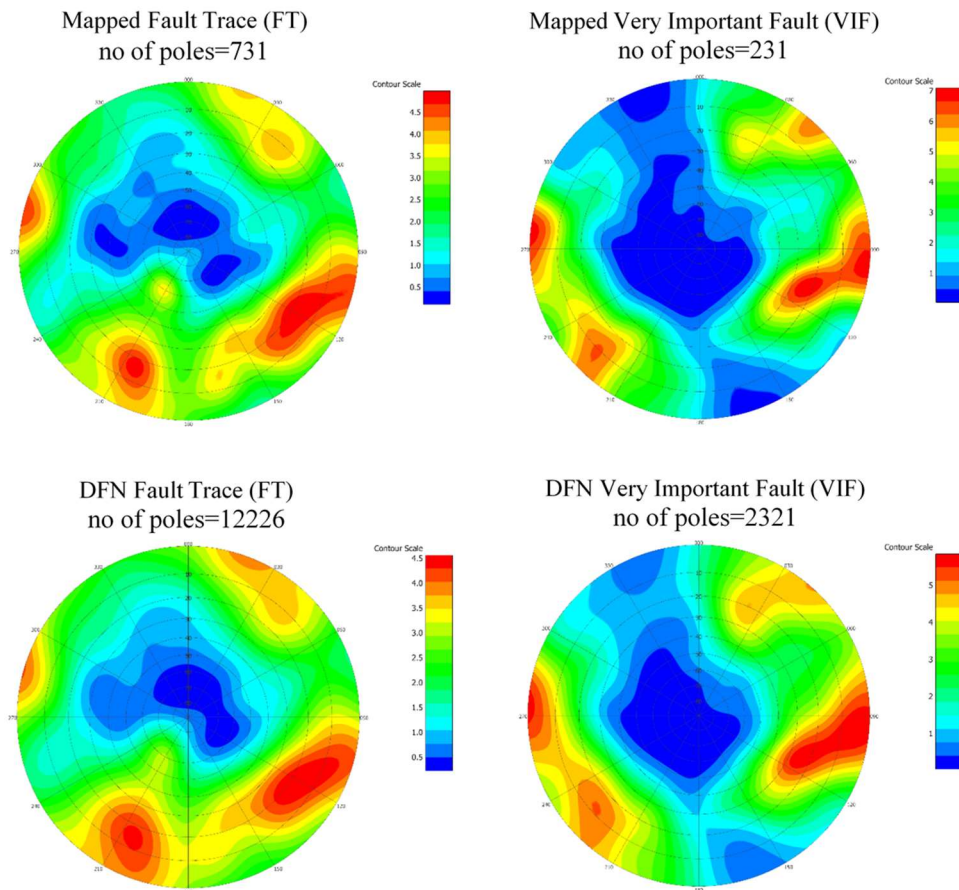
**Figure 5.6. Validation of DFN's traces length distribution. a1, b1 VIF and FT realizations were generated in a 250 m side cube. a2, b2 each realization was sampled with a trace plane with same slope orientation (azimuth=N20°W, dip=70°). a3, b3, comparison of the trace length distribution of simulated faults (brown) and mapped faults along scanlines(blue).**

There is good agreement between DFN faults and mapped faults traces. The stepped shape of mapped fault length in figure 5 is due to faults traces cannot be measured directly; their length is estimated considering the bench height as reference, and thus trace length estimation tends to be concentrated around certain values. This is evident for FT faults, where almost 50% of the cumulative distribution has a trace length of 18 meters, which is in fact the bench height for this slope. For FT, the DFN median trace length is 20 m which compares with 18 m mapped median

length. For VIF the DFN trace length and mapped trace length median are coincident and equal to 36 m.

Validation of intensity was carried out by simulating the scanline sampling with five horizontal drillholes. Each simulated drillhole was 150 m length each and the same orientation of the slope. The average intensity P10 yielded by simulated drillholes was equal to  $0.127 \text{ m}^{-1}$  for FT and  $0.054 \text{ m}^{-1}$  for VIF, which compares reasonably well with mapped P10 of  $0.11 \text{ m}^{-1}$  for FT and  $0.05 \text{ m}^{-1}$  for VIF showed in **Table 5.1**.

Mapped orientation vs DFN orientation for both VIF and FT shows a good agreement (**Figure 5.7**)



**Figure 5.7. Stereonets comparison of mapped and DFN generated faults.**



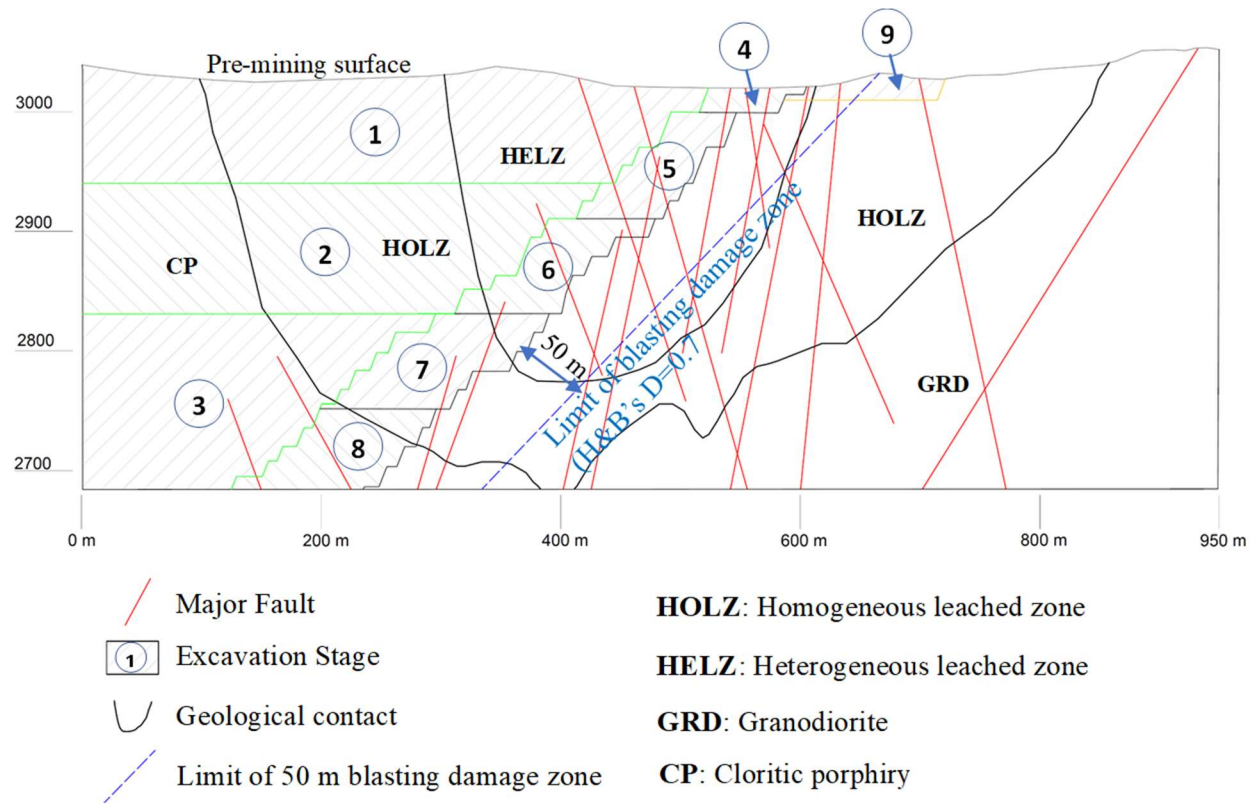
## 5.4 Model settings

### 5.4.1 Section geometry and excavation stages

Pit topography, Geological contacts, blast damage zone and main major faults were included in the 2D section analyzed in RS2 and ELFEN software, the latter additionally included VIF+FT faults DFN.

Hoek et al. (2002) introduced the blast damage D factor to generalized H&B's failure criterion to account for the effect of blasting in the excavated rock mass. Previous experience in Chuquicamata open pit mine suggest a 50 m zone of blast damage with a D factor equal to 0.7 (**Figure 5.8**). This practice was included in the analysis presented here.

Nine excavation stages were set up; the first three stages correspond to the removal of the central part of the pit and are not related to a specific period of time. Stages 4 to 8 correspond each to the excavation performed in one-year time, while stage 9, located at the top of the slide, and corresponds to the 3 months of excavation done before the failure. The constitutive models used in RS2 and ELFEN simulations, H&B and M-C respectively, are not time dependent, thus the stability of the slope is related to the stress field and its change in response to modifications of the geometry. Therefore, one of the aims of a staged excavation of the slope is to allow gradual change in the stress field, maintaining the condition of quasi equilibrium. **Figure 5.8** shows the 2d section, major structures, geological contacts and excavation stages used in the stability analysis.



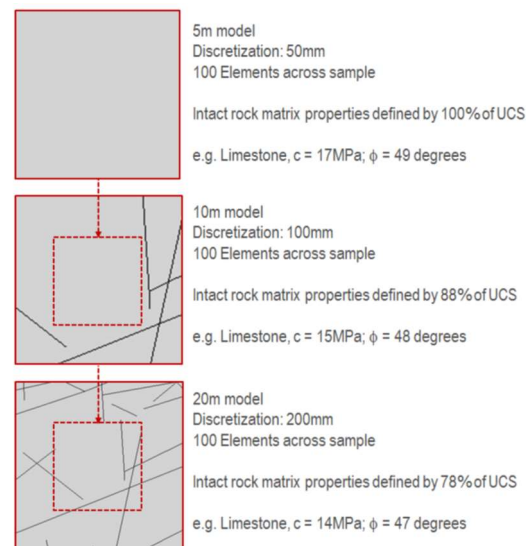
**Figure 5.8.** Geometry of the vertical cross section assessed in RS2 and Elfen software. Sequence of excavation stages indicated in circled number. Meters above sea level are indicated at the left.

#### 5.4.2 Intact rock and rock mass input properties

The rock mass of the geological units involved in the analysis was characterized using the H&B failure criteria and the GSI parameter (Hoek and Brown, 2018). The numerical simulations were performed to assess the suitability of numerically upscaled intact rock properties and laboratory intact rock properties to reproduce the failure in the HELZ unit. Laboratory intact rock properties were used to set up the base-case scenario, recreating a numerical analysis where upscaled properties are not available, which probably is the most common situation. Thus, base-case UCS was set equal to the average unconfined strength of mixed rupture laboratory test (30 MPa) of 61 mm diameter samples. Use of mixed rupture test UCS is a relatively common practice in industry when defects are relevant and need to be incorporated in the analysis (Russo and Hormazabal, 2016). As can be expected, confined strength of biaxial test with mixed rupture showed a high dispersion, therefore, the obtention of H&B's  $m_i$  for rock with defects was not possible. This

parameter ( $m_i$ ) was set equal to the value obtained from biaxial test with rupture trough matrix ( $m_i=11.3$ ). Although this assumption neglects the increase of dilation due to defects, it is a possible election when reliable data is not available, and it can be interpreted as a conservative approach. Actual laboratory test of defected/veined rocks show an increase of confined strength regarding its non-defected rock matrix (Bewick et al, 2018), which expression is higher H&B's  $m_i$  constant value. Young modulus and Poisson ratio were sourced, for non-upscaled intact rock base-case, from non-defected rock matrix laboratory. Numerically upscaled intact rock properties were obtained from ELFEN SRM samples presented in Chapter 4.

For the units not involved in the failure, given that the zone of failure is known, intact rock laboratory properties were not upscaled. For FDEM models, Elmo and Stead (2010) propose the procedure showed in **Figure 5.9**. This method is aimed at accounting for rock matrix strength decreasing when mesh size increases, assuming a  $k$  constant (equation 4, Chapter 4) equal to 0.18 as suggested by Hoek and Brown (1981). From the laboratory test data compiled by Yoshinaka et al (2008), it can be deduced that  $k$  upscaling constant is specific for each rock type. Therefore, a  $k=0.18$  can be considered as an estimation when no further information is available. The  $k$  upscaling constant value should be used/chosen carefully when the behavior of the rock mass under study is not well established.



**Figure 5.9. Example of upscaling approach in function of mesh size elements as proposed by Elmo and Stead (2010).**

There are no implicit joints used in the analysis, therefore intact rock properties must be first converted to equivalent continuum rock mass properties to be used in the slope stability analysis. To fully characterize rock mass strength using H&B failure criteria, UCS,  $m_i$  and GSI are needed. While UCS and  $m_i$  correspond to intact rock properties, GSI is incorporated to address the two main factors influencing the rock mass mechanical properties: blockiness and joint condition (Hoek and Brown, 2018). For the units not involved in the failure, GSI was sourced from bench mapping, while for HELZ, the unit enclosing the failure, GSI was obtained from a combination of bench mapping and drillhole characterization. Drillhole data showed that bench mapped GSI was not always appropriate to capture the blockosity in the HELZ unit.

While H&B's failure criterion is available in RS2 software, that option is not present in ELFEN code; therefore, H&B rock mass envelope must be linearized to be converted to M-C properties. This was done using Rocdata software (Rocscience, 2017), where M-C's cohesion and friction angle were calculated for a  $\sigma_3$  maximum corresponding to a 200 m slope. Tensile strength cutoff was set equal to the tensile strength obtained from the H&B rock mass envelope. Rock mass Young modulus was calculated using the empirical equation of Hoek and Diederichs (2006). **Table 5.2** shows the intact rock and rock mass input parameters used in the 2d analysis, where “numerically upscaled” properties correspond to those obtained from SRM samples showed in chapter 4.

**Table 5.2. Input properties for 2d slope stability analysis. Rock mass friction angle and cohesion were obtained from the linearization of H&B criteria and applied to M-C properties in ELFEN code.**

Property		Heterogeneous Leached Zone (HELZ)		Homogeneous Leached Zone (HOLZ)	Cloritic Porphyry (CP)	Granodiorite (GRD)
		Base -case (Laboratory non-upscaled)	Numerically upscaled (SRM)			
<b>Intact rock</b>	Density (ton/m <sup>3</sup> )	2.5	2.5	2.5	2.6	2.6
	Young Modulus (GPa)	21.9	24	21.9	35	33.2
	Poisson ratio	0.27	0.35	0.27	0.25	0.23
	Uniaxial Compressive strength (MPa)	30	15	30	80	100
	Tensile strength (MPa)	4.5	1	4.5	9.3	10
	H&B's $m_i$	17.6	23	17.6	15	13.5
<b>Rock mass</b>	GSI average (min-max)	34 (20-50)	34 (20-50)	44 (20-70)	53 (37-70)	43 (33-53)
	Rock Mass Cohesion (MPa)*	0.84	0.82	1.01	1.92	1.68
	Rock Mass Friction Angle (°)*	37	32	40	46	44
	Rock Mass Tensile Strength (MPa)*	0.012	0.005	0.025	--	--
	Rock mass elastic modulus (Mpa)**	2321	2544	4897	12812	6499

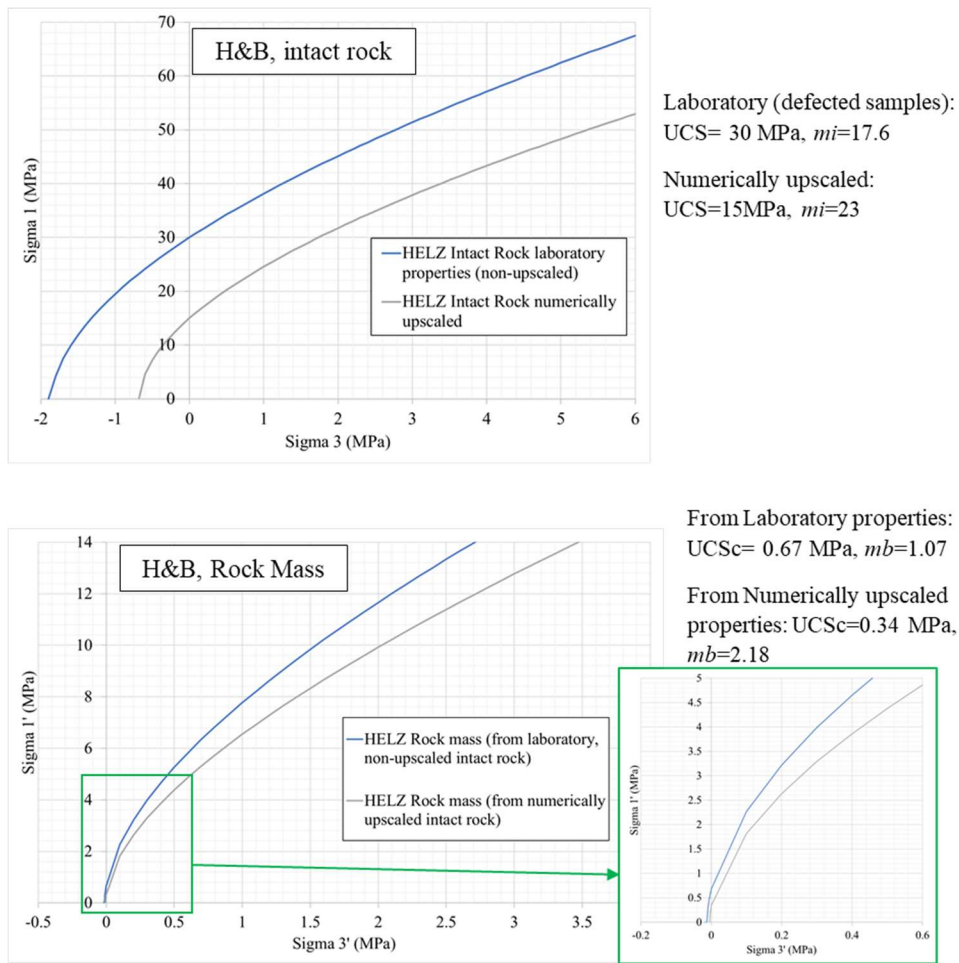
\* Obtained from the linearization of H&B's curve in Rocdata software (Rocscience, 2017).

\*\* Calculated using Hoek and Diederichs (2006).

Rock mass properties in Table 2 correspond to H&B's D factor equal to 0 (no blasting damage). Properties for units in the blast damage zone (**Figure 5.8**) were calculated in accordance with Hoek et al. (2002) for a D factor equal to 0.7. These properties are applied defining a different material

for the units in that zone. While RS2 software requires only the input of the D factor value to calculate the equivalent H&B's properties, in ELFEN software rock mass cohesion, friction angle and elastic modulus were calculated in Roclab software.

Laboratory and numerically upscaled UCS and  $m_i$  constant for HELZ unit in **Table 5.2** are contrasting. The numerically upscaled UCS=15 MPa is equivalent to only 50% the UCS of laboratory test, while numerically upscaled  $m_i$  is 1.3 times the laboratory  $m_i$  for defected samples. Both intact rock envelopes are in fact quite apart in the  $\sigma_1$ - $\sigma_3$  space. This difference of strength is still present but in a lesser extent for HELZ rock mass properties H&B's envelope (**Figure 5.10**).



**Figure 5.10. Hoek and Brown envelopes for Intact Rock (a) and Rock Mass (b) for HELZ unit. For intact rock envelopes, numerically upscaled properties depict a weaker rock (a). In the case of rock mass envelopes, unconfined strength difference is less marked due to low GSI, the increase in strength with confinement is higher for the rock mass based on non-upscaled laboratory properties of intact rock strength.**

For HELZ unit, intact rock UCS from laboratory and numerically upscaled can be classified as low strength. This low UCS, in combination with the low GSI (34), decreases the initial difference of intact rock UCS when scaled to rock mass UCS. In turn,  $m_i$  constant for laboratory intact rock properties is lower than the numerically upscaled intact properties. Thus, although the unconfined numerically upscaled intact rock is weaker, its confined strength increases more in comparison with the laboratory data. In general, the HELZ rock mass based in numerically upscaled strength is weaker than its analogues based on laboratory properties from defected samples.

### 5.4.3 Loadings

Only field stress is acting in the analyzed slope. Previous studies in Chuquicamata mine (Informe Proyecto aumento angulo talud, 2005) define the stress field for global slopes as follows: Vert Stress =  $0.0026 \cdot H$  (MPa); Horizontal Major stress (E-W) =  $1.13 \cdot \text{Vert Stress}$  (MPa); Minor Horizontal Stress (N-S) =  $0.7 \cdot \text{Vert. Stress}$  (MPa). This stress field is considered appropriate for the stability analysis presented here and was introduced in both FE and FDEM codes. This stress field is not necessarily applicable to deeper zones of the mine or to the underground mine under development.

## 5.5 Bidimensional numerical modelling of the failure

### 5.5.1 Slope failure back-analysis in finite element continuum code RS2

The low GSI value (GSI=34) depicts a well-connected fracture network in the HELZ unit. Consequently, the rock mass, at slope scale, can be considered continuum enough to be fairly simulated using a finite element (FE) code. Both sets of properties, base-case laboratory non-upscaled and numerically fully upscaled (**Table 5.2**), were used to simulate the failure of the HELZ unit in the 2D analysis performed in RS2 FE program (Rocscience, 2019). Rock mass properties were set using generalized H&B's failure criterion. Plastic material type was used for all units. Residual properties were set equal to initial properties. On site investigation showed that water level was located below the failure surface, thus, no water pressure was set in both 2D analysis (RS2 and ELFEN). All major faults modelled from drillholes were included in the geometry analyzed.

For both sets of properties, based on laboratory test on defected samples and numerically upscaled, the extension of the failure is quite similar when maximum shear plastic strain is examined (**Figure 15.11**). The back of the simulated failure agrees with field observations in both cases, occurring associated to the same major fault that limited the back of the failure in reality. In the lower part of the slope the actual rupture occurred approximately at the level 2830, which compares with level 2790 in both RS2 simulations. Thus, there is an overestimation of 40 m in the simulated failure extension. The failure surface is completely enclosed in the HELZ unit. The Strength Reduction Factor (SRF) is equal to 1.1 for non-upscaled properties (from laboratory) and equal to 1 for numerically upscaled properties. In rigorous terms, the failure is replicated only when upscaled properties are used (SRF=1), but an extra factor of 20% -30% (SRF 1.2 – 1.3) is considered in practical stability assessment to account for uncertainties in the input variables. Displacements are of the same order of magnitude with a maximum absolute horizontal displacement of approximately 0.5 m (**Figure 5.12**).

From **Figure 5.11** and **5.12** it can be asserted that the limit of the 50 m zone where blast damage D factor is applied acts as a hard limit, and the failure is conditioned to this blasting damage zone. When D was set equal to 0 in a test model, meaning no blasting damage, the failure extension was not reproduced, showing sliding in the upper part of the slope only. Certainly D=0 is an unlikely condition for blasts of the order of hundreds of thousands of tons, as in the Chuquicamata case, and probably the blast damage factor D aids to account for other factors not included in the equation, for instance deconfinement. It is probable that the actual blasting damage zone can be described as a gradation from high damage at slope surface to an in situ rock mass conditions at certain (unknown) depth. Back analysis performed on other instabilities in Chuquicamata mine (not part of this study) showed 50 m and D=0.7 as suitable to reproduce the failures. In the same manner, Rose et al (2018) study the rock mass disturbance in open pit slopes, assigning the fully disturbed limit to a depth of approx. 50 m for a 450 m slope height. The importance of H&B's D factor for the stability analysis is acknowledged here, but its investigation is out of the scope of this research; the D zone based on previous back analysis was adopted in the current stability examination.



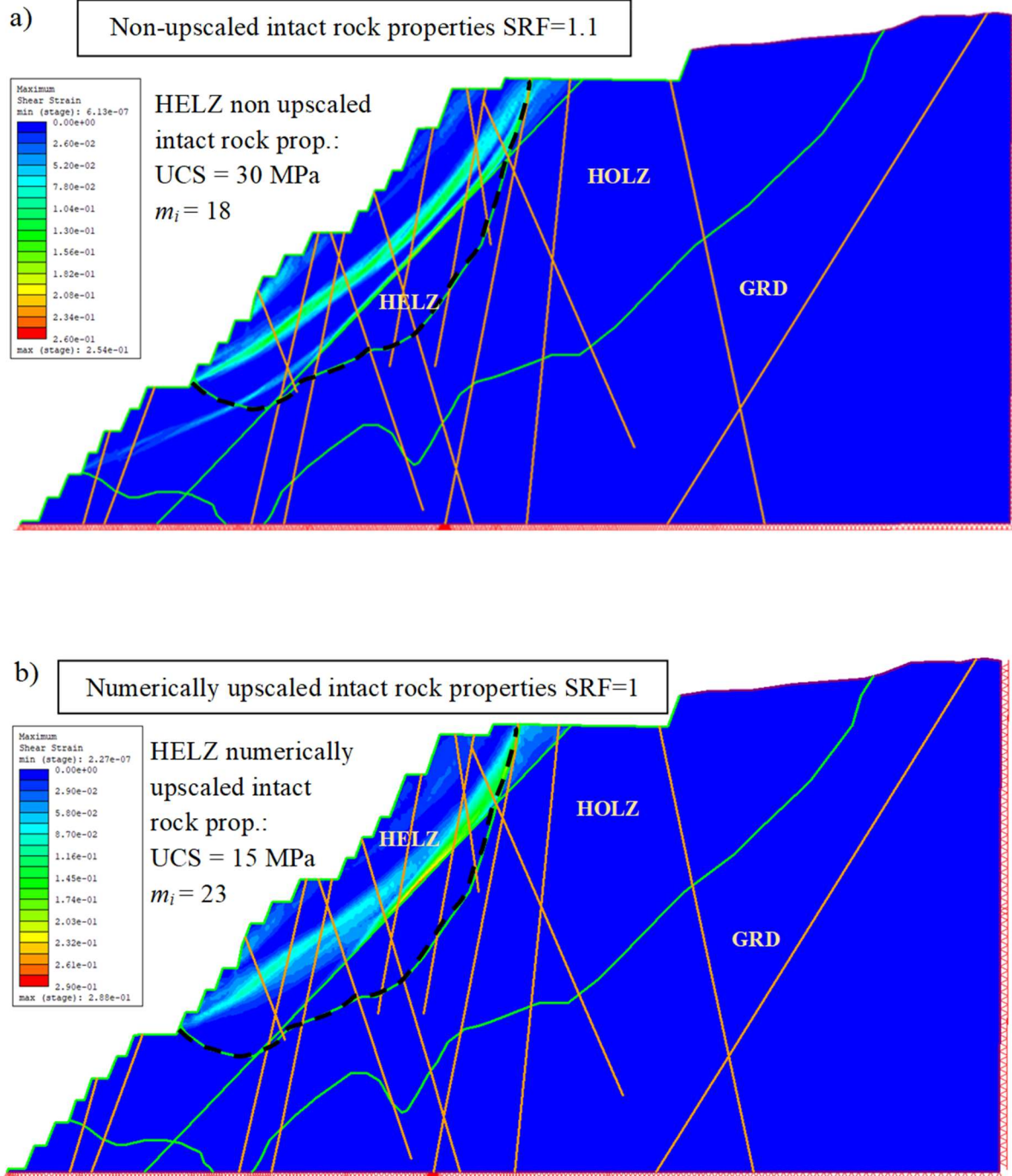


Figure 5.11. Bidimensional stability analysis in RS2 FE code showing maximum shear strain for non-upscaled intact rock properties (a) and numerically upscaled intact rock properties (b). In both cases the extension of the failure and shape is quite similar and consistent with field observations. Black dotted line marks HELZ limit. HELZ: Heterogeneous Leached Zone; HOLZ: Homogeneous Leached Zone; GRD: Granodiorite. Major implicit faults in pink

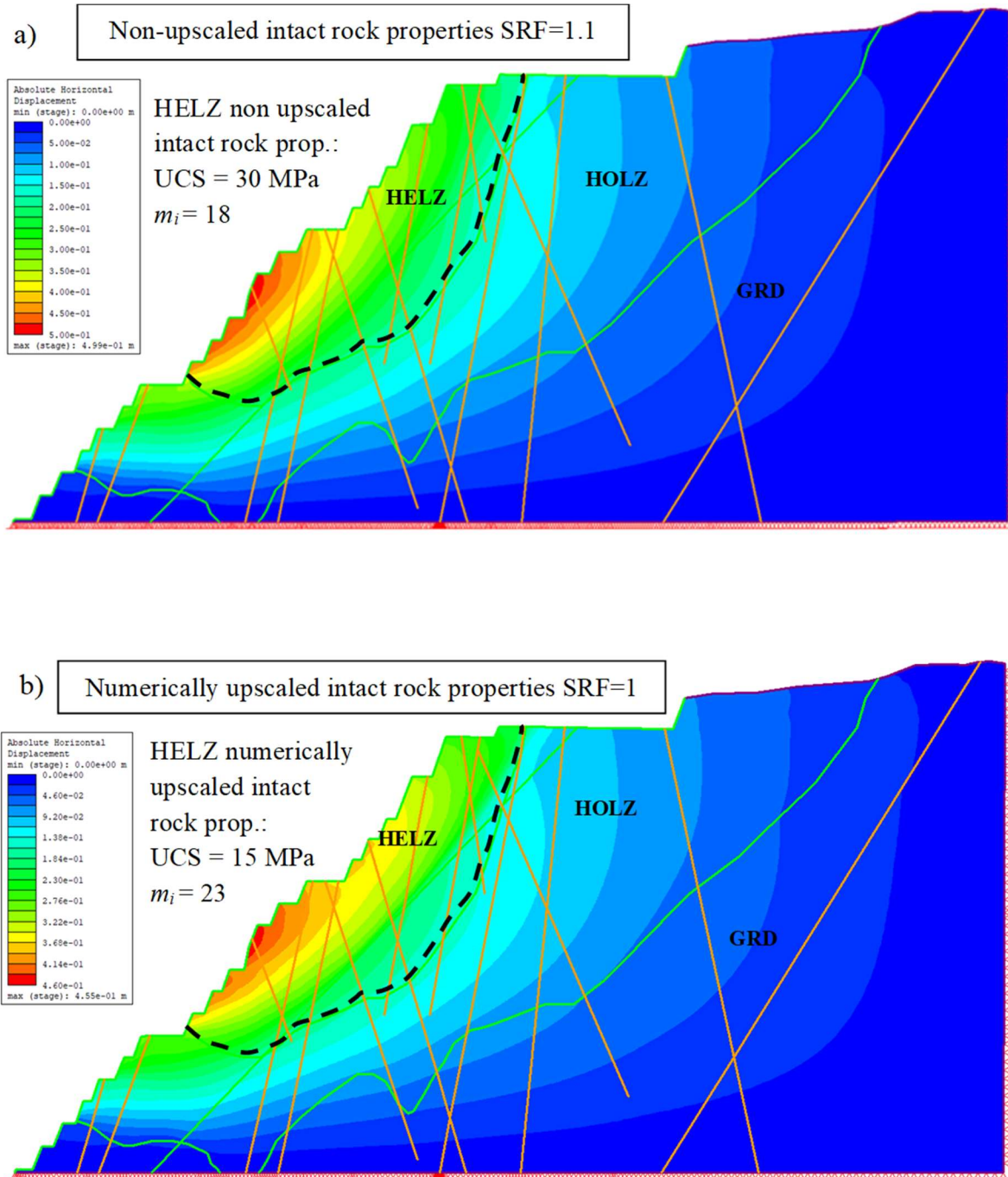


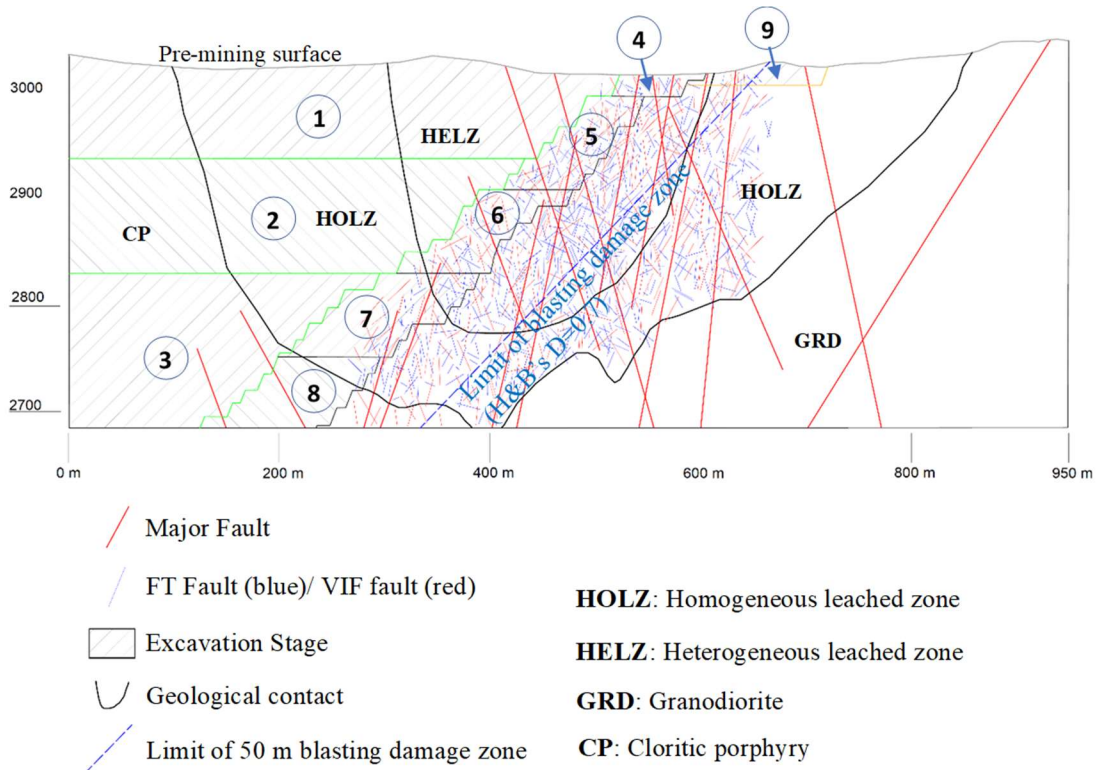
Figure 5.12. Bidimensional stability analysis in RS2 FE code showing absolute horizontal displacement for non-upscaled intact rock properties (a) and numerically upscaled intact rock properties (b). As expected, due to similar H&B's rock mass envelopes, displacement is alike between both cases. The zone of major displacement is concordant with the actual failure. Maximum horizontal displacement is approx. 0.5 m. Black dotted line marks HELZ limit. HELZ: Heterogeneous Leached Zone; HOLZ: Homogeneous Leached Zone; GRD: Granodiorite.

Both cases analyzed in RS2 yield quite a similar surface of failure and horizontal displacement. However, SRF indicates that the failure was reproduced when the numerically upscaled properties were used. The simulated failure is concordant with field observations, although the rupture's toe is located approximately 40 meters below the actual rupture. The 50 meters blasting damage zone conditions the failure. Due to the origin of this criteria on other back analysis in Chuquicamata mine, and analysis performed in other mines (Rose et al 2018), the extension of the blasting damage zone was considered acceptable. It is acknowledged that the modelling of the blasting damage zone can be improved by reducing the D factor gradually over the extension of the zone.

### **5.5.2 Slope failure back-analysis in FDEM code ELFEN**

Due to its hybrid functionality from continuum to discontinuum, ELFEN code offer advantages to evaluate the influence of preexisting discontinuities during the failure. Therefore, with the aim of accounting for possible anisotropy induced by the less continuous faults, the DFN of faults described in section 5.3 was added to the bidimensional model. Due to the low intensity of VIF + FT faults DFN ( $P_{10}=0.16 \text{ m}^{-1}$ ) the addition of these faults does not need to be accounted for in the equivalent continuum properties for the rock mass. Numerical investigation on SRM samples performed by Farahmand (2017) shows the REV size for a moderately fractured rock mass to be approximately 7 meters, which is approximately the spacing of VIF + FT faults.

Excavation stages, geological contacts and major faults were kept unchanged from the section assessed in RS2 software. Excavation stages 1 to 8 and Granodiorite unit (GRD) were set as elastic materials. Excavation stage 9 and non-excavated part of the units HELZ and HOLZ were set as plastic materials. Fracturing was allowed in all plastic units. A triangular unstructured mesh was used with element size decreasing towards the zone of failure, namely: 5 m in the CP and GRD units, 3 m elements for HOLZ and excavation stages 4 to 8, and 1 m element size for the failed unit HELZ. **Figure 5.13** shows the 2D cross section assessed in ELFEN software.



**Figure 5.13.** Vertical cross section assessed in ELFEN software. Sequence of excavation stages indicated in circled number. Meters above sea level are indicated at the left. Thin blue and red traces correspond to DFN of VIF (red) and FT (blue faults).

Analogously to the analysis performed in RS2 software, two cases for HELZ rock mass strength were analyzed in ELFEN: rock mass strength based on non-upscaled intact rock and numerically upscaled intact rock properties. The slope stability and extension of failure were evaluated based on slope displacements. A minimum horizontal displacement's threshold of 0.2 m showed a good agreement with slope zones with crack development. Portions of the slope showing block detachment and unraveling agree with total horizontal displacement of approximately 0.7 m, quantity that was considered as failure limit for results analysis. The simulation reproduces the failure fairly well in both cases. **Figure 5.14** shows the stability analysis in ELFEN for both sets of properties. In agreement with field observations, the zone of interpreted failure is fully enclosed in the HELTZ unit. The case based on non-upscaled intact rock properties yielded a failure of slightly bigger extension than the real failure (**Figure 5.14a**). The extension of the failure based on numerically upscaled properties, agrees perfectly with the real rupture (**Figure 5.14b**) and is deeper than the failure based on non-upscaled laboratory test.



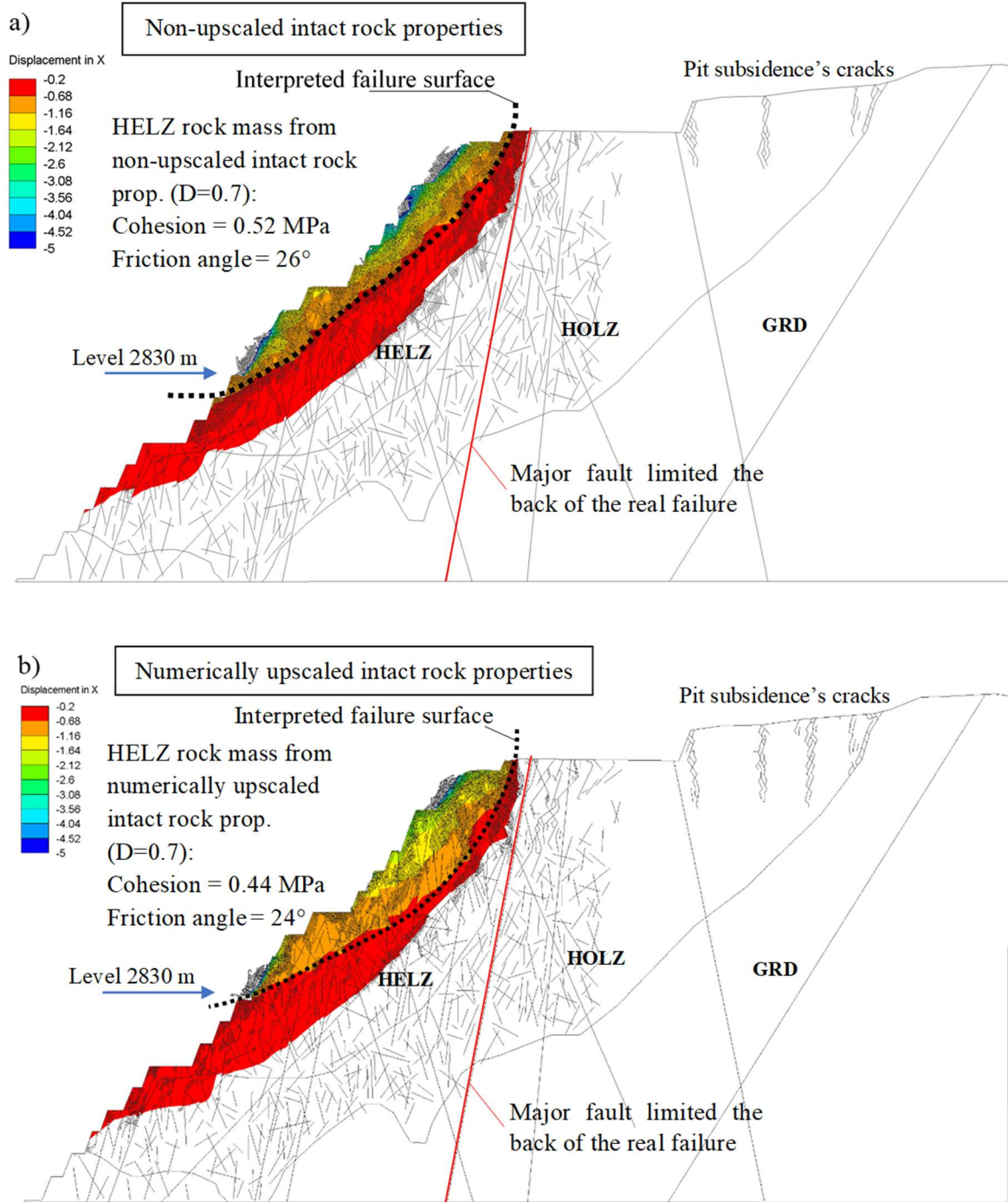


Figure 5.14. Bidimensional failure back analysis in ELFE code showing horizontal displacement for simulation using rock mass properties based on non-upscaled intact rock properties (a) and numerically upscaled intact rock properties (b) for HELZ unit. Interpreted failure surface for 0.7 m horizontal displacement is shown with black dotted line. Major fault limiting the back of the failure in red. Level 2830 correspond to the toe of the real failure.

None of the cases analyzed exactly replicates both limits observed in the field for the actual slide, namely the major fault that limited the back of the failure and level 2830 for failure toe (**Figure 5.14**).

There is development of new cracks from the tips of minor VIF and FT faults, preferentially in those discontinuities parallel to the slope and those with the geometry of toppling. Therefore, minor faults with critical orientation promote the failure but it cannot be asserted that the DFN is a major driver of the mobilized zone.

In general terms, the development of new cracks in the failure zone is more profuse in the case based on non-upscaled intact rock properties. New cracks occurred not only in the zone of failure, they developed at the toe of the slope in the HOLZ unit, and in the upper part of the section, out of the excavation (**Figure 5.14**). These cracks located outside of the pit are concordant with cracks observed in the field; they are nonrelated to the failure and were interpreted, when found in Chuquicamata mine, as a consequence of subsidence due to pit excavation. Thus, ELFEN simulation apparently addressed this phenomenon as well.

As in RS2 simulation, the blasting damage zone appears as a conditioning factor for the failure in ELFEN simulation. Given that the failure cannot be reproduced without the application of H&B's D factor to rock mass properties, it is considered as licit practice for both analyses presented here.

The ELFEN simulation shows similar failure in both cases and it is in general concordant with reality. However, the extension of the failure and depth of the zone of movement point to the simulation based on numerically upscaled properties as being the most accurate.

The difference of UCS between laboratory defected samples and numerically upscaled samples is dramatically reduced in the H&B's rock mass envelope. On the contrary, confined strength is likely the factor of higher influence in the differences between the results of simulation based on both sets of properties. Thus, a sensitivity analysis was developed to assess the effect of the confined strength of intact rock in the simulation of the failure using different values of H&B's  $m_i$ .

### 5.5.3 Influence of intact rock confined strength on stability analysis

Sensitivity analysis was carried out on HELZ unit confined strength. The unconfined compressive strength (UCS) was kept constant and equal to the numerically upscaled strength (15 MPa), GSI was kept unchanged as well. To test different variations of confined strength, H&B's  $m_i$  value of the non-defected rock ( $m_i=11.3$ ) was taken as a base and increased to  $m_i*1.3$ ,  $m_i*1.5$ ,  $m_i*1.8$  and  $m_i*2$ . In this manner, the analysis is intended to test the effect of incremental degrees of confined strength of the intact rock. The analysis was performed in both RS2 and ELFEN software. While H&B's generalized failure criteria parameters can be introduced directly into RS2, they need to be converted to equivalent M-C rock mass strength parameters using Rocdata software. **Table 5.3** shows intact rock H&B's  $m_i$  values used in RS2 analysis and its equivalent friction angle for intact rock and rock mass, the latter was used in ELFEN simulations.

**Table 5.3. H&B's  $m_i$  and equivalent Rock mass Friction angle for sensitivity analysis performed on HELTZ unit confined strength. Base  $m_i$  value corresponds to the non-defected intact rock. Numerically upscaled  $m_i$  is equal to  $m_i*2$**

	H&B's $m_i$ value	Equivalent rock mass friction angle (D=0.7)
$m_i$ base value	11.3	19°
$m_i*1.3$	15	21°
$m_i*1.5$	18	22°
$m_i*1.8$	20	23°
$m_i*2.0$	23	24°

**Figure 5.15 and 5.16** show the results of the sensitivity analysis in RS2 and ELFEN respectively.

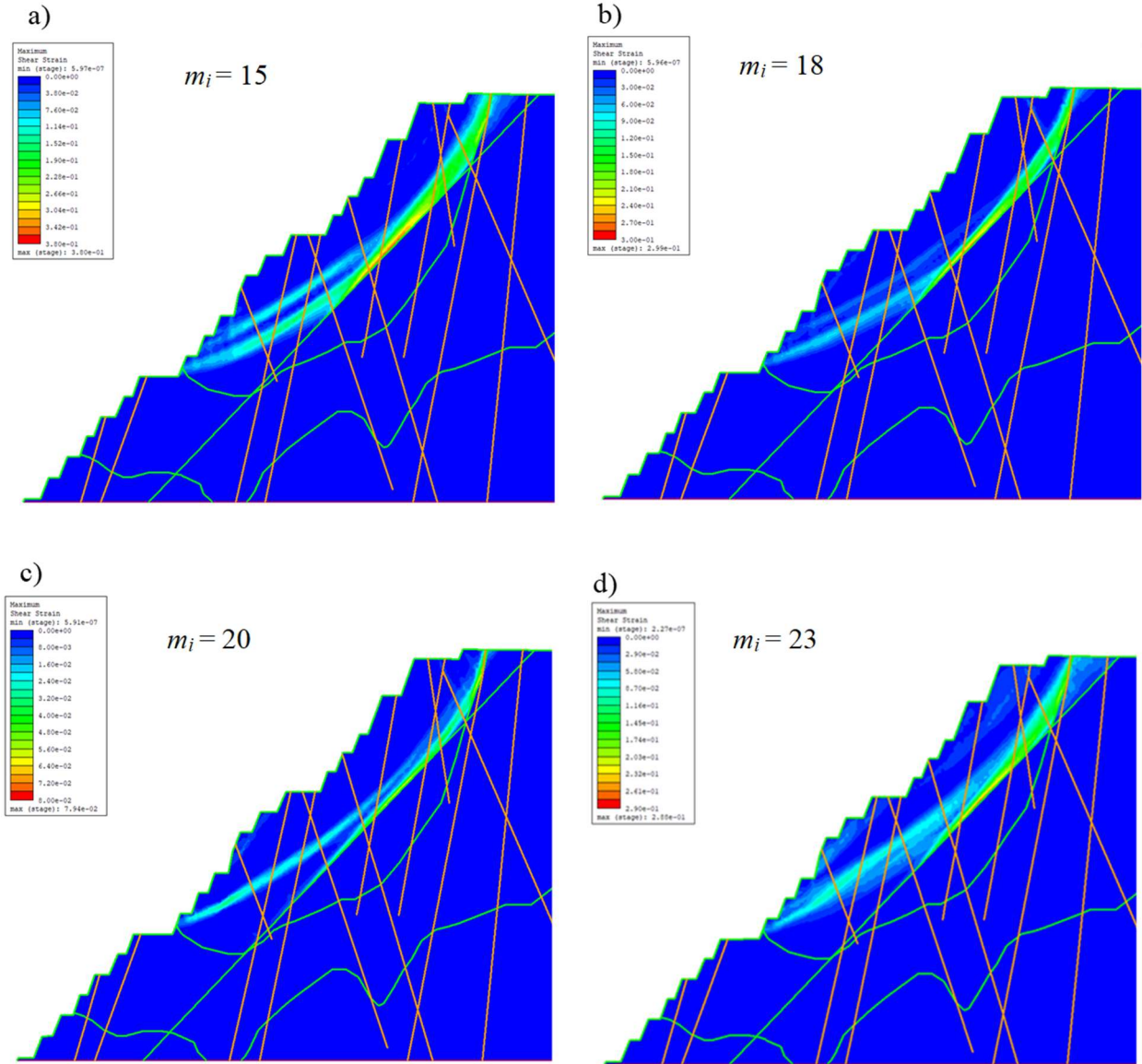
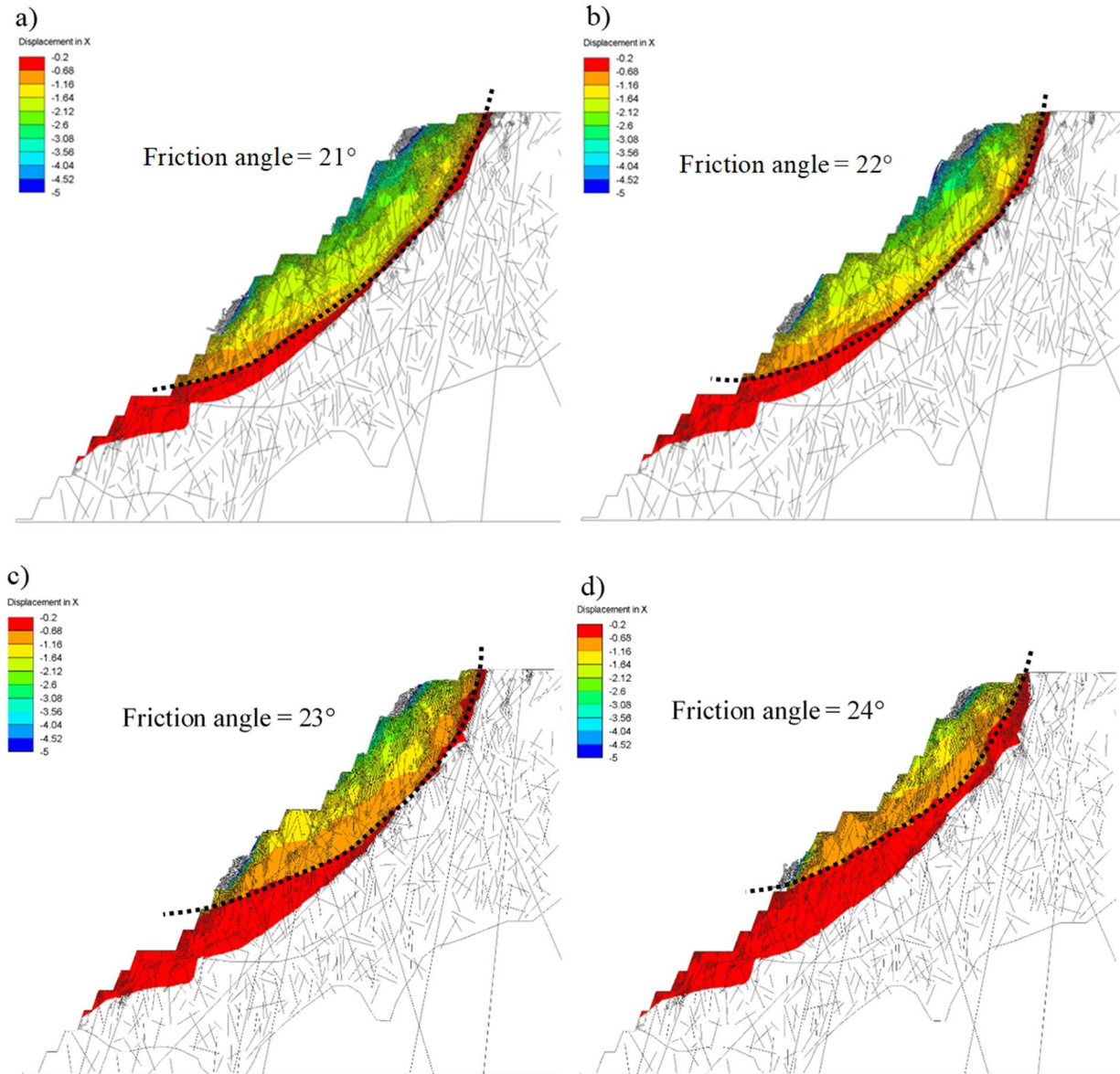


Figure 5.15. Sensitivity analysis performed in RS2 on increasing values of H&B's  $m_i$  as a manner of assess confined strength. Variations of  $m_i$  only for HELZ unit. Figures coloured by maximum shear strain. The extension of the failure surface does not change significantly. SRF varies from 0.95 for  $m_i=15$  to 1 for  $m_i=23$





**Figure 5.16. Sensitivity analysis performed in ELFEN software. H&B's  $m_i$  was transformed to friction angle for M-C rock mass properties. Figures colored by horizontal displacement. Interpreted failure surface (0.7 m threshold) indicated with dotted line. The extension of the failure surface and depth of the movement decreases when friction angle decreases. Failure surface for a friction angle of 23° (c) shows the best match with the extension of the real failure.**

Results from RS2 software showed negligible variation in the extension of the failure surface (**Figure 5.15**). As can be expected, all results showed an unstable slope, with SRF varying from 0.95, for the lower  $m_i$  values, to 1. In all cases the slide extends from the fault that limited the back of the failure up to the contact HELZ-HOLZ in the slope face. This can be considered still a fair representation of the failure surface, but the continuous code showed no sensitivity to the tested variations of confined strength.

The extension of the failure is sensitive to changes of rock mass friction angle in ELFEN software results. In all cases the failure surface is fully enclosed in the HELZ unit and is considered a fair representation of the real failure. Depth and extension of the failure increases with the decreasing of friction angle. The difference in height of the toe of the failure between the lowest and highest friction angle cases is approximately 55 meters (**Figure 5.16a and 5.16d**). Friction angle of  $23^\circ$ , equivalent of  $m_i=20$  (**Figure 5.16c**), shows the best agreement with the extension of the real failure. Thus, it can be asserted that numerically upscaled intact rock confined strength is overestimated ( $m_i=23$ ). This can be explained due to a higher capacity of dilation in a 2D sample, in which, the lack of constraints that impose a 3<sup>rd</sup> dimension, allow easier movement of blocks when numerical samples are tested under confinement.

## 5.6 Conclusion

Inter-ramp failure in the geological unit HELZ in Chuquicamata mine was presented. The HELZ unit can be summarized as a bad quality rock, with a well-connected fracture network. The instability was back analyzed in a 2D cross section for two cases: deriving rock mass strength properties from non-upscaled intact rock properties and from numerically upscaled intact rock properties. Non – upscaled intact rock properties correspond to laboratory test on samples with mixed rupture presented in Chapter 3, while numerically upscaled intact rock properties refer to those presented in detail in Chapter 4. RS2 continuum code and ELFEN FDEM hybrid code were used to back analyze the 2D cross section, with an addition of VIF and FT minor faults DFN for ELFEN analysis. The two cases, non-upscaled intact rock strength and numerically upscaled intact rock strength were analyzed in both software.

H&B's generalized failure criterion was used to characterize the rock mass strength. H&B's properties were input directly in RS2 while for ELFEN the H&B's envelope was linearized to obtain equivalent rock mass M-C properties. The blasting damage zone extension, where H&B's D factor is applied to rock mass properties, was shown to be an important controlling factor of the stability analysis. Rose et al (2018) assigned the fully disturbed limit to a depth of approx. 50 m for a 450 m slope height. This agrees with the D zone extension applied to the analysis performed in RS2 and ELFEN and with back analysis of previous instabilities in the Chuquicamata mine.

In the analysis performed in RS2 the vertical extension of the failure is overestimated 40 m for both cases analyzed (non-upscaled and upscaled rock properties). The back of the simulated slide is coincident with the fault that was the real limit of the instability. The SRF factor was 1.1 for the non-upscaled properties and 1 for the upscaled strength. In rigorous terms, the failure is replicated only when upscaled properties are used (SRF=1), however given the always existent uncertainty in the input variables, this is not a conclusive difference to consider the non-upscaled simulation stable. There is no difference in displacement for both cases in RS2 simulations.

In ELFEN simulation, the vertical extension of the instability for the upscaled case shows a good agreement with the real extension of the failure. For the non-upscaled case, the zone of movement is vertically more extended than the real slide, but is shallow in comparison with the upscaled case.

In general, the inter ramp failure can be reproduced for both sets of properties in a fair manner in RS2 and ELFEN software. The extension of the failure is similar to that observed in the field. However, the simulation based on numerically upscaled properties reproduces the failure more precisely in ELFEN code. The little contrast between the stability assessment with upscaled and non-upscaled properties included is attributed to the major influence of the joint network in the estimation of rock mass properties for the highly fractured leached rock.

Sensitivity analysis was performed on confined strength throughout variations of H&B's  $m_i$  in RS2 and its equivalent friction angle for M-C properties in ELFEN. While RS2 showed negligible sensitivity to different values of H&B's  $m_i$ , the extension of the failure in ELFEN showed to be dependent of rock mass friction angle. ELFEN results showed that friction angle of  $23^\circ$ , equivalent of  $m_i=20$ , is more suitable to reproduce the real failure in the HELZ unit. Thus, an overestimation

of numerically upscaled confined strength is established. It can be explained that due to a higher capacity of dilation in a 2D sample, in which, the lack of constrain that impose a 3<sup>rd</sup> dimension, allows easier movement of blocks when numerical samples are tested under confinement. ELFEN Hybrid code was shown to be a valuable tool to perform numerical upscaling of strength of a defected rock; however, confined strength can be overestimated when assessed in the bidimensional space. The overestimation of  $m_i$  factor for defected rock can lead to erroneously stable excavations, therefore, to use an  $m_i$  estimated in the range of 1.3-1.9\* $m_i$ , as recommended by Bewick et al (2019), is more suitable when no laboratory test is available.

The use of upscaled strength (or rock block strength) showed to be the right manner to assess rock mass stability in a major excavation. Applying this conclusion and following the proposal of Bewick et al (2019), the generalized Hoek and Brown failure criterion (Hoek et al, 2002) can be expressed in the following manner:

$$\sigma'_1 = \sigma'_3 + \sigma_{bl} \left( m_{rm} \frac{\sigma'_3}{\sigma_{bl}} + S \right)^a \quad (5.1)$$

$$m_{rm} = m_{bl} \exp \left( \frac{GSI-100}{24-14D} \right) \quad (5.2)$$

$$S = \exp \left( \frac{GSI-100}{9-3D} \right) \quad (5.3)$$

$$a = \frac{1}{2} + \frac{1}{6} \left( e^{-\frac{GSI}{15}} + e^{-\frac{20}{3}} \right) \quad (5.4)$$

Equations 5.1 to 5.4 introduce no change in the mathematical structure of H&B's criterion, but take into account the actual strength that the rock will develop due to scale effect. Thus,  $\sigma_{ci}$  is replaced by the rock block strength  $\sigma_{bl}$  and  $m_i$  factor is exchanged for rock block  $m_{bl}$  factor. This is not a modification of H&B's equations, but a precision of the values that should be used to characterize the rock and rock mass failure. In the opinion of the author, this is already implicitly stated in Hoek and Brown (2018).

## Chapter 6. Conclusions

### 6.1 Conclusions summary

Scale effect was assessed applying synthetic rock numerical experiments developed in ELFEN FDEM code. Real data from a naturally leached and defected rock was used as input, coupling rock components' strength and a discrete defect network. Rock matrix strength, defect strength and geometry of defects were obtained from laboratory testing and core logging. The rock mass was characterized using GSI to back analyze a major instability associated to it. Numerically upscaled and non-upscaled properties were used in the analysis to obtain rock mass strength, and results from both analyses were compared. The main conclusions of the numerical experiments performed in this research are:

- ELFEN FDEM software was able to realistically reproduce the progressive cracking and stress-strain curves of uniaxial, biaxial and indirect tensile testing. The scale effect of unconfined strength was assessed successfully using numerical samples in ELFEN, obtaining results that are in accordance with what is expected for both, the upscaled unconfined strength (rock block strength) and the scale effect. The resultant strength of the numerical samples was fitted with a H&B failure envelope. However, the numerically upscaled confined strength was overestimated. When no laboratory testing is available, upscaled  $m_i$  can be better estimated in the range of 1.3-1.9 times the  $m_i$  of the non-defected rock, as recommended by Bewick et al (2019), based on laboratory testing on veined samples.
- Upscaled intact rock properties must be used to estimate rock mass strength to assess excavations' stability or excavation design. Numerical experiments on a jointed rock demonstrated that rock bridges are subject to scale effect. Back analysis of a major instability showed that upscaled rock properties reproduced the failure in a more precise manner. The little contrast between the stability assessment with upscaled and non-upscaled properties included in this work is attributed to the major influence of the joint network in the estimation of rock mass properties for the highly fractured leached rock.

These conclusions summarize the findings related to synthetic rock and numerically upscaled rock properties in the stability assessment. The details of the findings are presented in the next two sections.

## **6.2 Findings on synthetic rock modelling of the defected rock and numerical upscaling**

The scale effect is a well-known characteristic of rock strength that is explained by the brittle failure mechanics, where natural defects are the controlling factor. In accordance with the variety of defect types that can be found in different geological settings, the extension of the scale effect is specific for each rock type and should be assessed in specific manner. The strength decreasing with size can be generalized mathematically using a relationship based on Weibull's distribution, but, the extension of the effect, i.e. the drop of the strength, must be assessed specifically for each type of rock. Synthetic rock experiments performed in ELFEN FDEM code were used to assess the scale effect on a real defected rock. The base laboratory data and field information came from a highly defected leached rock. The main conclusions related to SR experiments and evaluation of scale effect performed in **Chapter 4** are:

- The SR samples tested in ELFEN FDEM code show a realistic behavior when submitted to unconfined compression, biaxial compression and indirect tension testing. The fracturing patterns developed in SR samples agree with observations on real rock tests. The development of cracks parallel to loading direction occurred in unconfined compression, while coalescence of cracks and development of shear bands occurred under biaxial compression, both in agreement with real tests performed on brittle rock.
- Strength upscaling was verified using a series of UCS numerical tests of sample diameter in the range of 0.05 m – 1 m. Yoshinaka's (2008) application of Weibull's statistical theory shows a remarkably good agreement when fitted to average UCS of each sample size class. A  $k$  constant of 0.38 characterize the strength drop until the diameter of 0.5 m, where REV is reached at a UCS strength of 15 MPa. Unconfined strength is size dependent while H&B's  $m_i$  factor remains size invariant. Tensile strength was shown to be size dependent as well.

- Two alternative methods to account for the effect of defects in rock strength upscaling were applied to the data: rock block strength estimation (Laubscher and Jakubec, 2002) and composite GSI (CGSI, Day et al, 2012, Day, 2016). While the former yielded rock block strength higher but near the REV strength obtained from ELFEN SR, the latter showed negligible scale effect for the leached rock; this is considered incorrect by the author.
- The scale effect on rock bridges' strength was verified using a SR with defects and joints. The numerical experiment demonstrated that to derive the strength of a rock mass, scale effect on intact rock must be considered.

## **6.2 Findings on the use of numerically upscaled properties to assess major excavations stability**

The importance of strength upscaling lies in its use on the estimation of rock mass strength, which is a key parameter to the design of excavations and its stability assessment. Due to the impossibility of directly measuring the rock mass strength, it is estimated by combining the effect of rock strength and the network of natural fractures (joints). At failure, the rock mass strength is controlled by strength of the joint bounded block, i.e. the block strength, and the fracture network. Block strength is assumed to be approximately the fully upscaled rock strength. In practice, due to cost and technical limitations, the rock strength is tested at a scale that is below the rock block size; thus, the scale effect and rock block strength remain unknown, and the analysis is performed using non upscaled properties. The importance of scale effect and rock block strength is acknowledged in literature. However, there are not many studies addressing the outcome of use non upscaled strength vs upscaled strength in the assessment of major excavation stability.

**Chapter 5** shows the stability assessment of a slope using upscaled and non-upscaled properties. The analysis was performed in RS2 and ELFEN software. The main conclusions are:

- In general, the inter ramp failure can be reproduced using both sets of properties, upscaled and non-upscaled rock strength, in RS2 and ELFEN software. However, the upscaled rock strength yielded more precise results, with a SRF of 1 in RS2 and the extension of the slide matching the real extension of the instability in ELFEN.

- In the analysis performed in RS2, the vertical extension of the failure is overestimated 40 m for both cases analyzed, non-upscaled and upscaled rock properties. There is no difference in displacement for either case in RS2 simulations.
- In the ELFEN simulation, the vertical extension of the instability for the upscaled case shows a very good agreement with the real extension of the failure. For the non-upscaled case, the zone of movement is vertically more extended than the real slide but is shallow in comparison with the upscaled case.
- When upscaled unconfined strength is used to derive rock mass strength, the extension of the failure showed negligible sensitivity to different values of H&B's  $m_i$  in RS2 software, while in ELFEN failure height is dependent of rock mass friction angle. ELFEN results showed that a friction angle of  $23^\circ$ , equivalent to  $m_i=20$ , is more suitable to reproduce the real failure. This value is lower than the  $m_i=23$  obtained from SR numerical experiments, thus an overestimation of numerically upscaled  $m_i$  factor and confined strength was established.
- An overestimation of numerically upscaled confined strength can be explained due to a higher capacity of dilation in a 2D sample, in which, the lack of constraints that impose a 3<sup>rd</sup> dimension, allow easier movement of blocks when numerical samples are tested under confinement. The overestimation of  $m_i$  factor for defected rock can lead to erroneously stable analyses of excavations; therefore, to estimate  $m_i$  in the range of  $1.3-1.9*m_i$ , as recommended by Bewick et al (2019), is more suitable when no laboratory test is available.
- Upscaled intact rock properties must be used to estimate rock mass strength to assess excavations' stability or excavation design. Thus, in similar manner as proposed by Bewick et al (2019), a change in the expression of H&B's failure criteria (Hoek *et al* 2002) is suggested, replacing intact rock unconfined strength ( $\sigma_{ci}$ ) and  $m_i$  factor for rock block unconfined strength ( $\sigma_{bl}$ ) and  $m_{bl}$  factor. This suggestion does not affect the mathematical structure of the failure criteria.

#### 6.4 Recommendation for future work

Logic indicates that numerical modelling in the bidimensional space adds a degree of freedom to the analyzed system. This impacts the strength of the SR, overestimating the confined strength,



which was verified on H&B's  $m_i$  factor obtained from SR samples. This can be corroborated using 3d SR samples. In case the effect is confirmed, the author believes that the application of a proper angular filter to restrict the selection of discontinuities for 2d simulation can aid to balance this issue. The usual practice is including traces from 3d discontinuities that make a certain angle with the 2d trace plane. This is aimed at ensuring plain strain, avoiding discontinuities that are subparallel to the trace plane. Nowadays this angle filter is a matter that lies in the field of subjectivity and expert judgement. Comparison of equivalent SR samples performed in the 2d and 3d space could help create objective criteria for filtering. The aim would be ensuring plain strain and constraining the amount of traces in the 2d SR simulation, countering the extra degree of freedom. It is acknowledged here that the assemblage of 3d SR samples can be geometrically much more challenging than the 2d SR modelling, mainly related to the accommodation of a mesh of appropriate quality

For the stability assessment in Chapter 5, the main assumption is that blocks that would brake during a slope failure are larger than the REV. Thus, the rock block strength can be equal to the fully upscaled strength. This allows the application of the fully upscaled strength to estimate the rock mass strength using H&B's failure criterion and GSI. This is a fair assumption for the simulations in Chapter 5, but is not necessarily true for all rock masses. When REV is larger than the rock block size, the rock block strength cannot be considered equal to the fully upscaled rock strength. In addition, in a rock mass, breakage through rock bridges can be very complex (Elmo, 2018), making it difficult to anticipate the size of the block that will fail and the overall strength of the rock mass. Given the complexity of this case, it is not possible to estimate the strength of such rock mass only knowing the upscaled strength. Numerical experiments of SR with implicit defects and joints can be of great utility in addressing the upscaling of rock bridges.

In this work, the impact of use upscaled properties was assessed on a relatively weak and highly fractured leached rock (GSI = 35). The study of strongest and least fractured rock masses (GSI 40-65), is of interest to understand how important the application of upscaled rock properties is in excavation design and stability assessment.

As is well known, the scale effect is not exclusive to rock strength, but it is present in discontinuities as well. Shear strength of joints decreases when size increases, with the subsequent impact to rock mass strength. Joints' Shear and normal stiffness are scalable parameters that have an important influence in rock mass strength and SR modeling. As in the case of rock strength, the impact of discontinuities' scale effect on stability assessment and excavation design is a subject that offers ample space to explore.

## References

1. Bahrani, N., Kaiser PK. 2016. Numerical investigation of the influence of specimen size on the unconfined strength of defected rocks. *Computers and Geotechnics*. Vol. 77, pp 56-67.
2. Bandis, S.C., 1990. Scale effects in the strength and deformability of rocks and rock joints. In: Cunha, A.P. (Ed.), *Scale Effects in Rock Masses*. Balkema, pp. 59–76.
3. Bandis C.S. 1993. Engineering properties and characterization of rock discontinuities. In: *Comprehensive rock engineering*. Vol. 1. pp. 155-183.
4. Beran, S. 2017. The effect of cubic specimen size on uniaxial compressive strength of carbonate rocks from Western Turkey. *Arabian Journal of Geosciences*. Vol 10, 426.
5. Bewick RP, Amann F, Kaiser PK, Martin CD. 2015. Interpretation of UCS test results for engineering design. In: *Proceedings of the 13th International Congress on Rock Mechanics: ISRM Congress 2015 – Advances in Applied & Theoretical Rock Mechanics*. Montreal, Canada: International Society for Rock Mechanics and Rock Engineering. Paper 521.
6. Bewick RP, Kaiser PK & Amann F. 2018. Strength of Massive to Moderately Jointed Rock Masses. *Journal of Rock Mechanics and Geotechnical Engineering*. <https://doi.org/10.1016/j.jrmge.2018.10.003>
7. Bewick, R.P., Campbell, R., Brzovic, A., Schwarz, A., Pierce, M. 2019 Incorporating veined rock mass characteristics into engineering design and caving. In *Proceedings of 53rd U.S. Rock Mechanics/Geomechanics Symposium*. ARMA. 19-304.
8. Bieniawski, Z.T. 1968. The effect of specimen size on compressive strength of coal. *International Journal of Rock Mechanics and Mineral Science*. Vol. 5, pp. 325-335.
9. Bieniawski, Z. T. 1989. *Engineering rock mass classifications: a complete manual for engineers and geologists in mining, civil, and petroleum engineering*. John Wiley & Sons.
10. Bobet, A., Einstein, H. 1989. Fracture Coalescence in Rock-type Materials under Uniaxial and Biaxial Compression. *International Journal of Rock Mechanics & Mining Sciences*. Vol 35, pp. 863-888.

11. Cai, M., Kaiser, P. K., Uno, H., Tasaka, Y., Minami, M. 2004. Estimation of rock mass deformation modulus and strength of jointed hard rock masses using the GSI system. *International Journal of Rock Mechanics and Mining Sciences*, Vol 41, issue 1, pp 3-19.
  
12. Caine, J. S., Evans, J. P., Foster, C. G. 1996. Fault zone architecture and permeability structures. *Geology*, Vol 24, issue 11, pp. 1025-1028.
  
13. Carvalho, J.L., Kennard, D.T. and Lorig, L. 2002. Numerical Analysis of the east wall of Toquepala mine, Southern Andes of Peru. In *Proc. EUROCK*, Lisbon, pp. 615-625.
  
14. Cundall, P. A., Pierce, M. E., Mas Ivars, D. 2008. Quantifying the Size Effect of Rock Mass Strength. In Potvin, Y., Carter, J., Dyskin, A., Jeffrey, R. (eds), 1st Southern Hemisphere International Rock Mechanics Symposium (p. 15). Perth: Australian Centre for Geomechanics.
  
15. Cunha, P.A. (Ed.), 1990. Scale Effects in Rock Masses, *Proc. of the First International Workshop*. Balkema, Loen, Norway.
  
16. Day, J. J., Hutchinson, D. J., and Diederichs, M. S. 2012. A critical look at geotechnical classification for rock strength estimation. In *proceedings 46th U.S. Rock Mechanics Geomechanics Symposium*, ARMA, Chicago, IL, USA.
  
17. Day, J. 2016. The influence of healed intrablock rockmass structure on the behaviour of deep excavations in complex rockmasses. Ph.D. thesis. Queen's University. Canada.
  
18. Diederichs, M. 2007. The 2003 Canadian Geotechnical Colloquium: Mechanistic interpretation and practical application of damage and spalling prediction criteria for deep tunnelling. *Canadian Geotechnical Journal*. Vol 44, issue 9, pp 1082-1116.
  
19. Dold, B. 2003. Enrichment processes in oxidizing sulfide mine tailings: Lessons for supergene ore formation. *Society for Geology Applied to Mineral Deposits, SGA News*, Vol 16, pp 1-15. <https://e-sga.org/fileadmin/sga/newsletter/news16/art01.html>

20. Duran, F. 2017. A numerical investigation of stress path and rock mass damage in open pits. Master's thesis. Queen's University.
21. Eberhardt, E. 1998. Brittle rock fracture and progressive damage in uniaxial compression. Ph.D. Thesis, University of Saskatchewan, Saskatoon.
22. Eberhardt, E., Stead, D., Stimpson, B., Read, R.S. 1998. Identifying crack initiation and propagation thresholds in brittle rock. *Canadian Geotechnical Journal*. Vol 35, pp 222-233
23. Eberhardt, M. 1999. Why things break. *Scientific American*, Vol. 281, No. 4. pp. 66-73. <https://www.jstor.org/stable/10.2307/26058440>
24. Eberhardt, E., Stead, D., Coggan, J.S. 2004. Numerical analysis of initiation and progressive failure in natural rock slopes—the 1991 Randa rockslide. *International Journal of Rock Mechanics & Mining Sciences*. Vol 41, pp 69-87.
25. Elmo, D. 2006. Evaluation of a hybrid FEM/DEM approach for determination of rock mass strength using a combination of discontinuity mapping and fracture mechanics modelling, with particular emphasis on modelling of jointed pillars. Ph.D. thesis. Camborne School of Mines, University of Exeter, UK.
26. Elmo, D., Stead, D. 2010. An integrated numerical modeling - discrete fracture network approach applied to the characterization of rock mass strength of naturally fractured pillars. *Rock Mechanics and Rock Engineering*. Vol. 43, issue 1, pp. 3-19.
27. Elmo D. 2012. FDEM & DFN modelling and applications to rock engineering problems. Faculty of Engineering, Turin University; 2012
28. Elmo, D., Rogers, R, Stead, D., Eberhardt, E. (2014) Discrete Fracture Network approach to characterize rock mass fragmentation and implications for geomechanical upscaling. *Mining Technology*. Vol 123, pp 149-161. DOI: 10.1179/1743286314Y.0000000064
29. Elmo, D., Stead, D. 2017. Application of fracture mechanics to rock slopes. In Feng, X.-T. (ed), *Rock Mechanics and Engineering, Volume 3, Analysis, Modeling & Design*. Pp 705-735

30. Elmo, D., Moffit, K., Carvalho, J. 2016. Synthetic rock mass modelling: experience gained and lessons learned. In proceedings 50th U.S. Rock Mechanics Geomechanics Symposium, ARMA, 16-777.
31. Elmo, D., Donati, D., Stead, D. 2018. Challenges in the characterization of intact rock bridges in rock slopes. Engineering Geology. DOI:10.1016/j.enggeo.2018.06.014
32. Farahmand, K. 2017. Characterization of rockmass properties and excavation damage zone (edz) using a synthetic rock mass (srm) approach. Ph.D. thesis. Queen's University. Canada.
33. Flores, G., Karzulovic, A. 2003. Geotechnical guideline for a transition from open pit to underground mining: Geotechnical characterization. Report to International Caving Study II. Brisbane: JKMRC
34. Gao, F., Stead, D., Kang, H. 2014. Numerical investigation of the scale effect and anisotropy in the strength and deformability of coal. International Journal of Coal Geology. Vol 136, pp 25–37
35. Goodman, R.E. (1989) Introduction to Rock Mechanics. 2nd Edition, John Wiley & Sons Ltd., New York.
36. Golder Associates. 2017. FracMan Version 7.60. FracMan Technology Group. <http://www.fracman.com/>
37. Griffith, A. 1920. The phenomena of rupture and flow in solids. Philosophical Transactions of the Royal Society of London, Series A, Mathematical and Physical Sciences, Vol 221, pp. 163-198.
38. Guest, A., Read, J. 2009. Geotechnical model. In: Read and Stacey, Guidelines for open pit slope design. CSIRO publishing. Pp 201-212
39. Hamdi, P. 2015. Characterization of Brittle Damage in Rock from the Micro to Macro Scale. Ph.D. thesis. Simon Fraser University, Canada

40. Hamdi, P., Stead, D., Elmo, D. 2015 Characterizing the influence of stress-induced microcracks on the laboratory strength and fracture development in brittle rocks using a finite-discrete element method-micro discrete fracture network FDEM-mDFN approach. *Journal of Rock Mechanics and Geotechnical Engineering*. Vol 7, pp 609-625
41. Hammah, R., Curran, J., Yacoub, T., Corkum, B. et al 2004. Stability Analysis of Rock Slopes using the Finite Element Method. In Schubert (ed.) EUROCK 2004 & 53<sup>rd</sup> Geomechanics Colloquium
42. Hammah, R.E, Yacoub, T.E, Corkum, B., Wibowo, F., Curran, J.H. 2007. Analysis of blocky rock slopes with finite element shear strength reduction analysis. In 1st Canada-U.S. Rock Mechanics Symposium. Pp 329-334. DOI: [10.1201/NOE0415444019-c40](https://doi.org/10.1201/NOE0415444019-c40)
43. Hoek E. 1994. Strength of rock and rock masses. *ISRM News Journal*. Vol 2, issue 2, pp 4-16
44. Hoek, E., Brown, E. 1997. Practical estimates of rock mass strength. *International Journal of Rock Mechanics and Mining Sciences*. Vol 34, issue 8, pp 1165-1186.
45. Hoek, E., and Diederichs, M. 2006. Empirical estimation of rock mass modulus. *International journal of rock mechanics and mining sciences*. Vol. 43, issue 2, pp 203-215.
46. Hoek, E. Marinos, P. 2000. Predicting Tunnel Squeezing. *Tunnels and Tunnelling International*. Vol 132, issue 11, pp 45-51
47. Hoek, E., Carter, T. G., Diederichs, M. S. 2013. Quantification of the geological strength index chart. 47th US Rock Mechanics/Geomechanics Symposium.
48. Hoek, E., Martin, D. 2014, Fracture initiation and propagation in intact rock - A review. *Journal of Rock Mechanics and Geotechnical Engineering*. Vol 6, issue 4, pp 287-300.
49. Hoek E., Brown E.T. 1980. *Underground excavations in rock*. London: Institution of Mining and Metallurgy.

50. Hoek E., Carranza-Torres C., Corkum B. 2002. Hoek-Brown failure criterion-2002 edition. In Proceedings of the Fifth North American Rock Mechanics Symposium. Toronto, Canada. pp. 267-273.
51. Hoek E, Kaiser PK, Bawden WF. 1995. Support of underground excavations in hard rock. Rotterdam: A.A. Balkema.
52. Hoek, E., Brown, E.T. 2019. The Hoek-Brown failure criterion and GSI - 2018 edition. Journal of Rock Mechanics and Geotechnical Engineering. Vol 11, pp 445-463
53. Jackson, R., Lau, J.S.O., 1990. The effect of specimen size on the laboratory mechanical properties of Lac du Bonnet grey granite. In: Cunha, P. (Ed.), Scale Effect in Rock Masses. Balkema, pp. 165–174.
54. Jakubec, J. 2013. Role of defects in rock mass classification. In: Potvin, Y. & Brady, B. (eds), Proceedings of the Seventh International Symposium on Ground Support in Mining and Underground Construction, Australian Centre for Geomechanics, Perth, pp. 337-344
55. Kaiser, PK., Amann, F., Bewick RP. 2015. Overcoming challenges of rock mass characterization for underground construction in deep mines. In: Proceedings of the 13th International Congress on Rock Mechanics: ISRM Congress 2015 – Advances in Applied & Theoretical Rock Mechanics. Montreal, Canada: International Society for Rock Mechanics and Rock Engineering
56. Karimi, L., Elmo, D., Stead, D. 2016. Simulation of rock bridge failure at the laboratory scale using a combined FDEM modeling and discrete crack network approach. In Proceedings of 53rd U.S. Rock Mechanics/Geomechanics Symposium. ARMA. 16-588.
57. Karimi, L., Elmo, D., Stead, D. 2019. Improving DFN-geomechanical model integration using a novel automated approach. Computers and Geotechnics. Vol 105, pp 228–248
58. Klerck P.A. 2000. The finite element modelling of discrete fracture in quasi-brittle materials. Ph.D. thesis. University of Swansea - Wales.
59. Klerck P.A., Sellers E.J. and Owen D.R.J. 2004. Discrete fracture in quasi-brittle materials under compressive and tensile stress states. Computational Methods Applied to Mechanical Engineering. Vol. 193, pp 3035-3056.



60. Laubscher D. H., Jakubec J. (2000). The MRMR rock mass classification for jointed rock masses. In: Hustrulid WA, Bullock RL, eds. Underground mining methods: engineering fundamentals and international case studies. Littleton, CO: Society for Mining, Metallurgy, and Exploration, Inc., pp. 475–481.
61. Lorig, L., Stacey, P., Read, J. 2009. Slope design methods. In: Read and Stacey, Guidelines for open pit slope design. CSIRO publishing. Pp 237-250
62. Lundborg, P. 1966. The strength-size relation of granite. International Journal of Rock Mechanics and Mineral Science. Vol. 4, pp. 269-272
63. Mahabadi, O. K. (2012). Investigating the influence of micro-scale heterogeneity and microstructure on the failure and mechanical behavior of geomaterials, Ph.D. thesis, University of Toronto, Toronto, Canada.
64. Marambio, F., Pereira, J., Russo, A. 2000. Metodología para seleccionar y analizar resultados de ensayos geotécnicos representativos de roca intacta. IX congreso Geológico Chileno. Puerto Varas.
65. Mayer, J.M., Stead, D. 2017. Exploration into the causes of uncertainty in UDEC Grain Boundary Models. Computers and Geotechnics. Vol. 82, pp 110-123
66. Nicksiar, N., Martin, C. D. 2014. Factors Affecting Crack Initiation in Low Porosity Crystalline Rocks. Rock Mechanics and Rock Engineering. Vol 47, pp 1165-1181.
67. Munjiza, A. 2004. The combined finite-discrete element method. John Wiley & Sons Ltd., Chichester, UK.
68. Pierce M, Gaida M, DeGagne D. 2009. Estimation of rock block strength. In: Diederichs M, Grasselli G, editor. ROCKENG09, 3rd Can-US Rock Mechanics Symposium. Paper 4360.
69. Pierce, M., Mas Ivars, D., Cundall, P.A. & Potyondy, D.O. 2007. A Synthetic Rock Mass Model for Jointed Rock. In Eberhardt, E. et al. (ed), Rock Mechanics: Meeting Society's Challenges and Demands, 1st Canada-U.S. Rock Mechanics Symposium, Vancouver.

70. Pratt, H.R., Black, A.D., Brown, W.S., Brace, W.F., 1972. The effect of specimen size on the mechanical properties of unjointed diorite. *International Journal of Rock Mechanics and Mineral Science*. Vol 9, pp 513-529
71. Informe Proyecto Aumento Angulo de Talud. 2005. Internal report, Superintendence of Geotechnics, Codelco- Chile. Chuquicamata Division. Unpublished
72. Potyondy, D. O., Cundall, P. A. 2004. A bonded-particle model for rock. *International Journal of Rock Mechanics and Mining Sciences*. Vol 41, pp 1329-1364. <http://doi.org/10.1016/j.ijrmms.2004.09.011>
73. Read, J., Jakubec, J., Beale, G. 2009. Field data collection. In: Read and Stacey, Guidelines for open pit slope design. CSIRO publishing. Pp 15-25
74. Reutter, K.-J., Chong, G., Scheubber, E. 1993. The "West Fissure" and the precordilleran fault system of northern Chile. *Second ISAG, Oxford (LJK)*, 21 -23 1911 993
75. Rocscience. 2017. RocData. Version 5.009. Toronto, ON, Canada. [www.rocscience.com](http://www.rocscience.com)
76. Rocscience. 2019. RS2. Version 10.007. Toronto, ON, Canada. [www.rocscience.com](http://www.rocscience.com)
77. Rockfield Software Ltd. 2013. ELFEN Version 4.7.1. Swansea, UK
78. Rose, ND., Scholz, M., Burden, J., King, M., Maggs, C., Havaej, M. 2018. Quantifying transitional rock mass disturbance in open pit slopes related to mining excavation. In: *Slope stability 2018 - XIV International congress on energy and mineral Resources*. Seville, Spain: Asociación Nacional de Ingenieros de Minas. pp. 1273e88.
79. Russo, A., Hormazabal, E. 2016. A methodology to select valid results from laboratory tests to estimate properties of intact rock with microdefects. In *Proceedings of 50th U.S. Rock Mechanics/Geomechanics Symposium*. ARMA. 16-416
80. Sari, M. 2019. Stability analysis of cut slopes using empirical, kinematical, numerical and limit equilibrium methods: case of old Jeddah–Mecca road (Saudi Arabia). *Environmental Earth Sciences*. <https://doi.org/10.1007/s12665-019-8573-9>.

81. Schlotfeldt *et al*, 2017 crazy horse Schlotfeldt, P., Elmo, D., Panton, B. 2018. Overhanging rock slope by design: an integrated approach using rock mass strength characterisation, large scale numerical modelling and limiting equilibrium methods, *Journal of Rock Mechanics and Geotechnical Engineering*, DOI: [10.1016/j.jrmge.2017.09.008](https://doi.org/10.1016/j.jrmge.2017.09.008).
82. Shang, J., Hencher, S. R., West, J. 2016. Tensile Strength of Geological Discontinuities Including Incipient Bedding, Rock Joints and Mineral Veins. *Rock Mechanics and Rock Engineering*. Vol 49, pp 4213-4225
83. Sonmez, H., Ulusay, R. 2002. A discussion on the Hoek-Brown failure criterion and suggested modification to the criterion verified by slope stability case studies. *Yerbilimleri (Earthsciences)*. Vol 26, pp 77-99.
84. Stavrou, A., Vazaios, I., Murphy, W., Vlachopoulos, N. 2019. Refined Approaches for Estimating the Strength of Rock Blocks. *Geotech and Geological Engineering*. Vol 37, issue 6, pp 5409-5439
85. Stavrou, A., Murphy, W. 2018. Quantifying the effects of scale and heterogeneity on the confined strength of micro-defected rocks. *International Journal of Rock Mechanics and Mining Sciences*. Vol 102, pp 131–143
86. Stead, D., Eberhardt, E., Coggan, J.S. 2006. Developments in the characterization of complex rock slope deformation and failure using numerical modelling techniques. *Engineering Geology*. Vol 83, pp 217-235
87. Tatone, B., Graselli, G. 2015. A calibration procedure for two-dimensional laboratory-scale hybrid finite–discrete element simulations. *International Journal of Rock Mechanics & Mining sciences*. Vol 75, pp 56-72
88. Thuro, K., Plinninger, R.J., Zäh, S., Schütz, S. 2001. Scale effect in rock strength properties. Part 1: Unconfined compressive test and Brazilian test. In: Särkkä & Eloranta (eds.), *Rock Mechanics – a Challenge for Society*. Espoo, Finland.
89. Tomlinson, A.J.; Mpodozis, C; Cornejo, R; Ramirez, C.F.; Dumitru, T. 1994. El Sistema de fallas Sierra Castillo-Agua Amarga: transpresion sinistral eocena en la Precordillera de Potrerillos-El Salvador. *In Congreso Geologico Chileno*, No. 7, Actas 2: 1459-1463. Concepcion.

90. Turichshev, A., & Hadjigeorgiou, J. 2015. Experimental and Numerical Investigations into the Strength of Intact Veined Rock. *Rock Mechanics and Rock Engineering*, pp 1897–1912. <http://doi.org/10.1007/s00603-014-0690-x>
91. Turichshev, A., Hadjigeorgiou, J. 2016. Development of Synthetic Rock Mass Bonded Block Models to Simulate the Behaviour of Intact Veined Rock. *Geotechnical and Geological Engineering*. <http://doi.org/10.1007/s10706-016-0108-5>
92. Vallejos, J. A., Suzuki, K., Brzovic, A., & Ivars, D. M. 2016. Application of Synthetic Rock Mass modeling to veined core-size samples. *International Journal of Rock Mechanics and Mining Sciences*. Vol 81, pp 47-61. <http://doi.org/10.1016/j.ijrmms.2015.11.003>
93. Vyazmensky, A., Stead, D., Elmo, D., Moss, A. 2010. Numerical analysis of block caving-induced instability in large open pit slopes: A finite element/discrete element approach. *Rock Mechanics and Rock Engineering*. Vol 43, pp 21-39
94. Weibull, W. 1951. A statistical distribution function of wide applicability. *Journal of Applied Mechanics*. Vol. 18, pp. 293-297.
95. Yilmaz, I., Sendir, H. 2002. Correlation of Schmidt hardness with unconfined compressive strength and Young's modulus in gypsum from Sivas (Turkey). *Engineering Geology*. Vol 66, pp 211-219
96. Yoshinaka, R., Osada, M., Park, H., Sasaki, T., Sasaki, K. 2008. Practical determination of mechanical design parameters of intact rock considering scale effect. *Engineering Geology*. Vol 96, pp 173-186.
97. Zhang, Q., Zhu, H., Zhang, L., Ding, X. 2011. Study of scale effect on intact rock strength using particle flow modeling. *International Journal of Rock Mechanics and Mining Sciences*. Vol 48, issue 8, pp 1320-1328. <https://doi.org/10.1016/j.ijrmms.2011.09.016>.
98. Zhang Z.X. 2002. An empirical relation between mode I fracture toughness and the tensile strength of rock. *International Journal of Rock Mechanics & Mining Sciences*. Vol. 39, pp 401-406.